Casting Integrity of High-Pressure Die-Castings

A thesis submitted for the degree of Doctor of Philosophy

by

Ewan Lordan

Department of Mechanical and Aerospace Engineering

Brunel University London

Declaration of Authorship

This thesis has been composed solely by the candidate, and has not been submitted—in whole or in part—for the attainment of any other higher education degree or professional qualification. The candidate was part of a research group at the Brunel Centre for Advanced Solidification Technology (BCAST), and made substantial contributions to all aspects of the work; the contributions of others is explicitly stated in the text. Parts of this thesis have been published in peer-reviewed journals, with co-authors clearly acknowledged at the beginning of each chapter. A full list of jointly-authored works can be found below.

Contributions of Others to the Thesis as a Whole

The text makes several references to a finite element model developed under the ProCAST (ESI Group) software platform. Although the candidate played a major role in the experimental validation of this model, the model itself was developed by Dr. Kun Dou and Prof. Alain Jacot, both of whom were members of the research group. My co-supervisor, Dr. Yijie Zhang, assisted in the design and completion of experiments. Ms. Chrysoula Tzileroglou assisted in sample preparation and EBSD mapping.

Published Works by the Author Incorporated into the Thesis

[1] E. Lordan, J. Lazaro-Nebreda, Y. Zhang, K. Dou, P. Blake, Z. Fan, On the Relationship Between Internal Porosity and the Tensile Ductility of Aluminium Alloy Die-Castings, Mater. Sci. Eng.: A 778 (2020) 139107. https://doi.org/10.1016/j.msea.2020.139107.

[2] E. Lordan, Y. Zhang, K. Dou, A. Jacot, C. Tzileroglou, P. Blake, Z. Fan, On the Probabilistic Nature of High-Pressure Die Casting, manuscript submitted for publication (2020).

[3] E. Lordan, K. Dou, Y. Zhang, C. Tzileroglou, A. Jacot, P. Blake, Z. Fan, Turbulent Breakup of Non-Metallic Inclusions and Equiaxed Crystals during Solidification of a Hypoeutectic Al-Si Alloy, manuscript submitted for publication (2020).

[4] K. Dou, E. Lordan, Y.J. Zhang, A. Jacot, Z.Y. Fan, Numerical Simulation of Fluid Flow, Solidification and Defects in High Pressure Die Casting (HPDC) Process, IOP Conf. Ser.: Mater. Sci. Eng. 529 (2019) 012058. https://doi.org/10.1088/1757-899X/529/1/012058.

[5] K. Dou, E. Lordan, Y.J. Zhang, A. Jacot, Z.Y. Fan, A Complete Computer Aided Engineering (CAE) Modelling and Optimization of High Pressure Die Casting (HPDC) Process, J. Manuf. Process. 60 (2020) 435-466. https://doi.org/10.1016/j.jmapro.2020.10.062.

[6] K. Dou, E. Lordan, Y. Zhang, A. Jacot, Z. Fan, Improvement of Mechanical Properties for Aluminium Alloy in High Pressure Die Casting (HPDC) Process Combining Experimental and Modelling Approach, manuscript Submitted for Publication. (2020).

Published Works by the Author Relevant to the Thesis but not Forming Part of It

[7] E. Lordan, J. Lazaro-Nebreda, Y. Zhang, Z. Fan, Effective Degassing for Reduced Variability in High-Pressure Die Casting Performance, JOM. 71 (2019) 824–830. https://doi.org/10.1007/s11837-018-3186-4.

[8] Y. Zhang, S. Wang, E. Lordan, Y. Wang, Z. Fan, Improve Mechanical Properties of High Pressure Die Cast Al9Si3Cu Alloy via Dislocation Enhanced Precipitation, J. Alloys Compd. 785 (2019) 1015–1022. https://doi.org/10.1016/j.jallcom.2019.01.278.

[9] Y. Zhang, E. Lordan, K. Dou, S. Wang, Z. Fan, Influence of Porosity Characteristics on the Variability in Mechanical Properties of High Pressure Die Casting (HPDC) AlSi7MgMn Alloys, J. Manuf. Process. 56 A (2020) 500-509. https://doi.org/10.1016/j.jmapro.2020.04.071.

Acknowledgements

"*Most men will not swim before they are able to*" – Novalis (1802).

My first debt is to Prof. Shouxun Ji, who recruited me to the project. I gratefully acknowledge the financial support provided by both Jaguar Land Rover Automotive PLC and the Engineering and Physical Sciences Research Council (grant number: 2043200).

I also owe thanks to many friends and colleagues. To my principal supervisor, Prof. Zhongyun Fan, for your direction, integrity, and spirit. To my co-supervisor, Dr. Yijie Zhang, for your guidance, generosity, and friendship. I am also indebted to Prof. Alain Jacot and Dr. Kun Dou, whose expertise in computational modelling, and sense of humour, were invaluable additions to the research group.

To Mr. Paul Blake, for your organizational intelligence and managerial ethos. I am also grateful for the opportunity to spend time at Jaguar Land Rover, for which I would like to thank Mr. Paul Blake, Mr. Daniel Silver, Dr. Zongjin Lu, Mr. Robert Crow, and Mr. Stuart Tyler.

To Dr. Chamini Mendis, Dr. Jaime Lazaro-Nebreda, and Dr. Loredana Saccone for your guidance and assistance with X-ray tomography experiments. To Ms. Chrysoula Tzigleroglou, for your assistance with electron backscatter diffraction mapping. To Dr. Maaouia Souissi, for stimulating discussions during our evening walks. I also thank members of the technical team—Mr. Jon Gadd, Mr. Peter Lloyd, Ms. Sam Melvin, Mrs. Stefanie Kennedy, Mrs. Aneta Walsh, and Mr. Stephen Cook—at BCAST for their expertise and, more importantly, their patience.

Finally, I would like to thank my friends and family. I am particularly indebted to Genevieve, to whom I owe thanks for innumerable reasons.

Abstract

High-pressure die casting (HPDC) is widely used in the manufacture of automobiles and aeroplanes; however, the mechanical properties of die-castings are notoriously inconsistent. This inconsistency leads to high scrap rates and increased safety factors for component design. Although the mechanical properties of die-castings have been linked to various microstructural heterogeneities, the underlying cause of variability remains somewhat enigmatic

First, a *Baseline* HPDC process is established that is representative of commercial foundry practice. Porosity and non-metallic inclusions are identified as the main sources of variability in tensile ductility, for specimens produced under these conditions. It is proposed that these non-metallic inclusions form during the pyrolysis of commercial plunger lubricants, and that these large pores derive from dilatational strains introduced during semi-solid deformation.

The ensuing series of experiments explore ways of reducing defect size using conventional HPDC equipment. Changing the kinematics of the plunger can greatly reduce the scatter in tensile ductility, which is attributed to the reduced size of pores observed under these conditions. The breakup of defect-forming suspensions during the transportation of liquid metals is then considered. Increasing the dissipation rate of turbulent kinetic energy leads to a refinement of non-metallic inclusions and primary α-Al crystals nucleated in the shot chamber. This refinement enhances the tensile ductility of the castings. Grain refinement is attributed to the fragmentation of incipient grains following turbulent oscillations of the surrounding liquid.

Finally, a novel technique—based on X-ray tomography and digital image processing—is presented to predict the areal fraction of porosity involved during tensile failure. By coupling this technique with an existing analytical model, the tensile fracture strain and tensile fracture stress are predicted to within 10.9 % and 8.1 % error, respectively. This fares well against its predecessor for which maximum errors of 242 % and 33.5 % were reported, respectively.

Table of Contents

Chapter 1: Introduction

1.1 Background and Challenges

Glaciers are melting, sea levels are rising, and extreme weather events are increasingly more frequent. Climate change is real. Climate change—specifically global warming—is primarily driven by the anthropogenic emission of greenhouse gases, with CO_2 being the main contributor. Road transportation accounts for roughly 21 % of CO_2 emissions in the European Union and is the main cause of air pollution in cities [1]. On 17 April 2019, the European Parliament and Council announced reduction targets of -15 % and -37.5 % for the CO_2 emissions of newly-registered passenger cars for the years 2025 and 2030, respectively [2]. Automobile manufacturers have responded to the emission reduction challenge by expanding their portfolio of electrically-chargeable vehicles. However, the market penetration of these vehicles is relatively low (Fig. 1.1). The sales of alternatively-powered vehicles will need to increase if the European Union hopes to achieve its 2025 and 2030 CO_2 emission targets.

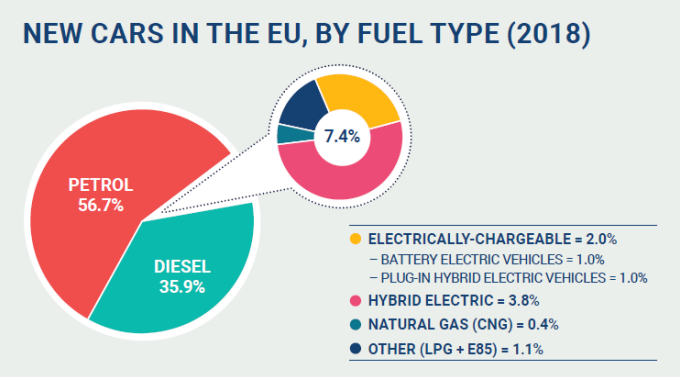

Fig. 1.1 Market share of fuel types for new passenger cars sold in the European Union for the year 2018 [2].

The main barriers to consumers are affordability and the availability of charging infrastructure [2]. Consumers worry that an electric vehicle will run out of power before reaching its destination, or a suitable charging point. One way to alleviate this anxiety is to increase the range of the vehicle—the distance travelled on a single charge. Lightweighting is a cost-effective route to reducing CO_2 emissions and improving vehicle range. Substituting steel for lightweight materials, such as aluminium alloys and magnesium alloys, can lead to weight savings of up to 50 % in the vehicle's body and chassis [3]. Aluminium alloys also enable closed-loop recycling, which presents both ecological and economic benefits in itself.

High-pressure die casting (HPDC) is the most common method for producing light alloy structures intended for use in automobiles. This is in part due to its high dimensional tolerance and suitability for robotic automation. In HPDC, a hydraulically actuated plunger injects molten metal into a sealed

mould cavity, where it solidifies under an applied pressure of 30∼100 MPa [4]. The process thus elicits an array of rich and complex phenomena including solidification, fluid turbulence, and semi-solid deformation. Combined, these phenomena make HPDC somewhat probabilistic in nature: the mechanical properties of die-castings are notoriously inconsistent [5–7]. This inconsistency leads to high scrap rates and increased safety factors for component design. Although the mechanical properties of die-castings have been linked to various microstructural heterogeneities—porosity [5,6], oxides [7,8], defect bands [9,10], sludge particles [11,12], cold flakes [12,13], and externally solidified crystals [14–16] to name a few— the underlying cause of variability remains somewhat enigmatic.

Porosity is one of the most common defects in conventionally die-cast structures. According to the mainstream literature [17,18], porosity is attributed to two main sources: solidification shrinkage, and the expansion of gaseous phases; however, recent studies involving synchrotron X-ray imaging [19–21] have shown that porosity also depends on the response of the semi-solid alloy to shear deformation. Pores adversely affect the fracture properties of die-cast structures by reducing the load-bearing area and localising strain [22]. Researchers have strived to establish a quantitative relationship between the casting integrity and the materials performance in tensile [22–24] and fatigue [25,26]; however, more experimental evidence is required to test the validity of these models. Validated models will enable materials engineers to produce more informed safety factors for component design, leading to a reduction in component cost and/or weight.

Over the past two decades, several so-called ‘high-integrity’ HPDC processes have emerged that aim to reduce the amount of porosity in die-castings [18]. Of these processes, the most commercially viable is vacuum-assisted HPDC. This variant of HPDC uses a vacuum system to evacuate air from the mould cavity prior to liquid metal injection. Although studies [6,27,28] suggest that these processes can be effective, the comparisons made to conventional HPDC are often biased. For example, when comparing vacuum-assisted HPDC and conventional HPDC, researchers tend to use the same processing parameters—processing parameters that are often tailored to the requirements of the vacuum system. Furthermore, these processes rely on the use of expensive external equipment that require regular maintenance. A major goal of the HPDC industry is to develop innovative technologies that enable the casting of high-integrity components using conventional HPDC equipment. To achieve this, the scientific community must first identify useful physical phenomena and means of further exploiting their potency.

1.2 Thesis Outline

This doctoral thesis aims to address the following challenges faced by the die casting industry:

- The dominant source of variability in mechanical properties is presently unknown.
- So-called 'high-integrity' processes rely on the use of expensive external equipment.
- A quantitative relationship needs to be established between the size of defects and the mechanical properties.

Following the introduction is a series of preliminaries (Chapters 2–5). Chapter 2 reviews current knowledge on topics relevant to the completion, and interpretation, of this thesis. Particular attention is paid to solidification and defect formation in HPDC, and the fundamentals of X-ray tomography (a technique which is used extensively in this work). Chapters 3 and 4 present the experimental and statistical techniques used throughout this thesis, respectively. A set of processing parameters and operating conditions are established in Chapter 5 that are representative of commercial foundry practice. The mechanical properties of specimens produced under these conditions will serve as a *baseline* for subsequent benchmarking.

After these preliminaries, the research findings are presented in Chapters 6-8. These chapters—which expand on papers published by the authors (see pages 1 and 2)—are presented in an order that is intended to emphasise the coherent nature of this work. Chapter 6 presents an investigation into the underlying cause of variability in mechanical properties, identifying critical casting defects and elucidating their genesis. Ways of reducing defect size using conventional HPDC equipment are then considered; this is achieved through a combination of process optimization (Chapter 6) and die design (Chapter 7). Finally, a quantitative relationship is established between the size of these defects and the materials performance in monotonic tension (Chapter 8). Chapter 9 concludes the thesis by reviewing its contributions to the field, and suggesting direction for future work.

1.3 References

[1] European Union, Road transport: Reducing CO_2 Emissions from Vehicles. https://ec.europa.eu/clima/policies/transport/vehicles_en (accessed September 4, 2020).

[2] European Automobile Manufacturers Association (ACEA), Making the Transition to Zero-Emission Mobility, 2019. https://www.acea.be/uploads/publications/ACEA_progress_report_2019.pdf.

[3] United States Department of Energy, Lightweight Materials for Cars and Trucks. https://www.energy.gov/eere/vehicles/lightweight-materials-cars-and-trucks (accessed August 28, 2020).

[4] X.P. Niu, K.K. Tong, B.H. Hu, I. Pinwill, Cavity Pressure Sensor Study of the Gate Freezing Behaviour in Aluminium High Pressure Die Casting, Int. J. Cast Met. Res. 11 (1998) 105–112. https://doi.org/10.1080/13640461.1998.11819264.

[5] H. Yang, S. Ji, D. Watson, Z. Fan, Repeatability of Tensile Properties in High Pressure Die-Castings of An Al-Mg-Si-Mn Alloy, Met. Mater. Int. 21 (2015) 936–943. https://doi.org/10.1007/s12540-015-5108-0.

[6] X. Dong, X. Zhu, S. Ji, Effect of Super Vacuum Assisted High Pressure Die Casting on the Repeatability of Mechanical Properties of Al-Si-Mg-Mn Die-Cast Alloys, J. Mater. Process. Technol. 266 (2019) 105–113. https://doi.org/10.1016/j.jmatprotec.2018.10.030.

[7] Y. Zhang, J.B. Patel, J. Lazaro-Nebreda, Z. Fan, Improved Defect Control and Mechanical Property Variation in High-Pressure Die Casting of A380 Alloy by High Shear Melt Conditioning, JOM. 70 (2018) 2726–2730. https://doi.org/10.1007/s11837-018-3005-y.

[8] D.R. Gunasegaram, M. Givord, R.G. O'Donnell, B.R. Finnin, Improvements Engineered in UTS And Elongation of Aluminum Alloy High Pressure Die Castings Through the Alteration of Runner Geometry and Plunger Velocity, Mater. Sci. Eng.: A 559 (2013) 276–286. https://doi.org/10.1016/j.msea.2012.08.098.

[9] C.M. Gourlay, H.I. Laukli, A.K. Dahle, Defect Band Characteristics in Mg-Al and Al-Si High-Pressure Die Castings, Metall. Mat. Trans. A 38 (2007) 1833–1844. https://doi.org/10.1007/s11661-007-9243-1.

[10] X. Li, S.M. Xiong, Z. Guo, Failure Behavior of High Pressure Die Casting AZ91D Magnesium Alloy, Mater. Sci. Eng.: A 672 (2016) 216–225. https://doi.org/10.1016/j.msea.2016.07.009.

[11] S. Ferraro, G. Timelli, Influence of Sludge Particles on the Tensile Properties of Die-Cast Secondary Aluminum Alloys, Metall. Mater. Trans. B 46 (2015) 1022–1034. https://doi.org/10.1007/s11663-014-0260-3.

[12] G. Timelli, A. Fabrizi, The Effects of Microstructure Heterogeneities and Casting Defects on the Mechanical Properties of High-Pressure Die-Cast AlSi9Cu3(Fe) Alloys, Metall. Mater. Trans. A 45 (2014) 5486–5498. https://doi.org/10.1007/s11661-014-2515-7.

[13] M. Okayasu, S. Wu, T. Hirayama, Y.-S. Lee, Method for Reducing Aluminum Alloy Heat Loss in High Pressure Die Casting Shot Sleeves, Int. J. Cast Met. Res. 31 (2018) 308–316. https://doi.org/10.1080/13640461.2018.1470370.

[14] X. Li, W. Yu, J. Wang, S. Xiong, Influence of Melt Flow in the Gating System on Microstructure and Mechanical Properties of High Pressure Die Casting AZ91D Magnesium Alloy, Mater. Sci. Eng.: A 736 (2018) 219–227. https://doi.org/10.1016/j.msea.2018.08.090.

[15] X. Li, S.M. Xiong, Z. Guo, On the Porosity Induced by Externally Solidified Crystals in High-Pressure Die-Cast of AM60B Alloy and its Effect on Crack Initiation and Propagation, Mater. Sci. Eng.: A 633 (2015) 35–41. https://doi.org/10.1016/j.msea.2015.02.078.

[16] Y. Zhou, Z. Guo, S.-M. Xiong, Effect of Runner Design on the Externally Solidified Crystals in Vacuum Die-Cast Mg-3.0Nd-0.3Zn-0.6Zr Alloy, J. Mater. Process. Technol. 267 (2019) 366–375. https://doi.org/10.1016/j.jmatprotec.2018.12.032.

[17] J. Campbell, Castings - 2nd Edition, Butterworth-Heinemann, 2002.

[18] E.J. Vinarcik, High Integrity Die Casting Processes, Wiley, New York, 2003.

[19] S. Bhagavath, B. Cai, R. Atwood, M. Li, B. Ghaffari, P.D. Lee, S. Karagadde, Combined Deformation and Solidification-Driven Porosity Formation in Aluminum Alloys, Metall. Mat. Trans A. 50 (2019) 4891–4899. https://doi.org/10.1007/s11661-019-05378-8.

[20] K.M. Kareh, P.D. Lee, R.C. Atwood, T. Connolley, C.M. Gourlay, Revealing the Micromechanisms Behind Semi-Solid Metal Deformation with Time-Resolved X-Ray Tomography, Nat. Commun. 5 (2014) 4464. https://doi.org/10.1038/ncomms5464.

[21] K.M. Kareh, P.D. Lee, R.C. Atwood, T. Connolley, C.M. Gourlay, Pore Behaviour During Semi-Solid Alloy Compression: Insights into Defect Creation Under Pressure, Scripta Mater. 89 (2014) 73–76. https://doi.org/10.1016/j.scriptamat.2014.06.033.

[22] C.H. Cáceres, B.I. Selling, Casting defects and the Tensile Properties of an AlSiMg Alloy, Mater. Sci. Eng.: A 220 (1996) 109–116. https://doi.org/10.1016/S0921-5093(96)10433-0.

[23] J.P. Weiler, J.T. Wood, R.J. Klassen, E. Maire, R. Berkmortel, G. Wang, Relationship Between Internal Porosity and Fracture Strength of Die-Cast Magnesium AM60B Alloy, Mater. Sci. Eng.: A 395 (2005) 315–322. https://doi.org/10.1016/j.msea.2004.12.042.

[24] J.P. Weiler, J.T. Wood, Modeling Fracture Properties in a Die-Cast AM60B Magnesium Alloy I—Analytical Failure Model, Mater. Sci. Eng.: A 527 (2009) 25–31. https://doi.org/10.1016/j.msea.2009.08.060.

[25] E. Battaglia, F. Bonollo, P. Ferro, Experimental Damage Criterion for Static and Fatigue Life Assessment of Commercial Aluminum Alloy Die Castings, Metall. Mater. Trans. A 48 (2017) 2574–2583. https://doi.org/10.1007/s11661-017-4038-5.

[26] M. Tiryakioğlu, Relationship between Defect Size and Fatigue Life Distributions in Al-7 Pct Si-Mg Alloy Castings, Metall. Mater. Trans. A 40 (2009) 1623–1630. https://doi.org/10.1007/s11661-009-9847-8.

[27] X. Li, S.M. Xiong, Z. Guo, Improved Mechanical Properties in Vacuum-Assist High-Pressure Die Casting Of AZ91D Alloy, J. Mater. Process. Technol. 231 (2016) 1–7. https://doi.org/10.1016/j.jmatprotec.2015.12.005.

[28] X.P. Niu, B.H. Hu, I. Pinwill, H. Li, Vacuum Assisted High Pressure Die Casting of Aluminium alloys, J. Mater. Process. Technol. 105 (2000) 119–127. https://doi.org/10.1016/S0924-0136(00)00545-8.

Chapter 2: Literature Review

2.1 Conventional High-Pressure Die Casting

We can divide conventional HPDC processes into two distinct categories depending on the design of the metal injection system. Fig. 2.1(a) shows the cold chamber HPDC process, in which the metal injection system is isolated from the holding furnace. Liquid metal is metered into the shot sleeve, either manually using a transfer ladle, or automatically using a dosing system. Fig. 2.1(b) shows the hot chamber HPDC process, in which the metal injection system is immersed in a reservoir of molten metal. This approach aims to increase productivity by reducing the distance travelled by the liquid metal during dosing. However, the high melting point of aluminium alloys can lead to severe degradation of the metal injection system when used in this way. When working with aluminium alloys, die-casters prefer to adopt a cold chamber configuration.

Fig. 2.2 shows a typical cycle of the cold chamber HPDC process, in which: (i) liquid metal is poured into the shot sleeve of the HPDC machine; (ii) a hydraulically actuated plunger slowly pushes the molten metal into the runner system; (iii) the plunger moves at high speed to inject the molten metal into the die cavity; (iv) the casting solidifies under an applied pressure of 30∼100 MPa [1]; (v) the die opens and the part is ejected; (vi) the die is sprayed with a coolant, and blown with air; (vii) the die closes, and the cycle repeats. Parts (ii), (iii), and (iv) are often referred to as the ‘slow-shot stage’, the ‘fast-shot stage’, and the ‘intensification stage’, respectively. Cycle times will vary depending on the size of the casting. For example, the cycle time for a V6 engine block—which weighs roughly 50 kg—is approximately 90 s [2].

Despite its benefits, the conventional HPDC process has one major limitation: the mechanical properties of die-castings are notoriously inconsistent. This inconsistency leads to large scrap rates and increased safety factors for component design. Though the mechanical properties of die-castings have been linked to various casting defects—such as porosity [3–6] and oxide films [7,8]—the underlying cause of variability is presently unknown.

[This space intentionally left blank]

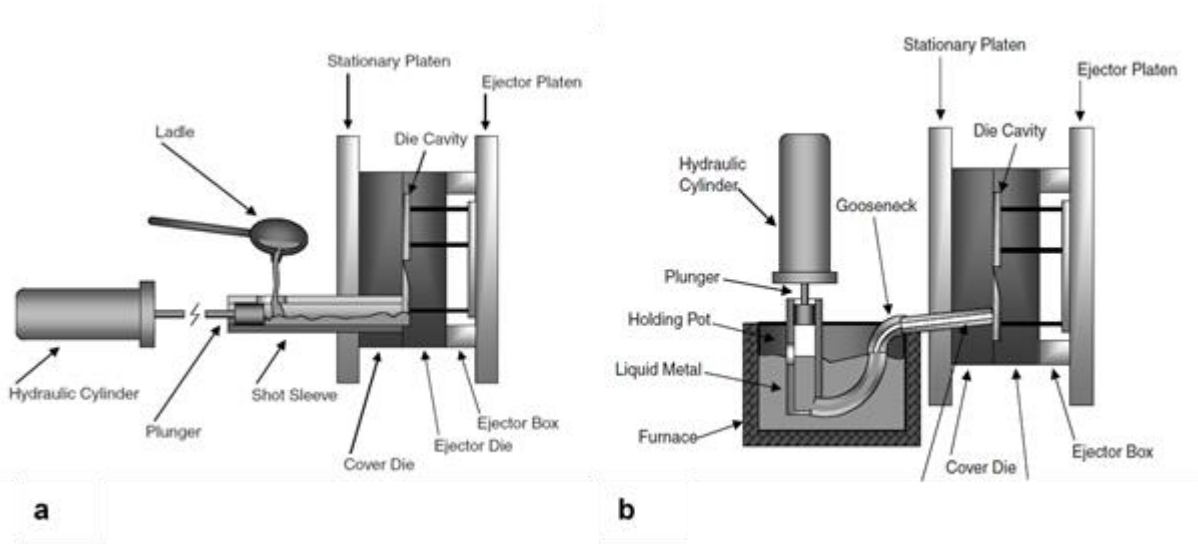

Fig. 2.1 Graphical illustrations of the (a) cold chamber, and (b) hot chamber metal injection systems [9].

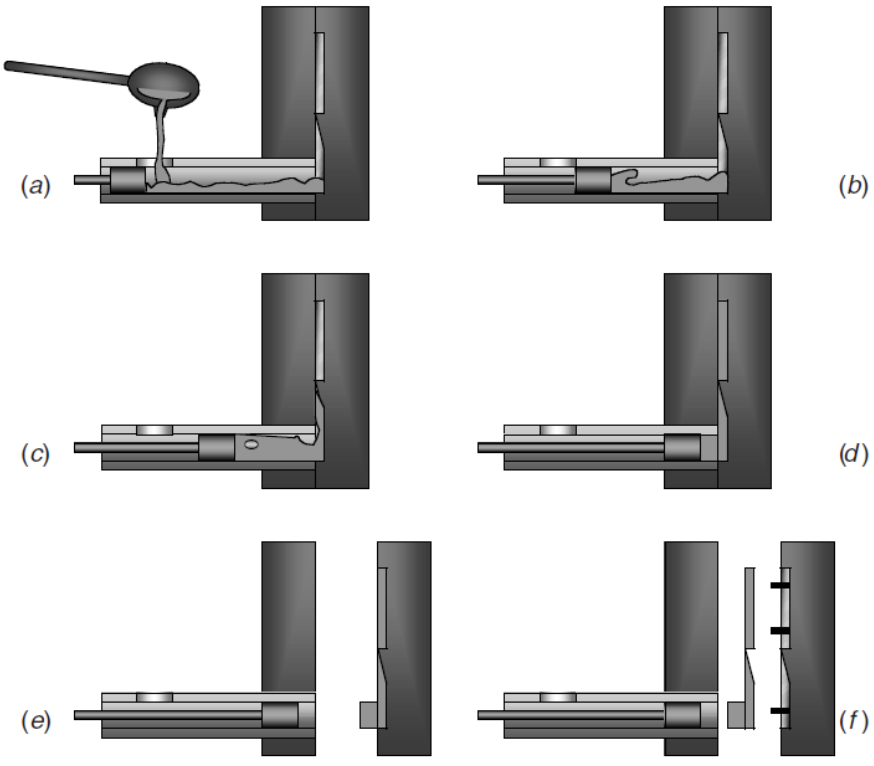

Fig. 2.2 A typical cold chamber HPDC cycle, in which: (a) molten metal is poured into the shot sleeve; (b-c) the plunger slowly pushes molten metal into the runner system; (d) the melt is injected at high speed into a sealed mould cavity, and then solidifies under an applied pressure; (e) the die opens, and; (f) the part is ejected from the mould [9].

2.2 Vacuum-Assisted High-Pressure Die Casting

Porosity is one of the most common defects in die-cast structures. This observation has led to the development of several 'high-integrity' HPDC processes that aim to reduce the amount of porosity in the casting while retaining the desirable characteristics of HPDC. In this section we will discuss the most commercially viable of these high-integrity processes: vacuum-assisted HPDC. This process relies on the use of an external vacuum system to evacuate the mould cavity prior to liquid metal injection. Other high-integrity processes, such as semi-solid casting and squeeze casting, are discussed at lengh in reference [9].

In vacuum-assisted HPDC, mould filling and evacuation operate in parallel. A typical casting cycle consists of the following: (i) initiation of the slow-shot stage; (ii) opening of the vacuum valve; (iii) evacuation of the shot sleeve and die cavity; (iv) closing of the vacuum valve; (v) the fast-shot stage; (vi) the intensification stage; (vii) ejection of the cast component; (viii) die spraying and blowing, and; (ix) die closing. The cycle then repeats.

To achieve optimal extraction, the vacuum shut-off valve should be located at the final region of the cavity to contact the liquid metal, as illustrated in Fig. 2.3. Koya et al. [10] demonstrate that fluid flow is partially atomized at the time of injection, provided a sufficiently high J-factor. The J-factor is determined by the Van Rens equation and indicates the initial flow regime during die filling:

$$J = D \cdot \rho \cdot V_g^{1.71} \tag{2.1}$$

where V_g is the gate velocity; $D = ab/(a+b)$ is the orifice radius, for a gate of width a and thickness b; and ρ is the density of the alloy. Atomization is attributed to two phenomena [10,11]: the collision of newly accelerated high-speed material and previously injected low speed material, which causes the front of the liquid jet to open like an umbrella; and surface fluctuations of the liquid jet, which cause droplets of molten metal to separate from the liquid column. A consequence of atomization is that the last-to-fill region is usually located near to the ingate, as shown in Fig. 2.3. Numerical modelling may be employed to locate the optimum location for the vacuum shut-off valve that achieves a minimum vacuum pressure prior to liquid metal injection.

[This space intentionally left blank]

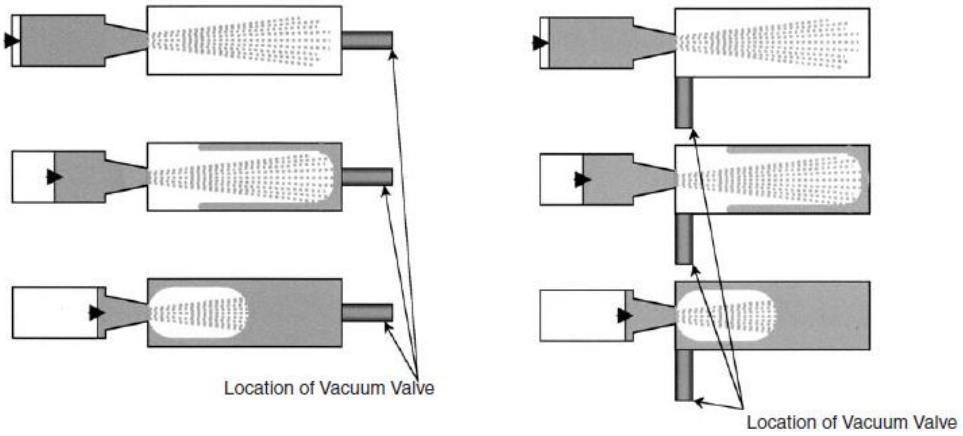

Fig. 2.3 Graphical illustration of atomized flow, highlighting improper (left) and proper (right) vacuum valve placement [9].

Successful evacuation of the cavity is highly dependent on the kinematics of the plunger during the slow-shot stage. In the slow-shot stage, the plunger slowly accelerates to form a wave of liquid metal that just reaches the ceiling of the shot chamber; the plunger then moves at a constant speed until the entire chamber is filled with molten metal. An ideal wave is such that air is pushed ahead of the liquid front allowing for its subsequent evacuation from the die cavity. Examples of proper and improper wave forms are shown in Fig. 2.4.

A decrease in vacuum pressure is accompanied by a decrease in pore size and an improvement in casting consistency [12]. Despite this, vacuum levels below 50 mbar are seldom reported in the literature, with the exceptions of Dong et al. who achieved a vacuum level of 19 mbar [3]. The high productivity and thermal cycling associated with pressure die casting can lead to gradual leakage of vacuum following poor die maintenance and improper sealing. Surface deformation along the parting line and ejector guides are inherent risks to excessive vacuum leakage. This introduces a requirement for regular maintenance, which incurs additional cost.

Studies have suggested that the addition of vacuum can significantly reduce the variability in mechanical properties of die-cast structures, particularly after subsequent solution and ageing treatments [3,12–14]. However, the comparisons between vacuum-assisted HPDC and conventional HPDC are often biased. For example, when comparing vacuum-assisted HPDC and conventional HPDC, researchers tend to use the same processing parameters—processing parameters that are often tailored to the requirements of the vacuum system. In other cases, the processing parameters are not provided, and the experiments are irreproducible.

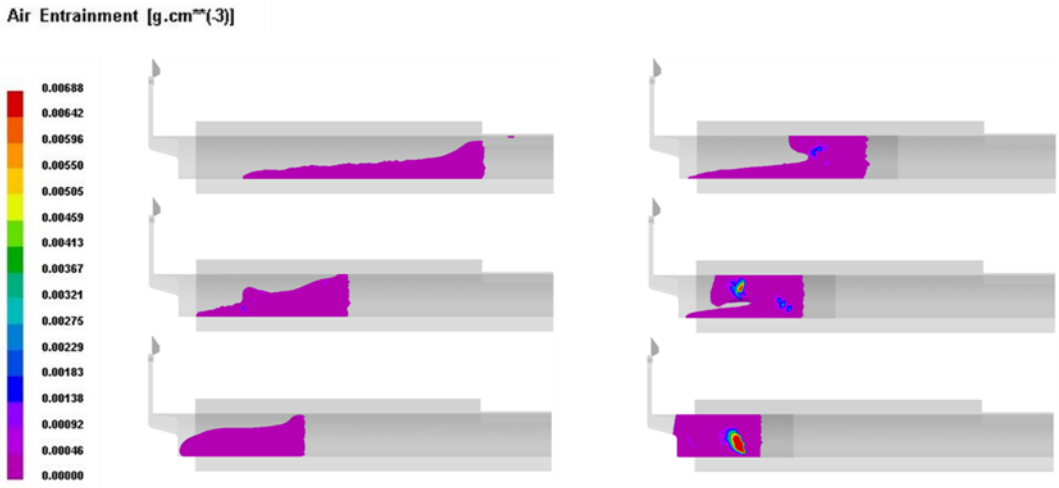

Fig. 2.4 ProCAST simulations of air entrapment during the slow shot phase, showing proper (left) and improper (right) wave forms. For the improper case, the wave reflects against the ceiling of the shot chamber and rolls over, encapsulating air. Courtesy of Dr. Kun Dou.

2.3 Solidification in High-Pressure Die Casting

2.3.1 Solidification in the Shot Chamber

Solidification commences when the liquid metal contacts the shot chamber wall; primary α-Al crystals nucleate and grow in thermally undercooled regions of the chamber wall and on the plunger tip. These primary α-Al crystals are coarse (30~300 μm [15]) and possess a dendritic morphology. Fe-rich intermetallic phases also precipitate while the melt is retained in the shot chamber. The melt thus resembles a multi-phase mixture consisting of up to 30 vol. % solid [16]. For the sake of convenience, the suffix X_1 will be used to denote solidification in the shot chamber; the suffix X_2 will denote solidification in the die cavity.

Several factors can influence the extent of solidification in the shot chamber, including: the initial melt superheat; the initial filling fraction; the interfacial heat transfer coefficient; and the chemical composition of the alloy. Furthermore, the interfacial heat transfer coefficient can vary between 1600~5500 $Wm^{-2}K^{-1}$ depending on the location in the shot sleeve [17]. An increase in the volume fraction of primary α-Al_1 crystals is accompanied by an increase in the apparent viscosity of the melt. By altering the rheology of the solidifying mush, a large population of α-Al_1 crystals may act to inhibit the transmission of intensification pressure and the feeding of shrinkage strains [18]. This suggests that although these primary α-Al_1 crystals may not be harmful themselves, their influence on the subsequent defect population may induce some degree of variability in mechanical properties. Similar observations have been made in reference [19]; however, further work is required to understand this phenomenon.

2.3.2 Solidification in the Die Cavity

During die filling, the melt is propelled at high speeds through a narrow orifice system, where it is subject to shear rates in the order of $10^4 \sim 10^5$ s^{-1} [1]. The resultant flow is highly turbulent, and strongly three-dimensional. Particles and aggregates suspended in this flow will experience large transient stresses, which may be large enough to induce breakage. Scientists have suggested that the shear rates encountered during die filling are large enough to cause oxides [8] and primary α-Al_1 crystals [14] to fragment. These fragments would act as suitable substrates for heterogeneous nucleation of α-Al_2 grains [20]. However, more experimental evidence is required to test these hypotheses.

Primary α-Al_2 grains form in the die cavity. These grains are relatively small ($\sim$10 μm [15]) and possess a globular-rosette morphology. These primary α-Al_2 grains are much smaller than their α-Al_1 counterparts, due to the higher cooling rates in the die cavity (100$\sim$1000 Ks^{-1} [15]) compared to those the shot chamber ($\sim$10 Ks^{-1} [15]). Fe-rich intermetallic phases will also precipitate in the die cavity. These phases are much smaller than their shot chamber solidified counterparts and typically possess a fine polyhedral morphology.

2.4 Casting Defects

2.4.1 Gas Porosity

Porosity is one of the most common defects in conventional die-castings. Porosity is traditionally attributed to solidification shrinkage, the expansion of gaseous phases, or a combination of the two [9,20]. The reduced solubility of hydrogen in liquid aluminium is believed to be a key factor influencing the formation of gas porosity. Fisher [21] elegantly quantifies the work associated with the reversible formation of a vapour bubble in the interior of a liquid. The total energy required for this homogeneous nucleation event consists of three components: the work required to push back a volume of liquid; the energy required for the formation, and growth, of a new gas-liquid interface; and the work required to fill the bubble with vapour or gas [20]. This work is provided by a negative pressure in the liquid. Plotting the potential energy of the system against the bubble radius, a maximum is observed. This maximum represents the energy threshold for homogeneous nucleation [21]. The critical radius r^* associated with this energy barrier is given by:

$$r^* = \frac{2\gamma}{\Delta P} \tag{2.2}$$

where γ is the interfacial energy per unit area, and ΔP is the pressure difference across the gas-liquid interface [20]. The size of the bubble determines whether it will grow, or shrink. Bubbles with a radius less than r^* require additional energy for growth, and tend to disappear; bubbles with a radius greater than r^* grow with decreasing energy [21]. However, the homogeneous nucleation of a bubble larger than r^*—in a metallic melt initially free of microbubbles—requires an exceptionally rare chain of favourable energy fluctuations. It is more likely that a pore will nucleate heterogeneously on some poorly wetted interface. The heterogeneous nucleation of gas pores is discussed at length in references [20–22]. Although the energy threshold for heterogeneous nucleation is much lower than that for homogeneous nucleation, the pressures required for these 'classical' nucleation events are practically unattainable in liquid aluminium. Campbell [20] suggests that oxide bifilms possess the potential to nucleate gas porosity with minimal difficulty: hydrogen diffuses into the air gap between the unbonded oxides, causing the bifilm to unfurl and inflate, like a balloon.

Rotary degassing, which involves the bubbling of an inert purge gas into the molten metal, is commonly used in foundries to reduce hydrogen levels in aluminium alloy melts. In this process, a smaller purge bubble equates to a higher degassing efficiency; however, it is difficult to obtain a bubble diameter below 10 mm [23]. The process therefore requires a considerably high argon flow rate between 4-10 l/min and a significant processing time between 15-30 min to achieve an industrially accepted hydrogen level below 0.15 cm^3/100g [24]. High rotor speeds may result in a reduced bubble diameter; however, the increased surface turbulence and vortex introduced at these speeds severely deteriorates the quality of the melt by entraining harmful oxides [25].

Water-based lubricants are often applied to the die to prevent the casting from sticking to the mould. Oil-based lubricants are also applied to the plunger tip to prevent wear and seizure. When these lubricants come into contact with liquid metal, they will either evaporate or burn, releasing gas into their environment. This gas may be engulfed by the liquid, causing the local gas content of the melt to increase [26]. This contribution to the total gas content is expected to increase as the geometry of the casting becomes more complex; it is more difficult to vent an intricate die as opposed to one with a simple geometry.

2.4.2 Shrinkage Porosity

As the liquid metal cools, and eventually solidifies, it undergoes three contractions due to the dissimilar densities of the liquid and solid phases: liquid contraction, solidification contraction, and solid-state contraction. Liquid contraction is straightforward to remedy provided there is sufficient liquid to compensate for the small reduction in volume. Solidification contraction, however, raises

two major concerns: it introduces a requirement for feeding, defined by Campbell as “any process that allows for the compensation of solidification contraction by the motion of liquid or solid” [20]; and the formation of shrinkage porosity, which is a result of inadequate feeding. The final contraction occurs in the solid-state, during which the casting attempts to reduce its size while being constrained by the mould and any regions of the casting that may have solidified and cooled already.

The nucleation of shrinkage pores is widely overlooked; there is a common misconception that shrinkage cavities simply exist due to the volume deficit induced by solidification contraction. Shrinkage cavities nucleate at high solid fractions, when the crystal packing density is high and the mushy zone is less permeable. To accommodate the volume deficit induced by solidification contraction, the liquid expands, placing it in a state of internal tension [20,22]. This negative pressure draws liquid into the interstitial space, leading to a local enrichment of hydrogen [27]. Cavitation may occur when the local gas concentration exceeds the solubility of the gas in the liquid [28,29]. Furthermore, it is well known that the solubility of a gas, in a liquid, decreases with liquid pressure and temperature. Suitable nuclei for pores include non-metallic inclusions and the non-wetted surfaces of oxide bifilms [20]. Once nucleated, a growing pore will retain its spherical shape until it comes into contact with solid, at which point further growth can only take place in the interdendritic channels [27]. Thus, shrinkage cavities are often observed to possess a highly irregular and tortuous morphology.

2.4.3 Dilatant Shear Bands

During the equiaxed solidification of metallic alloys, the liquid to solid transition exhibits a continuous development in mechanical behaviour from a Newtonian fluid to a polycrystalline viscoplastic solid [30]. Crystals are initially dispersed in the liquid, with subsequent growth leading to an increase in the volumetric fraction of solid (f_s). At some critical solid fraction (f_s^{coh}) these crystals impinge on one another, forming an intertwined network of solid [30–32]. This phenomenon is often termed coherency and marks the transition from mass to interdendritic feeding. Following coherency, the solidifying alloy has been shown to develop measurable compressive and shear strength, however, it is unable to transmit tensile strain [30,33,34]. Numerous studies involving vane rheometry and direct shear cell experiments have demonstrated that equiaxed solidifying alloys at $f_s \geq f_s^{coh}$ share rheological similarities with compacted granular materials such as water-saturated sand [30,31,33–35]. The grains in a compacted granular assembly respond to compressive and shear loads by rearranging to form regions of contraction and dilation. In equiaxed solidifying alloys, such as Al7Si0.3Mg and Mg9Al0.7Zn, an increase in shear stress is accompanied by a volumetric expansion—Reynold’s dilatancy [30]. As the shear stress increases, dilatancy develops in

a highly anisotropic manner, ultimately localising within a narrow band following the casting contour. The negative pressure induced by dilatancy results in positive macrosegregation, provided sufficient liquid can be drawn to the dilating band. Interdendritic porosity forms in the band when insufficient liquid is available for feeding [30]. These bands of interdendritic porosity have been shown to be a major source of failure in Mg alloy die-castings [36].

The complexity involved in describing the deformation of semi-solid alloys at $f_s \geq f_s^{coh}$ can be embodied by a range of interrelated phenomena, such as the self-organization of grains, the nonlinear dynamics of grain rearrangement, and the coexistence of solid-like and liquid-like behaviours within the mushy zone [32,37]. By performing synchrotron X-ray radiography experiments on thin-sample direct shear cells, Gourlay et al. [38] observed the mesoscopic deformation of semisolid aluminium alloys and steels. Fig. 2.5 shows the deformation of a globular Al-15Cu alloy specimen at roughly 70 % solid, measured in one such radiography experiment. In addition to providing direct evidence of shear-induced dilation in solidifying alloys as a result of grain rearrangement, this series of radiographs also highlights how crystal size and morphology influences dilatancy.

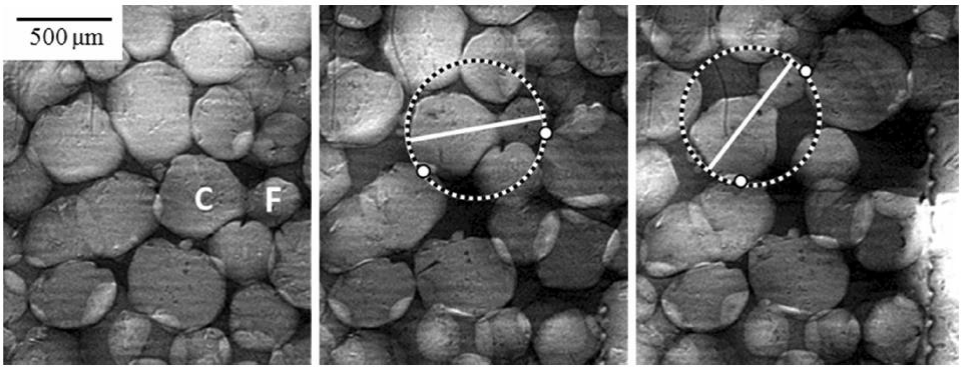

Fig. 2.5 Time-resolved synchrotron X-ray radiographs depicting the deformation of a globular Al-15Cu alloy at approx. 70% solid in a thin-sample direct shear cell experiment. The push plate is located on the right-hand side of each image, and is moving upwards [38].

Tordesillas [39] elegantly describes the evolution of stress-dilatancy within a cohesionless granular assembly, demonstrating that the underlying mechanism is one of cyclic jamming-unjamming events governed by the collective buckling of so-called ‘force chains’ (self-organization of particles into load-bearing structures, which align to the principal stress axis prior to collapse). Examples of force chains in a granular medium are shown in Fig. 2.6(a) for an assembly of photo-elastic discs. Within a dense granular material, stress is heterogeneously transmitted along a two-phase network of contacts [40]. The strong network is a subnetwork comprising chains of highly stressed particles,

which carry the majority of the applied load. The complementary weak network consists of contacts that experience a below average force and provides lateral support to existing force chains. Initial deformation of the granular medium is predominately affine, with potential energy increasing with strain [39,41]. At the onset of non-affine deformation, force chains establish and align to the principal stress axis. The absence of force chain buckling is accompanied by a global dilation of the granular assembly [37,39,41]. Force chain buckling initiates just prior to the peak shear stress, generating large voids between neighbouring columns [39,41]. At the maximum shear stress, buckling events propagate along the shear plane, causing dilatancy to rapidly localise into a narrow band [42–44]—as illustrated in Fig. 2.6(b). When a force chain fails (unjamming event), the energy stored at its contacts is dissipated to neighbouring particles from the weak network, encouraging the formation of new force chains or the reinforcement of existing ones (jamming event) [39]. The shear band continues to develop, until these cyclic jamming-unjamming events cause the band to attain a residual state, in which the collapse of existing force chains is in equilibrium with the generation of new ones [39]. Although the granular mechanics community has extensively studied this phenomenon, little evidence exists that quantitatively links this literature to the equiaxed solidification of metallic alloys.

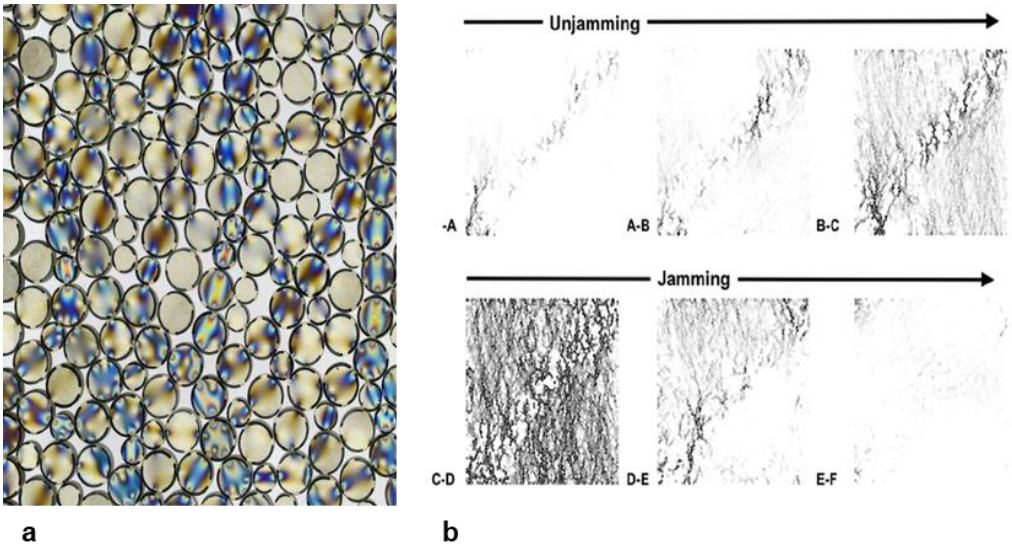

Fig. 2.6 (a) Assembly of photo-elastic disks showing the self-organization of particles into load-bearing structures, i.e. force chains [45]; (b) energy flow in a granular medium at consecutive strain intervals. A particle is coloured according to the magnitude of the drop in potential energy: black (highest) and white (zero). Global unjamming can be seen to nucleate in the upper right-hand corner of A-B and rapidly propagates across the shear plane [39].

2.5 X-ray Tomography

X-ray computed tomography (CT) is a non-destructive evaluation technique that allows one to visualise the internal structure of an object. CT involves the acquisition of multiple radiographic projections while the object rotates between 0 ° and either 180 ° or 360 °. These projections are mathematically reconstructed to visualise the object in three-dimensional space. CT has historically been used as a medical diagnostic tool, with most research programmes aiming to reduce the data acquisition time to within the breath-holding range of a typical patient. Such studies led to new geometric configurations and enhanced image reconstruction algorithms. Since then, CT has gained industrial importance as a non-destructive evaluation technique for high-value manufacturing. This is especially true for parts prone to internal porosity, such as those produced by HPDC or additive manufacturing. Here, we introduce the fundamentals of X-ray tomography, namely data acquisition and image reconstruction. This aims to provide an unfamiliar reader with sufficient knowledge to follow later discussions on X-ray attenuation and defect characterisation. Few resources are presently available that discuss the role of X-ray tomography in the material sciences—the interested reader is referred to the book by Baruchel et al. [46].

2.5.1 X-ray Sources

X-rays are electromagnetic waveforms; whose wavelength varies from several picometers to several nanometers. X-ray photons are produced when high speed electrons impinge on matter. The Planck-Einstein relation states that the energy of each photon E is proportional to its frequency v

$$E = hv = hc/\lambda,$$

(2.3)

where h is Planck's constant (6.63x10^{-34} Js), c is the speed of light in vacuum (3x10^{8} ms^{-1}), and λ the wavelength of the incident X-ray. For convenience, we express X-ray energies in electron volts (eV), where an electron gains 1 eV (1.602x10^{-19} J) of kinetic energy as it accelerates across an electric potential of 1 V [47]. X-ray sources may be classified as either monochromatic or polychromatic, depending on their energetic nature [48]: monochromatic sources produce X-rays with a single characteristic energy; polychromatic sources produce X-rays with a continuous spectrum of energies, and characteristic energy peaks. X-ray tubes are typically used in CT scanners to generate polychromatic X-rays (Fig. 2.7). These X-ray sources comprise an evacuated glass tube, housing two electrodes and a focusing cup. A coiled tungsten filament forms the cathode and emits electrons through thermionic emission. A focusing cup concentrates the electron beam onto a small area of

the target material. Tungsten is generally used as a target material, in part due to its relatively large thermal conductivity, but more so due to its high atomic number of 74.

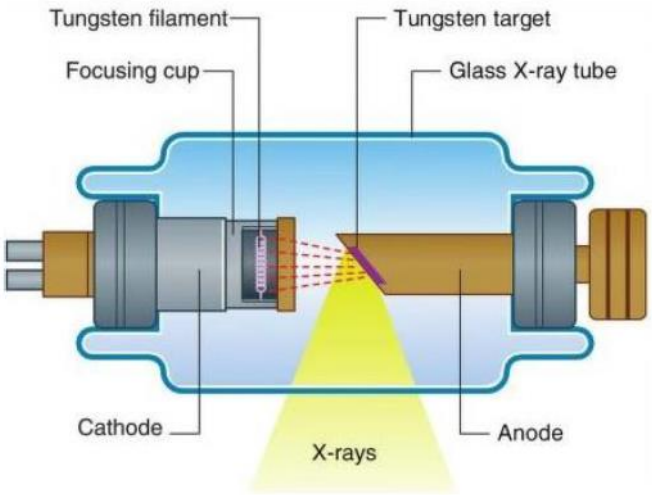

Fig. 2.7 Schematic diagram of an X-ray tube [47].

2.5.2 X-ray Detectors

X-ray detectors are generally based on scintillation, in which X-ray energy is first converted to visible light by fluorescence, and then to an electrical signal via an array of photodiodes or photomultipliers [47]. Alternatively, thicker scintillators may be optically coupled to a CCD camera via an optical lens [46,48]. Among the fluorescent materials used in X-ray detectors, the most popular include NaI, Gd_2O_3, and Tb_2O_3.

An X-ray can interact with matter in several ways. While a detailed description of these interactions is beyond the scope of this thesis, it is important to understand that an X-ray beam is attenuated as it traverses matter: that is, the intensity of an X-ray beam decreases as it passes through an object. This attenuation is described by the Beer-Lambert law for a monoenergetic X-ray beam and a material of uniform density and atomic number [47]:

$$I = I_0 e^{-\mu L}, \tag{2.4}$$

where I and I_0 are the transmitted and incident X-ray intensities, μ is the linear attenuation coefficient and L is the thickness of the material. It is clear from (2.4) that materials with high μ will be more attenuating than those with low μ.

2.5.3 Geometric Configurations

The first commercially viable CT scanner was developed by Hounsfield in 1967. This system performed linear scans on a rotating specimen, and took a total of nine days to produce an image. These first-generation systems, often termed translate-rotate systems, consist of a single source-detector pair which measures one ray-sum at a time—as illustrated in Fig. 2.8(a) [47]. First, the object translates along a linear path, acquiring individual measurements at predefined intervals. The object then rotates at angular increments between 0 and 180° to collect enough projections to reconstruct the tomographic plane. The stage then translates in the z-direction to acquire projection data for the remaining planes. Although first-generation scanners have a good spatial resolution and produce artefact-free images, the data acquisition times of these scanners are impractically high.

Second-generation systems were developed in an attempt to reduce the data acquisition times of first-generation scanners. This configuration introduced a linear array of detector cells, while maintaining the familiar translate-rotate configuration of first-generation scanners (Fig. 2.8(b)). The X-ray beam thus resembles a well-collimated fan, with its apex at the X-ray source. Measurements are acquired at angular intervals equal to the fan-angle, thereby drastically reducing the data acquisition times of first-generation scanners. As the beam is now divergent, a complete turn is required to reconstruct the plane.

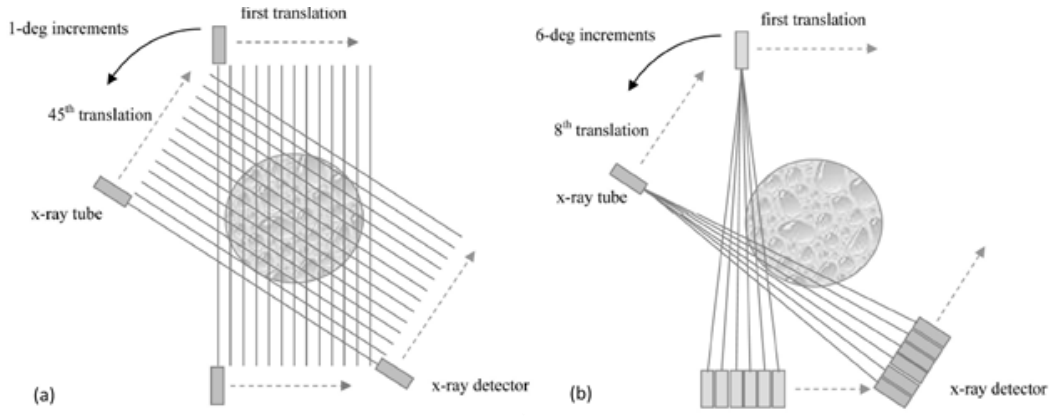

Fig. 2.8 Geometric configuration of (a) first-generation and (b) second-generation CT scanners [47].

Third-generation scanners further reduce data acquisition times by eliminating the linear motion associated with first- and second-generation systems. In third-generation systems, a linear (or areal) detector array is placed on an arc concentric to the X-ray source, as shown in Fig. 2.9(a). The geometry of the beam depends on the detector array: for a linear detector array, the X-ray beam resembles a well-collimated fan; for an areal detector array, the X-ray beam resembles a well-collimated cone. One distinct feature of third-generations systems, is that the entire object is

contained within the detectors field of view. The data required to reconstruct a tomographic plane (for a linear detector array)—or the entire three-dimensional volume (for an areal detector array)—can, therefore, be obtained from a single rotation of the object. Despite this, third-generation scanners have several disadvantages, such as increased noise and artefacts [48]. This introduces a requirement for additional data processing steps, which incurs additional cost. Fourth-generation scanners have been developed for medical applications, wherein an enclosed ring of detectors remains stationary during operation and the X-ray source rotates around the patient, as illustrated in Fig. 2.9(b). In this case the beam again resembles a well-collimated fan or cone; however, the apex is now the detector as opposed to the X-ray source. While fourth-generation systems have achieved great success as a medical diagnostic tool, they are seldom used in engineering applications. The interested reader is referred to [47,48].

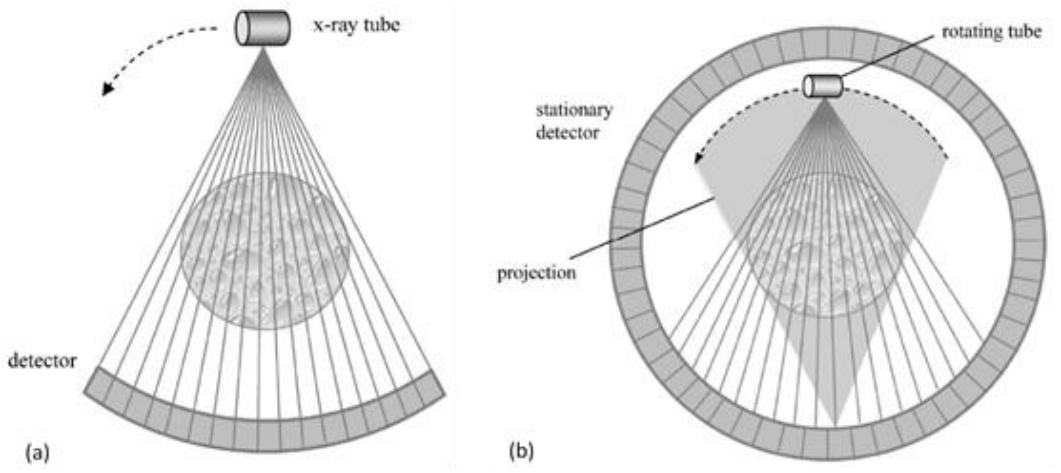

Fig. 2.9 Geometric configuration of (a) third-generation and (b) fourth-generation CT scanners. In both configurations, the entire object is contained within the detectors field of view [47].

2.5.4 Measurement of Line Integrals

Previously, we stated that X-rays are attenuated as they traverse matter. We also introduced the Beer-lambert law, equation (2.4), which describes the attenuating behaviour of a homogeneous material. This concept is also illustrated in Fig. 2.10(a). Although equation (2.4) may hold for a material with uniform density and atomic number, these simplifications are seldom valid in practice. If we now consider the case of an inhomogeneous object subject to a monoenergetic X-ray beam, the overall attenuation may be evaluated by dividing the object into a series of finite elements—as illustrated in Fig. 2.10(b). Provided these elements are sufficiently small in size, we may regard each element as a uniform object with constant linear attenuation coefficient μ_i.

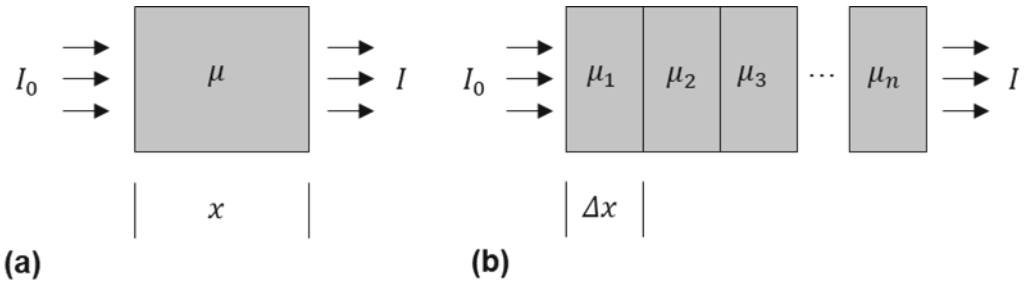

Fig. 2.10 Attenuating behaviour of a monochromatic X-ray beam as it traverses a (a) homogeneous, and (b) an inhomogeneous object [47].

Consider the boundary conditions of two adjacent elements. The arriving flux of one element is the departing flux from the previous element along the ray-path. Therefore, we may apply (2.4) in a cascade fashion:

$$I = I_0 \exp\left(-\sum_{n=1}^{N} \mu_n \Delta x\right), \tag{2.5}$$

where Δx denotes the element thickness. As Δx becomes infinitesimal, the summation term in (2.5) tends towards an integration over the ray-path. By dividing both sides of (2.5) by I_0 and taking negative logarithms, we obtain an expression for the line integral:

$$p = -\ln\left(\frac{I}{I_0}\right) = \int_L \mu(x)\, dx, \tag{2.6}$$

where p is commonly termed the projection measurement. Although (2.6) suffices for a monochromatic X-ray source, it is no longer valid for X-ray beams of a polyenergetic nature. This is due to the beam-hardening phenomenon, in which the linear relationship between the projection measurement and the sample thickness no longer exists [47]. As most industrial CT systems utilise a polychromatic X-ray source, computationally intensive pre-processing and post processing steps are required to account for non-ideal data. Rather than measuring the incident and transmitted X-ray intensities, it is more convenient to measure the number of photons emitted by the source N_0 and the number of photons transmitted along the ray-path N [46]. Accordingly, (2.6) may be written in terms of the measured photon counts as

$$p = -\ln\left(\frac{N}{N_0}\right) = \int_L \mu(x)\, dx. \tag{2.7}$$

We may now introduce the tomographic reconstruction problem: given a set of projection measurements, how can we estimate the attenuation distribution of the object, and thus visualise its internal structure?

2.5.5 The Radon Transform and Sinogram Space

The mathematical framework for tomographic reconstruction was developed in 1917 by the Austrian mathematician Johann Radon, in which he introduced the Radon transform on Euclidean space, along with its inverse transformation. The Radon transform $\mathcal{R}$ of some object function f is

$$\check{f} = \mathcal{R}f, \tag{2.8}$$

where $\check{f}$ comprises a set of projections. The object function f can be defined in any n-dimensional Euclidean space $\mathbb{R}^n$, with the Radon transform of f determined by integrating f over all hyperplanes in $\mathbb{R}^n$ [49]. The Radon transform of f when defined in $\mathbb{R}^2$ and $\mathbb{R}^3$ are of practical importance: when f is defined in $\mathbb{R}^2$, $\check{f}$ is given by the line integrals of f; when f is defined in $\mathbb{R}^3$, $\check{f}$ is given by the surface integrals of f over two-dimensional hyperplanes.

Returning to tomographic reconstruction, let us now consider a cross-sectional plane through an arbitrary three-dimensional object [46]. We begin by defining a Cartesian coordinate system comprising x, y, and z axes. If the sectional plane is orthogonal to the z-axis, we may express the attenuation coefficient μ as a function of x and y. Although it is common in industrial CT for the measurement system to remain stationary and for the sample to rotate, the image reconstruction problem is greatly simplified if we instead attach a reference system to the object itself, as shown in Fig. 2.11. In this reference system, the origin is placed on the axis-of-rotation and a point M is defined by coordinates (x, y). As with previous examples, we assume a first-generation system with a monochromatic source. A source-detector ray is defined by the polar coordinates (r, θ), where r is the distance from the origin to the ray and θ the angle between the x-axis and the perpendicular to the ray. It follows then, that the projection measurement p along a ray (r, θ) is given by:

$$p(r,\theta) = -\ln\left(\frac{N}{N_0}\right) = \int_{M \in ray\ (r,\theta)} \mu(M)\, dM \tag{2.9}$$

Note that (2.9) denotes a sampling of the Radon transform for the function μ. For tomographic reconstruction, we must acquire enough projections to provide a valid representation of the continuous Radon transform.

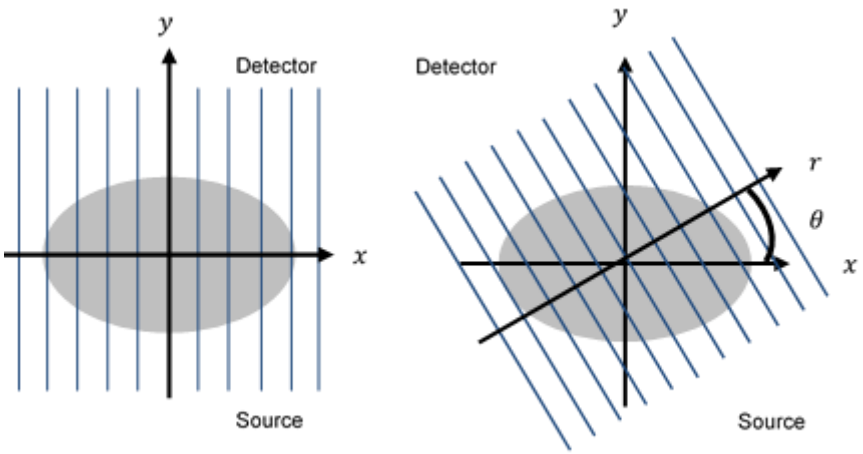

Fig. 2.11 Schematic diagram of the image reconstruction problem [46]. A rotating reference system is attached to the object. A source-detector ray (blue line) is defined by the polar coordinates (r, θ), where r is the distance from the origin to the ray and θ the angle between the x-axis and the perpendicular to the ray.

One important property of the Radon transform is symmetry. In first-generation systems, a projection acquired at 180° is equivalent to a projection acquired at 360° [48]. For convenience, the Radon transform is commonly visualised as a sinogram (Fig. 2.12). In the sinogram space, r occupies the horizontal axis, and θ the vertical axis. The projection of a point M traces a sinusoidal path in the sinogram—provided that M does not lie on the axis-of-rotation. As any object can be well approximated by a sufficiently dense point cloud in $\mathbb{R}^3$, the Radon transform of the object will resemble a collage of overlapping sinusoidal curves in the sinogram space. Abnormalities in the CT system, such as defective detector modules or a temporary malfunction of the X-ray tube, can be easily identified from the sinogram, manifesting as vertical and horizontal lines, respectively [47].

[This space intentionally left blank]

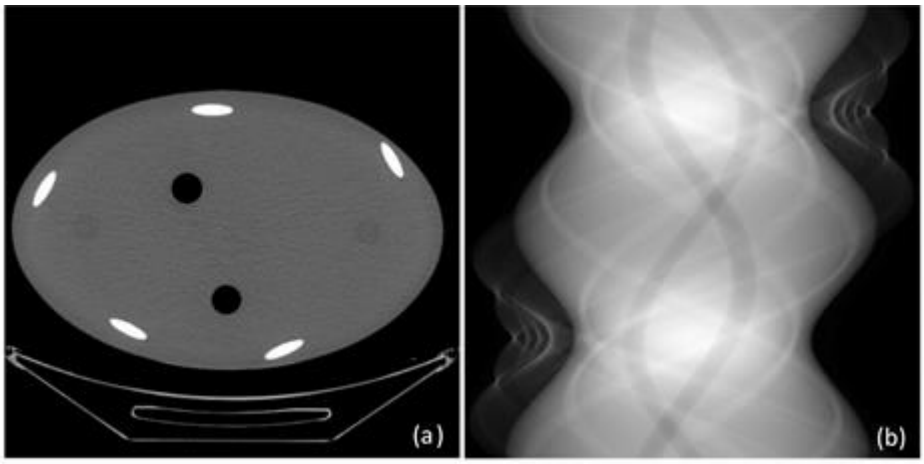

Fig. 2.12 (a) Cross section of a body phantom, and (b) its sinogram [47].

2.5.6 The Fourier-Slice Theorem

The Fourier-slice theorem forms the basis of many tomographic reconstruction algorithms. It states that the one-dimensional Fourier transform $P(\omega, \theta)$ of a projection, acquired in the θ direction, is equivalent to a line in the two-dimensional Fourier transform $F(u, v)$ of the object function, in the same direction θ [46–48]. To derive the Fourier-slice theorem, let us first consider the example shown in Fig. 2.13. Here, we define a rotating coordinate system (r, s), such that the s-axis is parallel to the ray-path of the projection. In this rotated coordinate system, the object function $f(x, y)$ is represented by $\acute{f}(r, s)$, where r again denotes the distance between the origin and the ray. The two coordinate systems are interrelated by:

$$r = xcos\theta + ysin\theta,$$

$$s = -xsin\theta + ycos\theta. \tag{2.10}$$

We may then obtain the projection $p(r, \theta)$ from the line integral of the function $\acute{f}(r, s)$:

$$p(r, \theta) = \int_{-\infty}^{\infty} \acute{f}(r, s)\, ds, \tag{2.11}$$

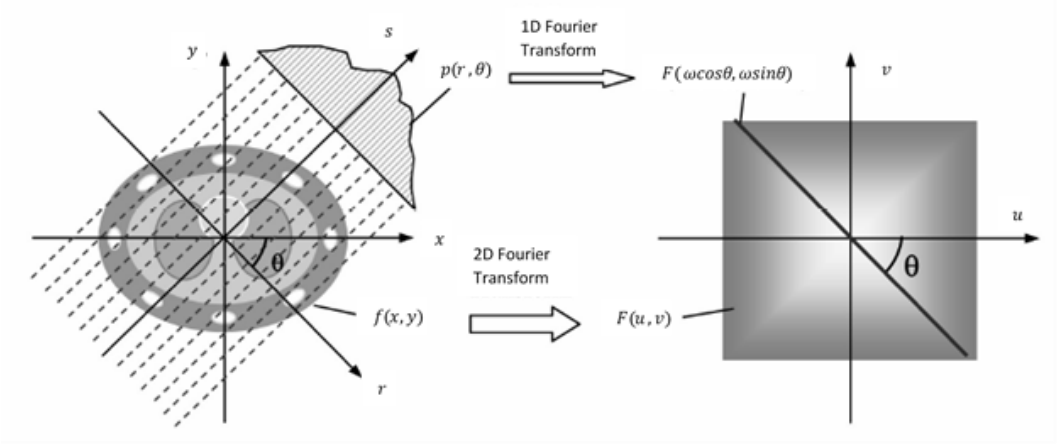

Fig. 2.13 The Fourier slice theorem [47].

The one-dimensional Fourier transform $P(\omega,\theta)$ of the projection $p(r,\theta)$ is then

$$P(\omega,\theta)=\int_{-\infty}^{\infty}\int_{-\infty}^{\infty}\acute{f}(r,s)e^{-2i\pi\omega r}\,ds\,dr,$$

(2.12)

where i is imaginary and denotes the square root of negative one. To express (2.12) in terms of the object function $f(x,y)$ we must first perform a coordinate transformation using the Jacobian. Following a coordinate transformation, areas scale by a factor equal to the Jacobian determinant J. The differential areas of $\acute{f}(r,s)$ and $f(x,y)$ are interrelated by the following expression

$$dsdr=Jdxdy=\begin{vmatrix}\frac{dr}{dx} & \frac{dr}{dy}\\ \frac{ds}{dx} & \frac{ds}{dy}\end{vmatrix}dxdy.$$

(2.13)

In this case, J is equal to unity. Combining (2.11), (2.12) and (2.13) we obtain our final expression for the one-dimensional Fourier transform $P(\omega,\theta)$ of the projection $p(r,\theta)$:

$$P(\omega,\theta)=\int_{-\infty}^{\infty}\int_{-\infty}^{\infty}f(x,y)e^{-2i\pi\omega(xcos\theta+ysin\theta)}\,dx\,dy.$$

(2.14)

To derive the Fourier slice theorem, we must obtain the two-dimensional Fourier transform $F(u,v)$ of the object function $f(x,y)$, and compare this to (2.14). The two-dimensional Fourier transform $F(u,v)$ of $f(x,y)$ is

$$F(u,v) = \int_{-\infty}^{\infty}\int_{-\infty}^{\infty} f(x,y)e^{-2i\pi(ux+vy)}\,dx\,dy.$$

(2.15)

Equations (2.14) and (2.15) are equivalent when $u = \omega cos\theta$ and $v = \omega sin\theta$. From the one-dimensional Fourier transform $P(\omega,\theta)$ of the projection we obtain a straight line $F(\omega cos\theta, \omega sin\theta)$ in the two-dimensional Fourier transform $F(u,v)$ of the object. This line passes through the origin, forming an angle θ with the u-axis, as shown in Fig. 2.13. By acquiring a large number of projections at different angles θ, we can effectively fill in the two-dimensional Fourier space of the object. The original object function $f(x,y)$ may then be recovered by performing an inverse two-dimensional Fourier transformation on our estimate of the continuous $F(u,v)$ [46,47]. The two-dimensional inverse Fourier transform of $F(u,v)$ is given by

$$f(x,y) = \int_{-\infty}^{\infty}\int_{-\infty}^{\infty} F(u,v)e^{2i\pi(ux+vy)}\,du\,dv.$$

(2.16)

2.5.7 Filtered Back-Projection

Filtered back-projection is one of the most common methods for reconstructing tomographic images [48]. In back-projection, the intensity of each projection measurement is smeared across the image plane at the angle at which it was obtained: this is equivalent to assigning to each image pixel the average value of all the projection measurements obtained at that point [46]. As projection measurements are inherently positive, this superposition amplifies attenuation within the object space, resulting in a blurred image, as shown in Fig. 2.14(f).

[This space intentionally left blank]

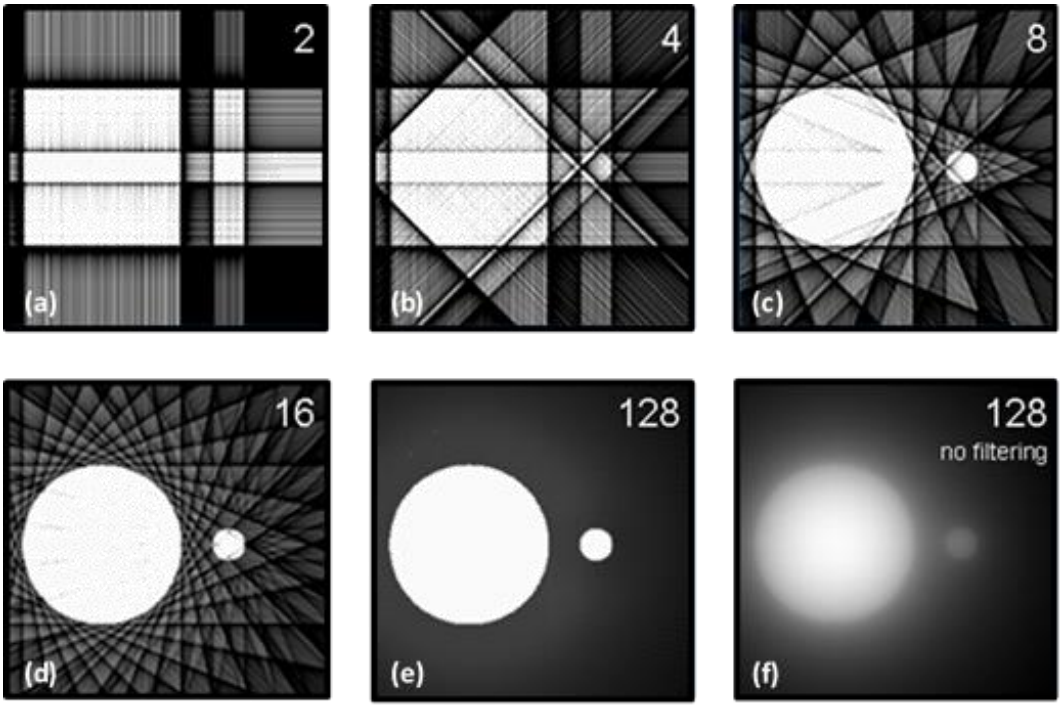

Fig. 2.14 Filtered back-projection process for an increasing number of projections. As the number of projections increases (a-e), the object begins to take shape. Comparing the filtered image (e) with the un-filtered image (f), it is clear that the negative components introduced by the applied filter drastically improves the quality of the image [50].

The back-projected image $f_b(x, y)$ is said to comprise a convolution of the true image $f(x, y)$ and some blurring function $b(x, y)$:

$$f_b(x, y) = f(x, y) * b(x, y),$$

(2.17)

where $*$ denotes the convolution operator. This relationship suggests that we may compute some deblurring function to recover the true image from the back-projected image. Rather than operating on the blurred image as a whole, it is more convenient to operate on the individual projections. The ramp filter creates negative components outside the object space to compensate for the contribution of other projections [46]:

$$\widehat{H}p(r, \theta) = \int_{-\infty}^{\infty} \left|\widehat{H}\right| P(\omega, \theta)\, e^{2i\pi\omega r} d\omega,$$

(2.18)

where $\widehat{H}$ and $\left|\widehat{H}\right|$ denote the response of the filter in the spatial and frequency domains, respectively. Following simplification due to symmetry, the back-projection of the filtered projections is obtained by

$$f(x,y) = \int_0^{\pi} \widehat{H} p(r,\theta)\, d\,\theta.$$

(2.19)

2.5.8 Convolution Back-Projection

An inherent limitation of filtered back-projection is the requirement of a uniform line integral spacing. This restricts its application to parallel projection geometries. In many second-generation and third-generation scanners, the line integrals do not form parallel lines but instead diverge from the X-ray source. The subsequent X-ray beam therefore resembles a well-collimated fan. With the increasing popularity of third-generation scanners, significant resources have been invested into the development of robust fan-beam reconstruction algorithms. One such method, convolution back-projection, shares many similarities with filtered back-projection; however, differs in that a spatial domain convolution is used instead of the frequency domain filter used in (2.18):

$$f(x,y) = \int_0^{2\pi} p(r,\theta) * \varphi(r)\, d\theta.$$

(2.20)

where $\varphi(r)$ denotes a discrete approximation to the spatial domain response of an equivalent filtered back-projection filter. Note that as the X-ray beam is now divergent, $p(r,\theta) \neq p(-r,\theta+\pi)$ and the back-projection operation is carried out over 2π. The main advantage of convolution back-projection is that it can be used in equiangular fan-beam geometries and also with some cone-beam geometries, provided the solid angle is sufficiently small [48,51]. A detailed mathematical derivation of fan-beam reconstruction methods is beyond the scope of this thesis, and is provided by Kak [51] for both equiangular and equidistant configurations.

2.5.9 Volumetric Reconstruction

So far, we have only considered the reconstruction of a two-dimensional plane from a series of line integrals. We can visualise the object in $\mathbb{R}^3$ by sequentially stacking the reconstructed planes one on top of the other. Neighbouring planes will be separated by a predefined spacing. If this interstitial spacing is greater than the slice thickness, important features may be omitted from the scan. Therefore, it is important to ensure some degree of overlap between the two quantities.

For a third-generation system with an areal detector array, it is possible to reconstruct the entire three-dimensional volume at once. When the object is defined in $\mathbb{R}^3$ its Radon transform is given by the surface integrals of the object function over a series of two-dimensional hyperplanes. The two-dimensional projections are then reconstructed into a three-dimensional volume. Volumetric reconstruction algorithms are mathematically rigorous and computationally expensive, with the detailed derivation of such methods beyond the scope of this thesis. For additional information, the interested reader is referred to the works of Smith and Kak [51,52].

2.6 References

[1] X.P. Niu, K.K. Tong, B.H. Hu, I. Pinwill, Cavity Pressure Sensor Study of the Gate Freezing Behaviour in Aluminium High Pressure Die Casting, Int. J. Cast Met. Res. 11 (1998) 105-112, https://doi.org/10.1080/13640461.1998.11819264.

[2] P.K. Mallik, Materials, Design and Manufacturing for Lightweight Vehicles, Woodhead Publishing Limited, 2010. https://doi.org/10.1533/9781845697822.

[3] X. Dong, X. Zhu, S. Ji, Effect of Super Vacuum Assisted High Pressure Die Casting on the Repeatability of Mechanical Properties of Al-Si-Mg-Mn Die-Cast Alloys, J. Mater. Process. Technol. 266 (2018) 105–113. https://doi.org/10.1016/j.jmatprotec.2018.10.030.

[4] J.P. Weiler, J.T. Wood, R.J. Klassen, E. Maire, R. Berkmortel, G. Wang, Relationship Between Internal Porosity and Fracture Strength Of Die-Cast Magnesium AM60B Alloy, Mater. Sci. Eng.: A 395 (2005) 315–322. https://doi.org/10.1016/j.msea.2004.12.042.

[5] C.H. Cáceres, B.I. Selling, Casting Defects and the Tensile Properties of an AlSiMg Alloy, Mater. Sci. Eng.: A 220 (1996) 109–116. https://doi.org/10.1016/S0921-5093(96)10433-0.

[6] H. Yang, S. Ji, D. Watson, Z. Fan, Repeatability of Tensile Properties in High Pressure Die-Castings of an Al-Mg-Si-Mn Alloy, Met. Mater. Int. 21 (2015) 936–943. https://doi.org/10.1007/s12540-015-5108-0.

[7] Y. Zhang, J.B. Patel, J. Lazaro-Nebreda, Z. Fan, Improved Defect Control and Mechanical Property Variation in High-Pressure Die Casting of A380 Alloy by High Shear Melt Conditioning, JOM. 70 (2018) 2726–2730. https://doi.org/10.1007/s11837-018-3005-y.

[8] D.R. Gunasegaram, M. Givord, R.G. O'Donnell, B.R. Finnin, Improvements Engineered in UTS and Elongation of Aluminum Alloy High Pressure Die Castings Through the Alteration of Runner Geometry and Plunger Velocity, Mater. Sci. Eng.: A 559 (2013) 276–286. https://doi.org/10.1016/j.msea.2012.08.098.

[9] E.J. Vinarcik, High Integrity Die Casting Processes, Wiley, 2002.

[10] E. Koya, M. Nakagawa, S. Kitagawa, J. Ishimoto, Y. Nakano, N. Ochiai, Research of Atomization Phenomena in HPDC-Step 1 Feature of Gas Porosity Dispersion and Photography of Atomized Flow, SAE (2018). https://doi.org/10.4271/2018-01-1392.

[11] E. Koya, M. Nakagawa, S. Kitagawa, J. Ishimoto, Y. Nakano, N. Ochiai, Atomization in High-Pressure Die Casting - Step 2 Simulation of Atomized Flow of Molten Aluminum by LES-VOF Method, SAE (2018). https://doi.org/10.4271/2018-01-1393.

[12] X.P. Niu, B.H. Hu, I. Pinwill, H. Li, Vacuum Assisted High Pressure Die Casting of Aluminium Alloys, J. Mater. Process. Technol. 105 (2000) 119–127. https://doi.org/10.1016/S0924-0136(00)00545-8.

[13] X. Li, S.M. Xiong, Z. Guo, Improved Mechanical Properties in Vacuum-Assist High-Pressure Die Casting of AZ91D Alloy, J. Mater. Process. Technol. 231 (2016) 1–7. https://doi.org/10.1016/j.jmatprotec.2015.12.005.

[14] Y. Zhou, Z. Guo, S.-M. Xiong, Effect of Runner Design on the Externally Solidified Crystals in Vacuum Die-Cast Mg-3.0Nd-0.3Zn-0.6Zr Alloy, J. Mater. Process. Technol. 267 (2019) 366–375. https://doi.org/10.1016/j.jmatprotec.2018.12.032.

[15] S. Otarawanna, C.M. Gourlay, H.I. Laukli, A.K. Dahle, Microstructure Formation in AlSi4MgMn and AlMg5Si2Mn High-Pressure Die Castings, Metall. Mater. Trans. A 40 (2009) 1645–1659. https://doi.org/10.1007/s11661-009-9841-1.

[16] C.M. Gourlay, H.I. Laukli, A.K. Dahle, Defect Band Characteristics in Mg-Al and Al-Si High-Pressure Die Castings, Metall. Mater. Trans. A 38 (2007) 1833–1844. https://doi.org/10.1007/s11661-007-9243-1.

[17] R. Helenius, O. Lohne, L. Arnberg, H.I. Laukli, The Heat Transfer During Filling of a High-Pressure Die-Casting Shot Sleeve, Mater. Sci. Eng.: A 413–414 (2005) 52–55. https://doi.org/10.1016/j.msea.2005.08.166.

[18] S. Otarawanna, H.I. Laukli, C.M. Gourlay, A.K. Dahle, Feeding Mechanisms in High-Pressure Die Castings, Metall. Mater. Trans. A 41 (2010) 1836–1846. https://doi.org/10.1007/s11661-010-0222-6.

[19] X. Li, S.M. Xiong, Z. Guo, On the Porosity Induced by Externally Solidified Crystals in High-Pressure Die-Cast of AM60B Alloy and its Effect on Crack Initiation and Propagation, Mater. Sci. Eng.: A 633 (2015) 35–41. https://doi.org/10.1016/j.msea.2015.02.078.

[20] J. Campbell, Castings, 2nd ed., Butterworth-Heinemann, Oxford, 2003.

[21] J.C. Fisher, Fracture of Liquids: Nucleation Theory Applied to Bubble Formation, Sci. Mon. 68 (1949) 415–419.

[22] J. Campbell, Origin of porosity in cast metals, PhD thesis, University of Birmingham, 1967.

[23] J.B. Patel, J. Lazaro-Nebreda, Z. Fan, Development of the Multi-Purpose High Shear Mixing Technology for Continuous Processing of Al and Mg Alloys, Proc. of 6th Decenn. Int. Conf. on Solidification Process., Old Windsor, 2017.

[24] J. Davis, ASM Specialty Handbook: Aluminum and Aluminum Alloys - ASM International, 1993. https://www.asminternational.org/search/-/journal_content/56/10192/06610G/PUBLICATION (accessed September 8, 2020).

[25] E. Lordan, J. Lazaro-Nebreda, Y. Zhang, Z. Fan, Effective Degassing for Reduced Variability in High-Pressure Die Casting Performance, JOM. 71 (2019) 824–830. https://doi.org/10.1007/s11837-018-3186-4.

[26] L. Wang, P. Turnley, G. Savage, Gas Content in High Pressure Die Castings, J. Mater. Process. Technol. 211 (2011) 1510–1515. https://doi.org/10.1016/j.jmatprotec.2011.03.024.

[27] S. Bhagavath, B. Cai, R. Atwood, M. Li, B. Ghaffari, P.D. Lee, S. Karagadde, Combined Deformation and Solidification-Driven Porosity Formation in Aluminum Alloys, Metall. Mater. Trans. A 50 (2019) 4891–4899. https://doi.org/10.1007/s11661-019-05378-8.

[28] G. Couturier, J.L. Desbiolles, M. Rappaz, A Porosity Model for Multi-Gas Systems in Multi-Component Alloys, MCWASP, Nice, 2006.

[29] Ch. Pequet, M. Rappaz, M. Gremaud, Modeling of Microporosity, Macroporosity, and Pipe-Shrinkage Formation During the Solidification of Alloys Using a Mushy-Zone Refinement Method: Applications to Aluminum Alloys, Metall. Mater. Trans. A. 33 (2002) 2095–2106. https://doi.org/10.1007/s11661-002-0041-5.

[30] C.M. Gourlay, A.K. Dahle, Dilatant Shear Bands in Solidifying Metals, Nat. Comms. 445 (2007) 70–73. https://doi.org/10.1038/nature05426.

[31] A.K. Dahle, L. Arnberg, Development of Strength in Solidifying Aluminium Alloys, Acta Mater. 45 (1997) 547–559. https://doi.org/10.1016/S1359-6454(96)00203-0.

[32] L. Yuan, C. O'Sullivan, C.M. Gourlay, Exploring Dendrite Coherency with the Discrete Element Method, Acta Mater. 60 (2012) 1334–1345. https://doi.org/10.1016/j.actamat.2011.11.042.

[33] A.K. Dahle, D.H. StJohn, Rheological Behaviour of the Mushy Zone and its Effect on the Formation of Casting Defects During Solidification, Acta Mater. 47 (1998) 31–41. https://doi.org/10.1016/S1359-6454(98)00342-5.

[34] C.M. Gourlay, B. Meylan, A.K. Dahle, Shear Mechanisms at 0–50% Solid During Equiaxed Dendritic Solidification of an AZ91 Magnesium Alloy, Acta Mater. 56 (2008) 3403–3413. https://doi.org/10.1016/j.actamat.2008.03.020.

[35] T. Sumitomo, D.H. StJohn, T. Steinberg, The Shear Behaviour of Partially Solidified Al–Si–Cu Alloys, Mater. Sci. Eng.: A 289 (2000) 18–29. https://doi.org/10.1016/S0921-5093(00)00936-9.

[36] A.M. Waters, Three-Dimensional Analysis of Voids in AM60B Magnesium Tensile Bars Using Computed Tomography Imagery, PhD thesis, Lawrence Livermore National Lab., 2001.

[37] D.M. Walker, K. Vo, A. Tordesillas, On Reynolds' Dilatancy and Shear Band Evolution: A New Perspective, Int. J. Bifurc. Chaos. 23 (2013) 1330034. https://doi.org/10.1142/S0218127413300346.

[38] C.M. Gourlay, C. O'Sullivan, J. Fonseca, L. Yuan, K.M. Kareh, T. Nagira, H. Yasuda, Synchrotron Radiography Studies of Shear-Induced Dilation in Semisolid Al Alloys and Steels, JOM. 66 (2014) 1415–1424. https://doi.org/10.1007/s11837-014-1029-5.

[39] A. Tordesillas, Force Chain Buckling, Unjamming Transitions and Shear Banding in Dense Granular Assemblies, Philos. Mag. 87 (2007) 4987–5016. https://doi.org/10.1080/14786430701594848.

[40] F. Radjai, D.E. Wolf, M. Jean, J.-J. Moreau, Bimodal Character of Stress Transmission in Granular Packings, Phys. Rev. Lett. 80 (1998) 61–64. https://doi.org/10.1103/PhysRevLett.80.61.

[41] A. Tordesillas, J. Shi, T. Tshaikiwsky, Stress–Dilatancy and Force Chain Evolution, Int. J. Numer. Anal. Methods Geomech. 35 (2011) 264–292.

[42] J. Konishi, M. Oda, S. Nemat-nasser, Induced Anisotropy in Assemblies of Oval Cross-Sectional Rods in Biaxial Compression, Stud. Appl. Mech. 7 (1983) 31–39. https://doi.org/10.1016/B978-0-444-42192-0.50010-4.

[43] K. Iwashita, M. Oda, Micro-Deformation Mechanism of Shear Banding Process Based on Modified Distinct Element Method, Powder Technol. 109 (2000) 192–205. https://doi.org/10.1016/S0032-5910(99)00236-3.

[44] T.S. Majmudar, R.P. Behringer, Contact Force Measurements and Stress-Induced Anisotropy in Granular Materials, Nat. Comms. 435 (2005) 1079–1082. https://doi.org/10.1038/nature03805.

[45] Confirming the Link Between Disorder and Metastability in Granular Physics, https://phys.org/news/2016-05-link-disorder-metastability-granular-physics.html (accessed September 8, 2020).

[46] J. Baruchel, J.Y. Buffière, E. Maire, P. Merle, G. Peix, X-ray Tomography in Material Science, Hermes Science Publications, 2000.

[47] J. Hsieh, Computed Tomography: Principles, Design, Artifacts and Recent Advances. 2nd ed., SPIE Press, 2009.

[48] A.M. Waters, Three-Dimensional Analysis of Voids in AM60B Magnesium Tensile Bars Using Computed Tomography Imagery, PhD, Lawrence Livermore National Lab., CA (US), 2001.

[49] S.R. Deans, The Radon Transform and Some of Its Applications, Wiley, 1983.

[50] http://www.impactscan.org/slides/impactcourse/basic_principles_of_ct/img15.html (accessed September 9, 2020).

[51] A.C. Kak, Computerized Tomography with X-Ray, Emission, and Ultrasound Sources, in: Proceedings of the IEEE (1979) 1245–1272. https://doi.org/10.1109/PROC.1979.11440.

[52] B.D. Smith, Cone-Beam Tomography: Recent Advances and a Tutorial Review, Opt. Eng. 29 (1990) 524. https://doi.org/10.1117/12.55621.

Chapter 3: Experimental Method

3.1 Material Preparation and HPDC Operating Conditions

Unless stated otherwise, a typical AlSiMnMg die-casting alloy (8 % Si, 0.4 % Mn, 0.3 % Mg) is used as a base material. This is a variant of the renowned A356 alloy, which has been modified for HPDC; the addition of Mn helps to prevent die soldering, and facilitates the conversion of harmful β-Fe intermetallic phases to less harmful α-Fe intermetallic phases [1]. The melts were prepared in clay-graphite crucibles (45 kg charge) and melted in an electric resistance furnace at 750 °C. The melt was degassed using a conventional rotary degassing unit (4 L/min of argon at 350 rpm for 10 min) and then manually ladled into the shot chamber of a Frech 4500 kN locking force cold chamber HPDC machine. The temperature of the melt, shot chamber and die cavity were maintained at 680°C, 180°C and 200°C respectively. See Chapter 6 for further information regarding the processing parameters and operating conditions of the HPDC machine.

3.2 X-ray Tomography and Three-Dimensional Analysis

3.2.1 Data Acquisition

Two CT scanners were used for X-ray inspection: the YCT Compact XL Mag (YXLON International) macrotomography system, and the Xradia 410 Versa (Carl Zeiss AG) microtomography system. The YCT Compact XL Mag was selected for matters concerning the macroscopic; the Xradia 410 Versa for those concerning the microscopic.

The YCT Compact XL Mag adopts a third-generation configuration, with a linear detector array and a fan-beam geometry with its apex located at the X-ray source. This system is particularly suited for the inspection of medium to large-sized components: boasting a large field of view and an achievable resolution of about 100 µm. Data acquisition and tomographic reconstructions are performed in parallel, with an anisotropic voxel defined by a pixel size and an interstitial spacing. Based on preliminary trials, an operating voltage of 450 kV and a current of 1 mA was selected for this work. YXLON's dedicated software algorithms were then used to generate raw sinograms and the reconstructed tomograms; with options available for noise reduction and the removal of artefacts.

The Xradia 410 Versa utilises a third-generation configuration, with an areal detector array and a cone-beam geometry with its apex located at the X-ray source. The user defines an isotropic voxel in the Scout-and-Scan Control System (Carl Zeiss AG), with an achievable resolution of about 0.9 µm. In this work, a resolution of approximately 3.5 µm was deemed sufficient for the analysis of porosity and inclusions. An appropriate operating voltage (80 kV or 140 kV), exposure time, and filter was selected depending on the sample material and geometry. Following data acquisition, volumetric

reconstructions were performed within the XMReconstructor software (Carl Zeiss AG) allowing for phase-shift and beam-hardening corrections.

3.2.2 Analysis of Porosity and Inclusions

The VGSTUDIO MAX software suite (Volume Graphics GmbH) was used to visualise and analyse the three-dimensional volumes; to import data from the Xradia 410 Versa into VGSTUDIO MAX, it was first necessary to convert the three-dimensional volume into a sequence of tomograms (*.TIFF format images) in the XMReconstructor software. After importing the tomograms into VGSTUDIO MAX, an iterative local surface determination was performed to define outer boundaries of the material volume while compensating for local fluctuations in grey value. Defect descriptors (relating to size, shape and location) were obtained using the VGDEFX void and inclusion analysis module in VGSTUDIO MAX. A probability threshold of 0.8 was defined to distinguish defects from the Al-matrix; this probability is determined by the contrast between the candidate defect and the background material. Only defects larger than 8 voxels in volume, with a probability exceeding the prescribed threshold, were considered in later analyses. As we are usually concerned with the largest defects in a material (typically 500~1000 µm in diameter) the spatial resolution of the system (3.5 µm) is assumed to have a marginal effect on defect size.

3.3 Microstructural Characterization

3.3.1 Optical Microscopy and Scanning Electron Microscopy

Samples for microstructural characterisation were taken from the centre of the gage length, perpendicular to the tensile direction. Samples were ground using standard metallurgical techniques, and then polished to a 0.04 µm finish using an OPUS non-crystallising colloidal silica suspension (Metprep Ltd.). To reveal the microstructure, samples were etched with Keller's reagent (95% H_2O, 2.5% HNO_3, 1.5% HCl, and 1% HF). The etched microstructures were then observed via optical microscopy and/or scanning electron microscopy. Electron microscopy was performed on a LEO 1455VP (Carl Zeiss AG) scanning electron microscope (SEM) equipped with an Apollo XP silicon drift detector (EDAX Inc.) for energy dispersive X-ray spectroscopy (EDX).

3.3.2 Electron Backscatter Diffraction

Electron backscatter diffraction (EBSD) was used to quantitatively assess grain size distributions in the as-cast microstructures. Here, EBSD is preferred to more conventional optical techniques as the latter techniques have been shown to produce unreliable grain size measurements for HPDC microstructures [2]. Samples for EBSD were ground using standard metallurgical techniques, and then polished to a 0.04 µm finish using an OPUS non-crystallising colloidal silica suspension (Metprep

Ltd.). The samples then underwent vibratory polishing, using the aforementioned colloidal silica suspension, a frequency of 90 Hz, and a polishing time of roughly 40 min. EBSD was carried out on a Crossbeam 350 FIB-SEM (Carl Zeiss AG) equipped with an Hikari Plus EBSD camera (EDAX Inc.). EBSD data was acquired at 20 kV with a sample tilt of 70 °. Mapping was performed using the EBSD Analysis module within the TEAM software package (EDAX Inc.), for which a 152 x 120 µm region was analysed with a step size of 0.4 µm. After mapping, EBSD data was analysed in the OIM Analysis software (EDAX Inc.). Grains in OIM are defined as groups of connected and similarly oriented points. For each point, an algorithm checks to see if its neighbours are within a grain tolerance angle defined by the user. If a neighbouring point is within the grain tolerance angle, then it is added to the grain, and its neighbours are checked to see if they are within the grain tolerance angle for the new point. This process is repeated until the grain is bounded by points that exceed the grain tolerance angle to their neighbours. For this work a grain tolerance angle of 5 ˚ was selected, corresponding to the misorientation of a low-angle grain boundary. A minimum grain size of 2 μm was used, in concord with the chosen step size.

3.4 Tensile Testing

Tensile tests were performed at room temperature using an Instron 5500 universal electromechanical testing system equipped with a 50 kN load cell, in accordance with ASTM standard E8/E8M [3]. Of these post-mortem tensile specimens, a select few were isolated and the fracture surfaces examined on a LEO 1455VP (Carl Zeiss AG) SEM equipped with an Apollo XP silicon drift detector (EDAX Inc.) for EDX.

3.5 References

[1] S. Ji, W. Yang, F. Gao, D. Watson, Z. Fan, Effect of Iron on the Microstructure and Mechanical Property of Al–Mg–Si–Mn And Al–Mg–Si Diecast Alloys, Mater. Sci. Eng.: A 564 (2013) 130–139. https://doi.org/10.1016/j.msea.2012.11.095.

[2] A. Bowles, K. Nogita, M. Dargusch, C. Davidson, J. Griffiths, Grain Size Measurements in Mg-Al High Pressure Die Castings Using Electron Back-Scattered Diffraction (EBSD), Mater. Trans. 45 (2004) 3114–3119. https://doi.org/10.2320/matertrans.45.3114.

[3] E28 Committee, Test Methods for Tension Testing of Metallic Materials, ASTM International, https://doi.org/10.1520/E0008_E0008M-16AE01.

Chapter 4: Statistical Modelling of Extreme Values

4.1 Introduction

The Engineer concerns themself with the unusual rather than the usual. We often deliberate the maximum load incurred on a structure; the largest defect within a material volume; the lowest ductility or fatigue life. Accordingly, when analysing defects or mechanical properties, we should consider the tails of the probability distribution as opposed to the mean, or expected value—as these extremes dictate our decision-making.

Extreme value theory allows one to make inference on the likelihood and magnitude of extreme events, based on limited data. The derivation of this theorem is analogous to the convergence of the sample mean to the population mean in the central limit theorem [1]. Methods based on the statistics of extremes are often used in modern durability (fatigue) analysis, where correlations have been established between the defect size distribution and the fatigue life [2]. In contrast, such techniques have rarely been used to relate the probability distribution of defect size to the scatter in tensile ductility [3]. Here, we introduce two classes of continuous probability distributions developed within extreme value theory: the generalized extreme value (GEV) distribution and the generalized Pareto (GP) distribution.

4.2 Block Maxima

4.2.1 The Generalized Extreme Value Distribution

The two classes of probability distributions discussed in this chapter—the GEV and GP distributions—differ in their approach to characterising extremes. Let us first consider the behaviour of the maximum order statistic [1]:

$$M_n = max\{X_1, \dots X_n\},$$

with $X_1, \dots X_n$ denoting a sequence of independent and identically distributed (IID) random variables sharing some marginal distribution function. The distribution of M_n is degenerate. Analogous to the central limit theorem, we can avoid this difficulty through a linear rescaling of M_n:

$$M_n^* = \frac{M_n - b_n}{a_n}.$$

If there exists some sequence of constants $\{a_n > 0\}$ and $\{b_n\}$, such that

$$\Pr\{M_n^* \leq z\} \to G(z) \quad as\ n \to \infty,$$

then $G(z)$ is a non-degenerate distribution function described by one of the Gumbel (I), Fréchet (II) or Weibull (III) families:

$$\text{I: } G(z) = \exp\left\{-\exp\left[-\left(\frac{z-b}{a}\right)\right]\right\}, \quad -\infty < z < \infty;$$

$$\text{II: } G(z) = \begin{cases} 0, & z \le b, \\ \exp\left\{-\left(\frac{z-b}{a}\right)^{-c}\right\}, & z > b\,; \end{cases}$$

$$\text{III: } G(z) = \begin{cases} \exp\left\{-\left[-\left(\frac{z-b}{a}\right)^{c}\right]\right\}, & z < b. \\ 1, & z \ge b, \end{cases}$$

Each family is parameterized by a scale parameter $a > 0$ and a location parameter b; the Fréchet and Weibull distributions also possess a shape parameter $c > 0$.

The GEV distribution combines the Gumbel, Fréchet, and Weibull families into a single functional form; the data decides which of the three distributions is most appropriate. The GEV distribution is parameterized by a location parameter μ, a scale parameter σ and a shape parameter ξ, which controls the tail behaviour of the distribution. The cumulative distribution function (CDF) of the GEV distribution is

$$G(z) = \exp\left\{-\left[1+\xi\left(\frac{z-\mu}{\sigma}\right)\right]^{-1/\xi}\right\}, 1+\xi\left(\frac{z-\mu}{\sigma}\right) > 0.$$

(4.1)

For $\xi \to 0$, the GEV distribution is equivalent to the Gumbel distribution, which is characterised by an exponentially decreasing tail:

$$G(z) = \exp\left[-\exp\left(-\frac{z-\mu}{\sigma}\right)\right].$$

(4.2)

For $\xi > 0$, the GEV distribution is equivalent to the Fréchet distribution, which possesses a polynomially decreasing tail and a finite lower bound μ':

$$G(z) = \begin{cases} 0, & z < \mu' \\ \exp\left[-\left(\frac{z-\mu'}{\sigma'}\right)^{-1/\xi}\right], & z \ge \mu'. \end{cases}$$

(4.3)

Here we introduce two new parameters, μ' and σ', for $\xi \neq 0$

$$\mu' = \mu - \frac{\sigma}{\xi} > 0, \qquad \sigma' = \left|\frac{\sigma}{\xi}\right| > 0.$$

(4.4)

$\xi < 0$ is equivalent to the Weibull distribution, which possesses a finite upper bound μ':

$$G(z) = \begin{cases} \exp\left[-\left(-\frac{z-\mu'}{\sigma'}\right)^{-1/\xi}\right], & z < \mu' \\ 0, & z \geq \mu'. \end{cases}$$

(4.5)

4.2.2 Estimates of Return Levels

Although the parameter estimates $\{\xi, \sigma, \mu\}$ provide valuable insight into the quality-of-fit and tail behaviour of the distribution, we are often more interested in estimates of the extreme quantiles. The quantile function is obtained by inverting (4.1) for $G(z_p) = 1 - p$:

$$z_p = \mu - \frac{\sigma}{\xi}\left[1 - \{-\log(1-p)\}^{-\xi}\right], \quad for\ \xi \neq 0,$$

$$z_p = \mu - \sigma \log\{-\log(1-p)\}, \quad for\ \xi = 0.$$

(4.6)

Where z_p is commonly termed the return level. The return level z_p is defined as the value that is expected to be equalled, or exceeded, on average once every return period m with probability $p = 1/m$. It thus represents a lower bound to the maximum value of z expected in a group of m measurements, i.e. $\max\{z_1, \ldots, z_m\}$.

4.3 Threshold Models

4.3.1 The Generalized Pareto Distribution

As a sampling technique, block maxima can be wasteful if other data on extremes are also available: if the maximum order statistic is supposed to be extreme, why would an observation of similar magnitude not also be considered extreme? Furthermore, the choice of block size can be crucial: too small and you introduce bias in estimation and extrapolation; too large and you are left with few data points, and large estimation variance [1].

An alternative approach to characterising extremes is to regard as extreme events those observations $X_1, \ldots X_n$ that exceed some threshold u, where the X_i are again IID random variables with some marginal distribution function. For sufficiently large u, the distribution function of $(y = X_i - u \mid X_i > u)$, is approximately

$$H(y) = 1 - \left(1 + \frac{\xi y}{\tilde{\sigma}}\right)^{-1/\xi},$$

(4.7)

for $y > 0$ and $(1 + \xi y/\tilde{\sigma}) > 0$. Here, we introduce a new parameter $\tilde{\sigma}$

$$\tilde{\sigma} = \sigma + \xi(u - \mu),$$

(4.8)

where (μ, σ, ξ) denote the location, scale, and shape parameters of the associated GEV distribution [1]. The family of distributions defined by (4.7) constitute the GP distribution. As with the GEV distribution, the shape parameter ξ controls the tail behaviour of the GP distribution: $\xi < 0$ corresponds to an underlying distribution with a finite upper bound $u - \tilde{\sigma}/\xi$; $\xi > 0$ corresponds to an underlying distribution characterised by a polynomially decreasing tail and no upper limit; $\xi \to 0$ corresponds to an exponential distribution with rate $1/\tilde{\sigma}$:

$$H(y) = 1 - \exp\left(-\frac{y}{\tilde{\sigma}}\right), \quad y > 0.$$

(4.9)

4.3.2 Threshold Selection

To address the threshold selection problem, we adopt an exploratory technique based on the threshold stability property of the GP distribution: if the GP distribution is valid for some threshold u_0, then it is also valid for all thresholds $u > u_0$ [1]. If σ_{u_0} denotes the scale parameter associated with the threshold u_0, then the expected value of the GP distribution is

$$E(X - u \mid X > u) = \frac{\sigma_{u_0} + \xi u}{1 - \xi}.$$

(4.10)

$E(X - u \mid X > u)$ thus becomes a linear function of u when $u > u_0$. Furthermore, an empirical estimate of $E(X - u \mid X > u)$ is obtained from the sample mean of threshold exceedances.

Accordingly, the mean residual life plot comprises the set of points

$$\left\{\left(u, \quad \frac{1}{n_u}\sum_{i=1}^{n_u}(X_i - u)\right) : u < X_{max}\right\},$$

where $x_1, \ldots, x_{n_u}$ comprise the n_u observations greater than u, and X_{max} denotes the largest of the X_i [1]. A suitable threshold may then be selected by searching for the onset of linearity in the mean residual life plot.

4.3.3 Estimates of Return Levels

Now, suppose that the GP distribution provides a reasonable approximation to the limiting distribution of threshold exceedances, then

$$\Pr(X > x \mid X > u) \approx \left[1 + \xi\left(\frac{x - u}{\tilde{\sigma}}\right)\right]^{-1/\xi}.$$

(4.11)

Considering the left-hand side of (4.11), we can express $\Pr(X > x \mid X > u)$ as a quotient

$$\Pr(X > x \mid X > u) = \frac{\Pr(X > x)}{\Pr(X > u)}.$$

(4.12)

Substituting (4.11) into (4.12) we obtain

$$\Pr(X > x) = \zeta_u \left[1 + \xi \left(\frac{x - u}{\tilde{\sigma}}\right)\right]^{-1/\xi},$$

(4.13)

where $\zeta_u = \Pr(X > u)$ [1]. The m^{th}-observation return level is then obtained by inverting (4.13) for $\Pr(X > x_m) = 1/m$:

$$x_m = u + \frac{\tilde{\sigma}}{\xi}\left[(m\zeta_u)^{\xi} - 1\right], \quad for\ \xi \neq 0;$$

$$x_m = u + \tilde{\sigma}\log(m\zeta_u), \quad for\ \xi \to 0.$$

(4.14)

In practise, one might prefer to express the return level on a temporal or volumetric scale. For example, suppose we wish to express return levels on an annual scale. This is achieved by substitution of $m = nN_y$ into (4.14):

$$x_n = u + \frac{\tilde{\sigma}}{\xi}\left[\left(nN_y\zeta_u\right)^{\xi} - 1\right], \quad for\ \xi \neq 0;$$

$$x_n = u + \tilde{\sigma}\log\left(nN_y\zeta_u\right), \quad for\ \xi \to 0,$$

(4.15)

Where, by definition, N_y is the number of observations per year and x_n is the n-year return level.

4.4 References

[1] S. Coles, An Introduction to Statistical Modelling of Extreme Values, Springer-Verlag, London, 2001.

[2] M. Tiryakioğlu, Relationship Between Defect Size and Fatigue Life Distributions in Al-7 Pct Si-Mg Alloy Castings, Metall. Mater. Trans. A 40 (2009) 1623–1630. https://doi.org/10.1007/s11661-009-9847-8.

[3] X. Teng, H. Mae, Y. Bai, T. Wierzbicki, Pore Size and Fracture Ductility of Aluminum Low Pressure Die Casting, Eng. Fract. Mech. 76 (2009) 983–996. https://doi.org/10.1016/j.engfracmech.2009.01.001.

Chapter 5: Establishing a Baseline HPDC Process

5.1 Introduction

Before addressing the problem of casting consistency, we must first define a set of processing parameters and operating conditions that are representative of industrial HPDC. This chapter does not review the state of the art, but rather aims to reproduce the variability encountered in commercial die-casting foundries. The representativity of this *Baseline* process is assessed in Section 6.4.5.

5.2 Baseline HPDC Process

5.2.1 Casting Procedure

A 45 Kg charge of Al8SiMnMg alloy is melted in an electric resistance furnace and then held at 750 °C for 30 min to maintain a uniform composition distribution. The melt is then degassed using a conventional rotary degassing unit for 10 min with a stirring speed of 350 rpm and an argon flow rate of 4 L/min; although other, more effective, techniques are available (e.g. melt conditioning [1] and ultrasonic melt processing [2]) rotary degassing was chosen as it is most representative of commercial foundry practise. After degassing, the liquid is manually ladled into the shot chamber of a Frech 4500 kN locking force cold chamber HPDC machine to produce ASTM standard [3] tensile specimens. The die geometry used in this work is shown in Fig. 5.1. The pouring temperature is maintained at 680±5 °C using a thermocouple; the temperature of the die and shot chamber are kept at ~200 °C and ~180 °C, respectively.

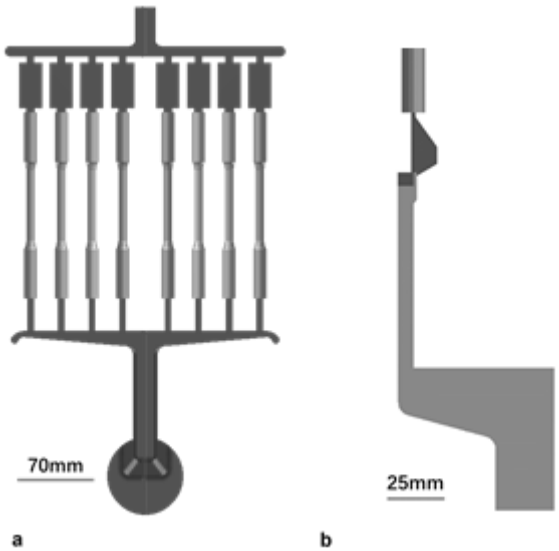

Fig. 5.1 Die geometry used to produce ASTM standard tensile specimens [3]. (a) Front view. (b) Side view of runner-orifice system. The gauge length and gauge diameter of the tensile specimens are 50 mm and 6.35 mm, respectively.

5.2.2 Thermal Die Cycling

The temperature of the die influences the quality of the cast component: low die temperatures are detrimental to liquid feeding during solidification, which may lead to porosity; high die temperatures increase the likelihood of flashing and soldering, both of which reduce productivity. We assume that the die surface is initially at room temperature (25 °C). Once activated, heating channels in the mobile and stationary platens heat the die to working condition. A target temperature of 200 °C is set in accordance with industrial practise; the heating channels automatically deactivate once this target is achieved. However, using the heating channels alone is highly inefficient. To assist in the heating process, it is common to perform a series of complimentary 'warm-up' shots to heat the die using the liquid metal. This raises a natural question: what is the optimal number of cycles required to heat the die to working condition?

Table 5.1 Thermal die cycling: sequence and durations used in the model

Sleeve pre-filling duration	3 s	Spraying start time	30 s
Piston starts to move	At 3.01 s	Spraying end time	48 s
Die opening	At 10 s	Blowing start time	49 s
Part ejection time	20 s	Blowing end time	55 s

[This space intentionally left blank]

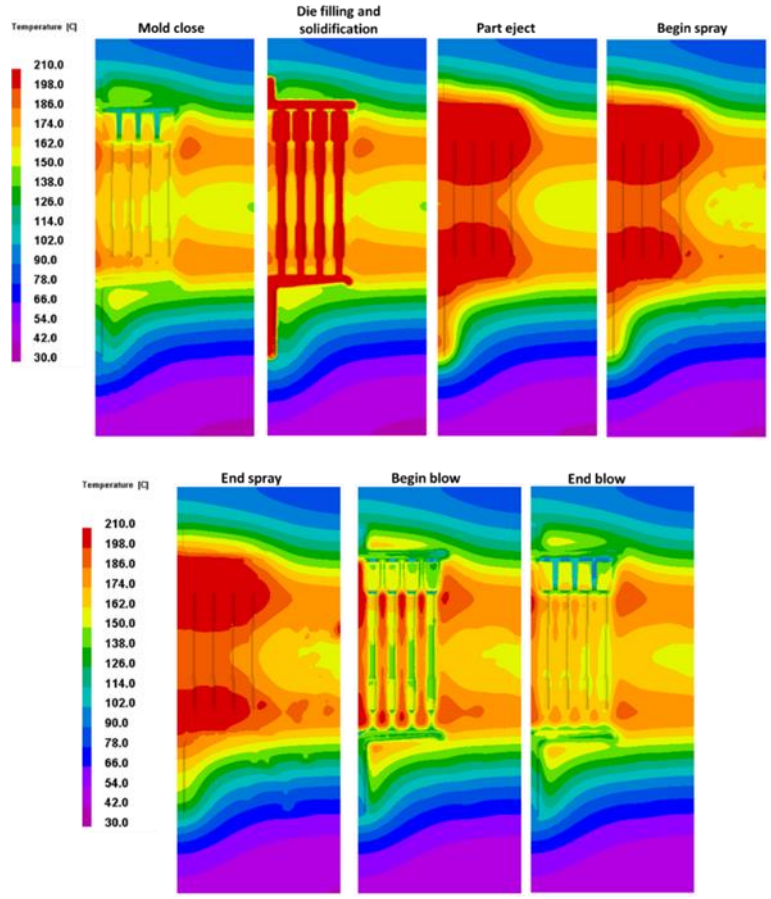

Fig. 5.2 Temperature distribution over the surface of the die during the sixth HPDC cycle. Courtesy of Dr. Kun Dou.

To answer this question, simulations were performed in ProCAST (ESI Group) and validated experimentally. A detailed description of the modelling procedure is outlined in reference [4]. In short, governing equations for mass, momentum, and heat (based on the enthalpy method) are solved in ProCAST [4]. The volume of fluid (VOF) method is used to monitor the evolution of the melt free surface [4]. Fluid turbulence is described using a standard k-ε turbulence model described in references [5–7]. Simulations were performed on finite element meshes generated from geometrical models of the HPDC machine produced in AutoCAD (Autodesk Inc.).

For a given cycle, we can divide the thermal history of the die into five periods: liquid metal injection and solidification; die opening and part ejection; die spraying (coolant); die blowing (air); and die closing. Experiments were performed to obtain representative durations for each period (Table 5.1); videos of the die spraying process were recorded to obtain representative spray trajectories for the model. Based on these experiments, a dynamic interfacial heat transfer coefficient was defined. The initial condition of a given cycle is equivalent to the final temperature of the previous cycle. By iterating this procedure, the thermal history of the die was modelled over a period of twenty cycles.

Fig. 5.2 shows the evolution of die surface temperature during the sixth HPDC cycle. The temperature distribution is both non-uniform and time-variant. To validate the model, a FLIR T6XX series infrared camera was used to capture thermographic images of the die surface; thermographic data was analysed in the FLIR Tools software package. Thermocouple measurements of the die surface temperature confirmed the accuracy of the infrared camera. Fig. 5.3 compares the simulated and experimental temperature distributions, for which there is a strong agreement.

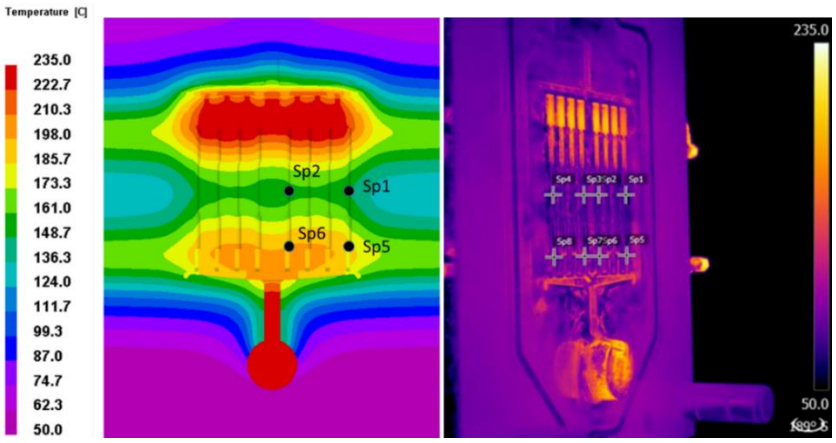

Fig. 5.3 Comparison of simulated (left) and experimental (right) temperature distributions over the die surface. SP# refer to spot measurement points extracted from the numerical model/thermographic image. Simulation courtesy of Dr. Kun Dou.

Fig. 5.4 presents temperature curves calculated over twenty cycles (each curve corresponds to one of the four spot measurement points *SP#* shown in Fig. 5.3). A quasi-steady die temperature is achieved after sixteen cycles (roughly 900 ms). Due to practical limitations (specifically, the maximum crucible volume) the first seven castings of each experiment were scrapped with subsequent castings used for microstructural analysis and mechanical testing. Similarly, simulations of the HPDC process use the final die temperature after the seventh cycle as an initial condition.

[This space intentionally left blank]

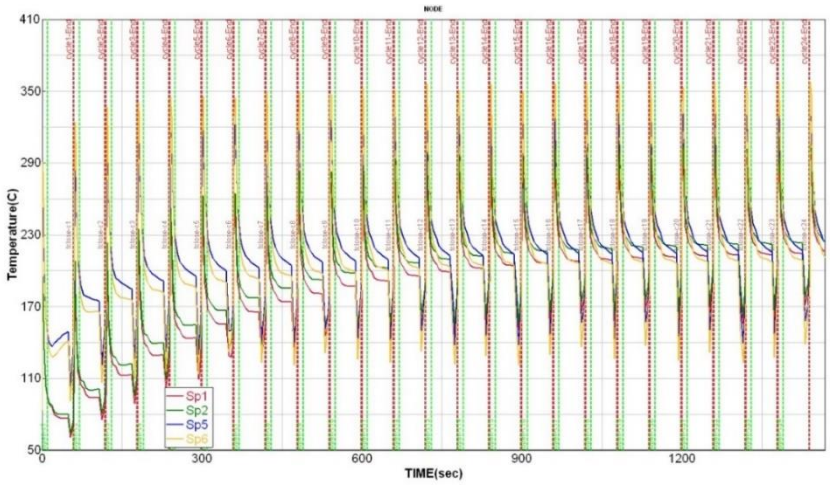

Fig. 5.4 Calculated temperature curves for sampling positions SP# (see Fig. 5.3) on the die surface recorded over 20 thermal cycles. Simulation courtesy of Dr. Kun Dou.

5.2.3 Process Parameters

Aside from melt quality and the operating conditions in the HPDC cell, the kinematic parameters of the injection system (i.e. the plunger speed profile and the pressure exerted by the hydraulic actuator) also influence the quality of the cast component. We can divide the kinematics of the plunger into three distinct stages: the slow-shot stage; the fast-shot stage (i.e. injection); and the intensification stage. In the slow-shot stage, the plunger moves at low speeds to produce a wave of molten metal that just reaches the ceiling of the shot chamber, expelling air ahead of the liquid front. In the fast-shot stage, the melt is injected at high speeds through a narrow orifice system to fill the cavity. Once the cavity is full, an intensification pressure of 30∼100 MPa [5] is applied to the solidifying alloy to compress gaseous phases and to assist in the feeding of shrinkage strains. The purpose of this chapter is not to discuss the current state of the art, but rather to establish a set of processing parameters and operating conditions that are representative of commercial foundry practice. Therefore, a plunger speed profile was selected according to recommendations from the supplier of the HPDC machine (Fig. 5.5). The control system switches from displacement control to pressure control once the piston traverses 375 mm, and a minimum pressure of 3 MPa has been attained. An intensification pressure of 32 MPa was selected, corresponding to the maximum attainable pressure of the hydraulic actuator.

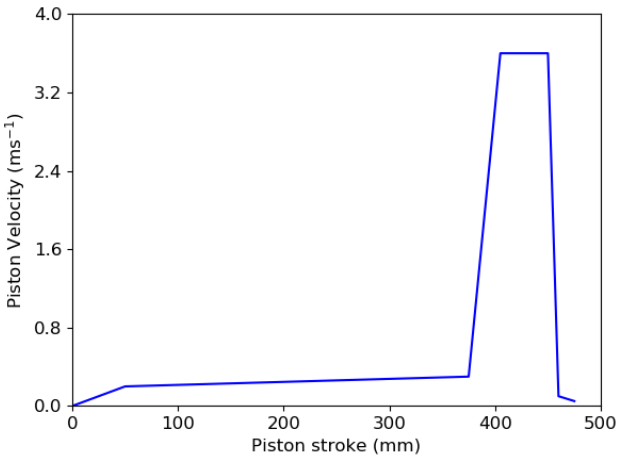

Fig. 5.5 Baseline plunger speed profile.

5.3 References

[1] E. Lordan, J. Lazaro-Nebreda, Y. Zhang, Z. Fan, Effective Degassing for Reduced Variability in High-Pressure Die Casting Performance, JOM. 71 (2019) 824–830. https://doi.org/10.1007/s11837-018-3186-4.

[2] D.G. Eskin, I. Tzanakis, F. Wang, G.S.B. Lebon, T. Subroto, K. Pericleous, J. Mi, Fundamental Studies of Ultrasonic Melt Processing, Ultrason. Sonochem. 52 (2019) 455–467. https://doi.org/10.1016/j.ultsonch.2018.12.028.

[3] ASTM Committee, Standard Test Methods for Tension Testing of Metallic Materials, 2003.

[4] K. Dou, E. Lordan, Y.J. Zhang, A. Jacot, Z.Y. Fan, Numerical Simulation of Fluid Flow, Solidification and Defects in High Pressure Die Casting (HPDC) Process, IOP Conf. Ser.: Mater. Sci. Eng. 529 (2019) 012058. https://doi.org/10.1088/1757-899X/529/1/012058.

[5] S. Elghobashi, T. Abou‐Arab, A Two‐Equation Turbulence Model for Two‐Phase Flows, Phys. Fluids. 26 (1983) 931–938.

[6] A. Vakhrushev, A. Ludwig, Menghuai Wu, Y. Tnag, G. Nitzl, G. Hackl, Modeling of Turbulent Melt Flow and Solidification Processes in Steel Continuous Caster with the Open Source Software Package OpenFOAM, (2010).

[7] O. Koser, J. Ruckert, P. Ubl, Modelling and Optimization of Part Ejection in Magnesium High Pressure Die Casting, ESI Group, 2015.

[8] X.P. Niu, K.K. Tong, B.H. Hu, I. Pinwill, Cavity Pressure Sensor Study of the Gate Freezing Behaviour in Aluminium High Pressure Die Casting, Int. J. Cast Met. Res. 11 (1998) 105–112. https://doi.org/10.1080/13640461.1998.11819264.

Chapter 6: On the Probabilistic Nature of High-Pressure Die Casting

6.1 Introduction

This chapter unmasks the probabilistic nature of high-pressure die-casting (HPDC); specifically, the cause of the relatively high variability in mechanical properties. Previous investigations into the reliability of die-castings have pursued one of three lines of inquiry: the first relates the scatter in mechanical properties to statistical variations in melt quality [1–3]; the second derives empirical correlations between the mechanical properties and various measures of microstructural uniformity [4–8]; the third considers the stochastic nature of fluid flow, and the subsequent encapsulation of air and oxides [9–12]. Although porosity is a recurrent theme in these studies, its formation mechanism is widely disputed. Tian et al. [1] relate the amount of porosity to the number of inclusions in the melt; Li et al. [8] correlate the volume fraction of porosity to the fraction of primary α-Al_1 grains solidified in the shot chamber; Dong et al. [13] found that the use of vacuum can lead to fewer pores and improved tensile properties. While these studies provide valuable insight into the various factors influencing pore growth, they do not address the issue at hand.

This article builds upon prior work [14,15] wherein the authors simulate the HPDC process using a finite element model developed under the ProCAST (ESI Group) software platform; an optimum shot curve is derived in reference [15] based on predictions from the model. HPDC experiments are performed under both *Baseline* and *Optimized* conditions to identify critical casting defects and to describe their genesis. Based on these results, we elucidate the probabilistic nature of defect formation in the HPDC process.

6.2 Experimental

6.2.1 Casting Parameters

Fig. 6.1 shows the plunger speed profiles considered in this chapter. Notable differences lie in the speeds attained at displacements of 50 mm and 375 mm (Baseline {0.2 ms^{-1}; 0.3 ms^{-1}} and Optimized {0.4 ms^{-1}; 0.6 ms^{-1}}, respectively). The Baseline profile is defined according to Chapter 5. The Optimized profile is defined according to simulations performed by the authors [14,15], based on the amount and distribution of defects predicted by the model. A fast shot speed of 3.6 ms^{-1} was selected for both plunger speed profiles based on preliminary trials by the authors. An intensification pressure of 32 MPa was selected, corresponding to the maximum attainable pressure of the hydraulic actuator. A detailed description of the casting procedure can be found in Chapter 5.

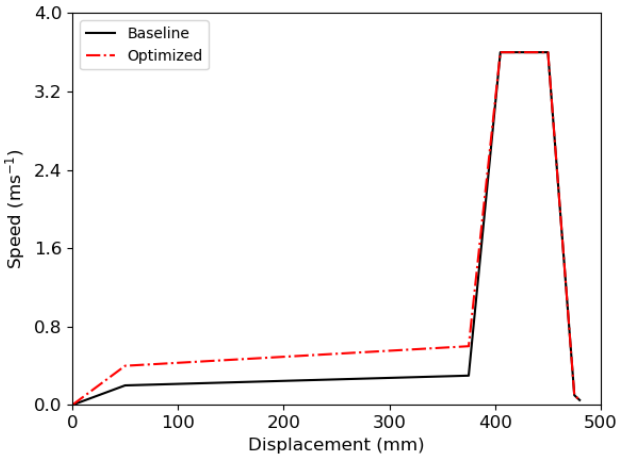

Fig. 6.1 Baseline and Optimized plunger speed profiles

6.2.2 X-ray Tomography

X-ray tomography was performed using a Xradia 410 Versa (Carl Zeiss AG) microtomography system operated with an accelerating voltage of 80 kV and a power of 10 W. An isotropic voxel was defined with a characteristic length of ~3.5 µm. The VGSTUDIO MAX (Volume Graphics GmbH) software suite was used to perform quantitative analyses on the three-dimensional volumes. An iterative surface determination was performed to isolate the material volume while compensating for local fluctuations in grey value. The VGDEFX module (Volume Graphics GmbH) was used to characterise voids and inclusions contained within the material volume.

6.3 Results

6.3.1 Mechanical Properties

Fig. 6.2 shows the tensile properties of specimens produced under Baseline and Optimized conditions; 95 % confidence ellipses are shown for two-dimensional normally distributed data. Average values and standard deviations are provided in Table 6.1. The average values and standard deviations are indifferent to the change in plunger speed profile. However, Fig. 6.2 shows that the variability in tensile strength, and tensile ductility, is greatly reduced under Optimized conditions (that is, if we define variability as significant *negative* deviations from the average property). For example, minimum values of 6.8 % and 9.4 % are obtained for the ductility of specimens produced under Baseline and Optimized conditions, respectively. A similar trend is also observed for tensile strength, with minimum values of 275 MPa and 282 MPa reported for the Baseline and Optimized conditions, respectively. The contrary is observed for 0.2 % proof strength, with minimum values of 143 MPa and 136 MPa obtained for the Baseline and Optimized conditions, respectively.

Table 6.1 Average tensile properties and standard deviations for samples produced under Baseline and Optimized conditions.

	0.2 % Proof Strength (MPa)	Tensile Strength (MPa)	Tensile Ductility (%)
Baseline	148±3 (min. 143)	292±4 (min. 275)	11.6±1.5 (min. 6.8)
Optimized	144±3 (min. 136)	294±4 (min. 282)	11.9±1.4 (min. 9.4)

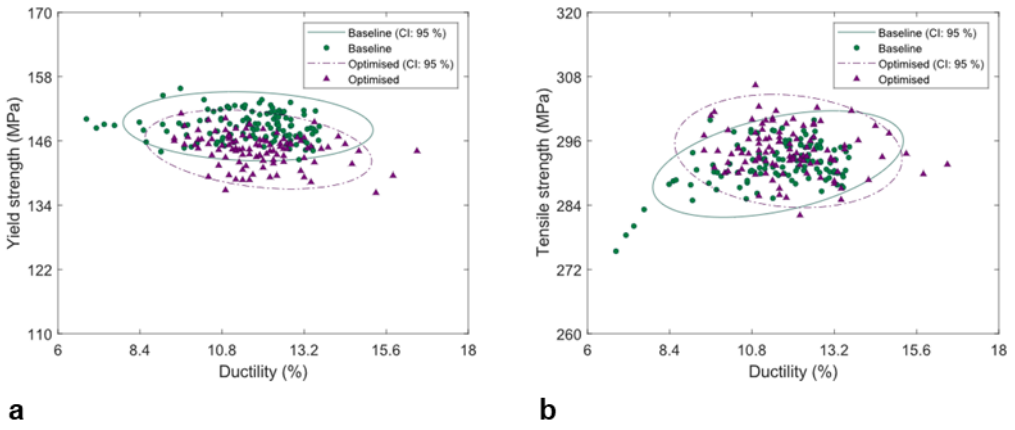

Fig. 6.2 Tensile properties of specimens produced under Baseline and Optimized conditions. 95 % confidence ellipses are shown for two-dimensional normally distributed data (CI: 95 %). (a) yield stress vs. tensile ductility. (b) tensile strength vs. tensile ductility. Tensile tests were performed in the F temper.

6.3.2 Porosity

X-ray tomography was used to characterise pores contained in the worst performing (min. ductility) tensile specimen from each group; preliminary work revealed that the effects of damage accumulation on pore size, and morphology, may be ignored due to the brittle nature of fracture. The volume of interest was defined from the upmost edge of the fracture surface, encompassing a volume of roughly 350 mm^3. Pore size was evaluated using the maximum Feret diameter method; unless otherwise stated, future reference to particle size will also imply use of the maximum Feret diameter method. In Fig. 6.3, the sphericity of each pore is plotted against its maximum Feret diameter (*D*). Here, sphericity refers to the ratio A_s/A_d where A_d is the surface area of the defect, and A_s is the surface area of a sphere with equivalent volume. Values of sphericity lie between zero and unity, with small values indicative of irregular morphology. Average values for pore size and sphericity are provided in Table 6.2. Although the average values are relatively unaffected, the change in plunger kinematics induces a significant decrease in the maximum pore size (from 1.32 mm to 0.37 mm). The irregular morphology of these large pores suggest that they originate from

solidification contractions and/or dilatational strains introduced during semi-solid deformation—as opposed to the expansion of a gaseous phase.

Table 6.2 Average size and sphericity of pores identified in the worst performing (min. ductility) tensile specimen produced under Baseline and Optimized conditions.

	Avg. pore size (mm)	Avg. sphericity
Baseline	0.05±0.02 (max. 1.32)	0.61±0.07 (min. 0.12)
Optimized	0.05±0.02 (max. 0.37)	0.59±0.07 (min. 0.29)

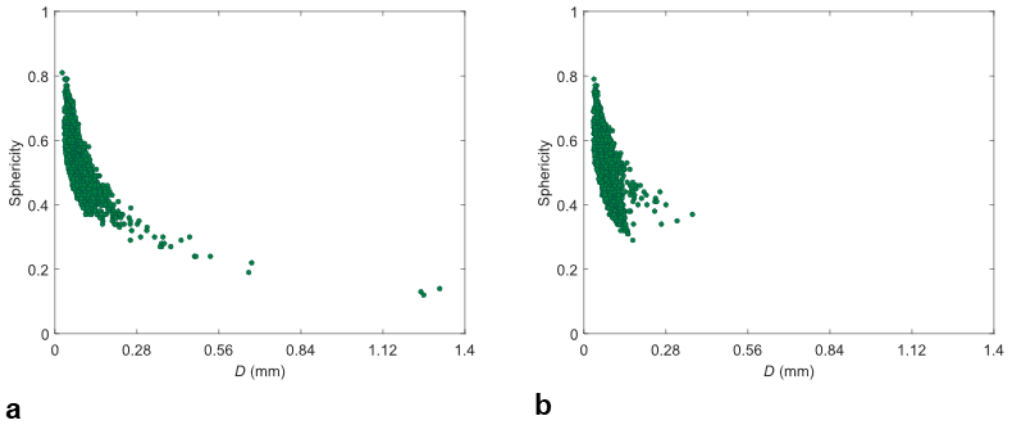

Fig. 6.3 Pore sphericity vs. maximum Feret diameter (*D*), for pores identified in the worst performing (min. ductility) tensile specimen produced under (a) Baseline, and (b) Optimized conditions.

6.3.3 Inclusions

Fig. 6.4(a) shows the largest pore observed on the fracture surface of the worst performing Baseline specimen. Large non-metallic inclusions can be seen within the pore; oxides are also observed in the vicinity of these inclusions. Pores are known to nucleate on non-wetted interfaces. Favourable nuclei include the non-wetted surfaces of oxide bifilms and certain non-metallic inclusions, particularly those comprising low-surface-tension liquids and non-wetted solids [16]. These inclusions, or the accompanying oxides, may act as nuclei for the pores observed in these specimens. Though inclusions in the worst performing specimens are relatively small, large non-metallic inclusions (0.4~0.7 mm) were observed on the fracture surface of other specimens with a tensile ductility in the range of 8~12 %. A representative micrograph of one such inclusion is shown in Fig. 6.4(b).

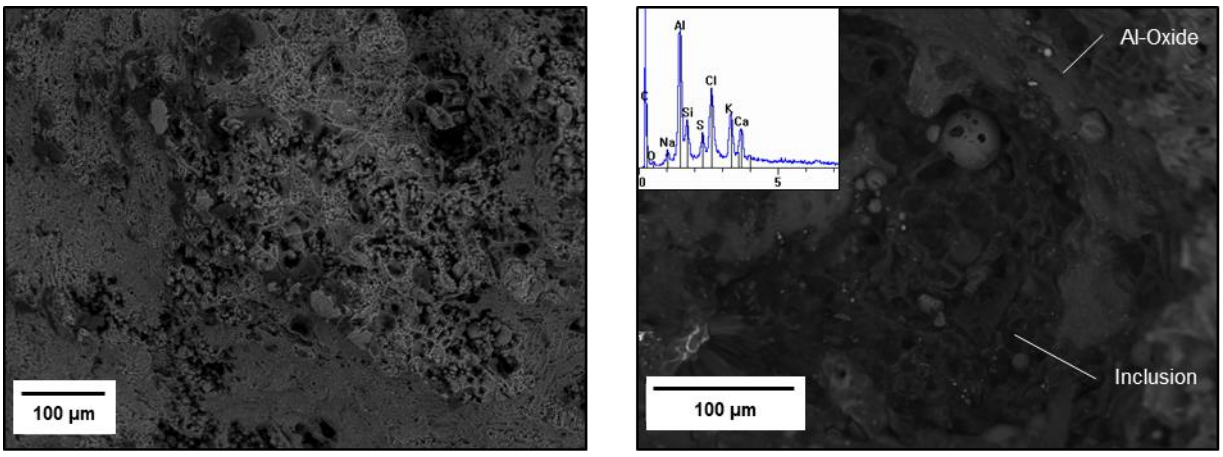

Fig. 6.4 Representative micrographs of defects observed on the fracture surface of tensile specimens. (a) Pore identified on the worst performing Baseline specimen. (b) Non-metallic inclusion; the insert in (b) shows a representative EDX spectrum acquired over an area of one such inclusion. Both images were obtained by detecting backscattered electrons in the SEM. Note that the scale differs in (a) and (b). In (b), the inclusion refers to the dark region towards the centre of the image, while the oxide refers to the lighter region circumscribing the darker inclusion.

6.3.4 Grain Structure

Fig. 6.5(a,b) show inverse pole figure (IPF) maps superimposed on band contrast images for the Baseline and Optimized samples, produced via EBSD mapping. The macroscopic direction for the IPF maps was taken to be parallel to the longitudinal axis of the tensile specimens. The grain structure is shown to comprise a mixture of large dendritic primary α-Al_1 grains (30~150 µm) solidified in the shot chamber, and smaller globular-rosette primary α-Al_2 grains (~10 µm) formed in the die cavity. The change in plunger speed profile appears to induce a refinement of both large primary α-Al_1 grains and smaller primary α-Al_2 grains. Fig. 6.5(c,d) show grain size distributions taken directly from the IPF maps in Fig. 6.5(a,b). Grain size distributions are often observed to approximate a lognormal shape [17]. Accordingly, we present grain size in terms of its natural logarithm (i.e. ln *D*). Clearly, the two distributions are multimodal—an observation that is more pronounced in the Baseline distribution. In accordance with previous studies [18,19], a threshold size of 30 µm was used to distinguish primary α-Al_1 grains from primary α-Al_2 grains. Primary α-Al_1 grains are, on average, smaller in the Optimized condition (42.0±13.8 µm) than in the Baseline condition (47.5±14.0 µm). A similar trend is observed for primary α-Al_2 grains, with average values of 9.0±5.4 µm and 8.0±5.0 µm reported for the Baseline and Optimized conditions, respectively. Additionally, we can infer from

the shape of the distributions that a more uniform grain structure is produced under Optimized conditions.

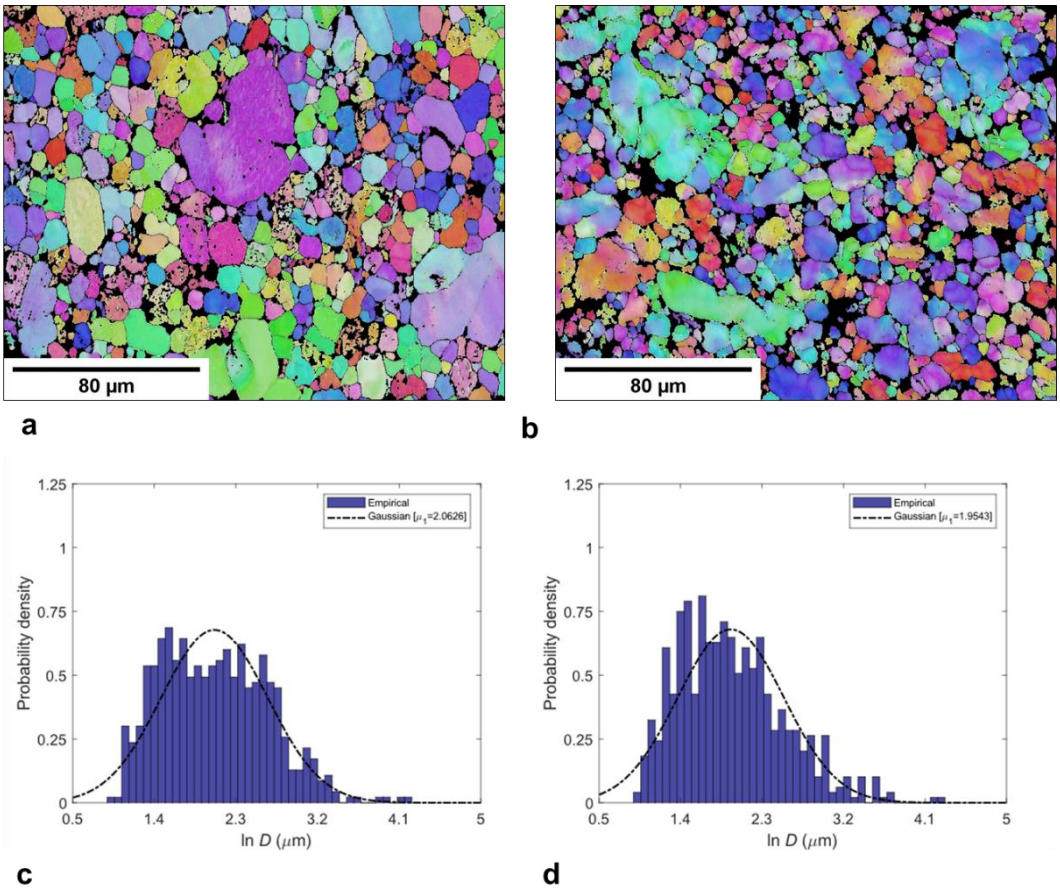

Fig. 6.5 EBSD Mapping of primary α-Al in specimens produced under (a,c) Baseline, and (b,d) Optimized conditions. Shown are IPF maps (a,b), and corresponding grain size distributions (c,d). Note that the grain size distributions in (c,d) are taken directly from the IPF maps in (a,b) and not from a larger data set of which the IPF maps are representative. Grain size is presented in terms of its natural logarithm, ln *D*, where *D* is the maximum Feret diameter of each grain. Fitted Gaussian functions, with expected value μ_1, are shown as dashpot lines in (c,d).

6.4 Discussion

6.4.1 Statistical Analysis of Tensile Ductility

Here, the generalized extreme value (GEV) distribution is used to model the limiting distribution of tensile ductility for specimens produced under Baseline and Optimized conditions. A detailed description of the GEV distribution is provided in Chapter 4 and reference [20]. The cumulative distribution function of the GEV distribution is

$$G(x) = \exp\left\{-\left[1+\xi\left(\frac{x-\mu}{\sigma}\right)\right]^{-1/\xi}\right\}, 1+\xi\left(\frac{x-\mu}{\sigma}\right) > 0$$

(6.1)

where μ, σ, and ξ describe the location, scale, and shape of the distribution respectively. $G(x)$ is equivalent to the Gumbel, Fréchet, and Weibull functions when $\xi \to 0$, $\xi > 0$, and $\xi < 0$, respectively. The quantile function is obtained by inverting (6.1) for $G(X) = 1 - p$:

$$X = \mu - \frac{\sigma}{\xi}\left[1 - \{-\log(1-p)\}^{-\xi}\right], \quad for\ \xi \neq 0,$$
$$X = \mu - \sigma \log\{-\log(1-p)\}, \qquad for\ \xi = 0 \tag{6.2}$$

where X is the return level associated with a return period m and probability $p = 1/m$. It is important to note that equations (6.1) and (6.2) are defined for the case of maxima, not minima. To model minima, we use the substitution $x_i = -y_i$, where y_i are our values of tensile ductility: small values of y_i now correspond to large values of x_i. Parameter estimates were obtained by maximum-likelihood estimation, with the sign correction $\tilde{\mu} = -\mu$. Parameter estimates and 95 % confidence intervals are provided in Table 6.3. The change in plunger kinematics has little effect on the threshold value $\tilde{\mu}$. However, the tail behaviour of the two distributions is markedly different. For example, the negative shape parameter $\xi = -0.481$ implies that the Optimized distribution possesses a finite upper bound of ~ -9.6 %. Conversely, the positive shape parameter $\xi = 0.102$ suggests that the Baseline distribution is boundless; the return level plots in Fig. 6.6 exemplify this disparity. To demonstrate the practical implications of ξ, let us consider a hypothetical design criterion requiring a minimum ductility of 10 %. From equation (6.2), we obtain scrap-rates of 12.5 % and 5.7 % for specimens produced under Baseline and Optimized conditions, respectively (i.e. $100/m$, for $X = -10$ %). Therefore, by changing the kinematics of the plunger we have effectively halved the scrap rates in our imaginary foundry.

Table 6.3 GEV parameter estimates used to model the limiting distribution of tensile ductility for specimens produced under Baseline and Optimized conditions.

	$\boldsymbol{\xi}$-mean	$\boldsymbol{\xi}$– 95 % Confidence Intervals	$\boldsymbol{\sigma}$	$\boldsymbol{\tilde{\mu}}$
Baseline	0.102	[-0.070; 0.275]	1.061	12.288
Optimized	-0.481	[-0.589; -0.373]	1.255	12.204

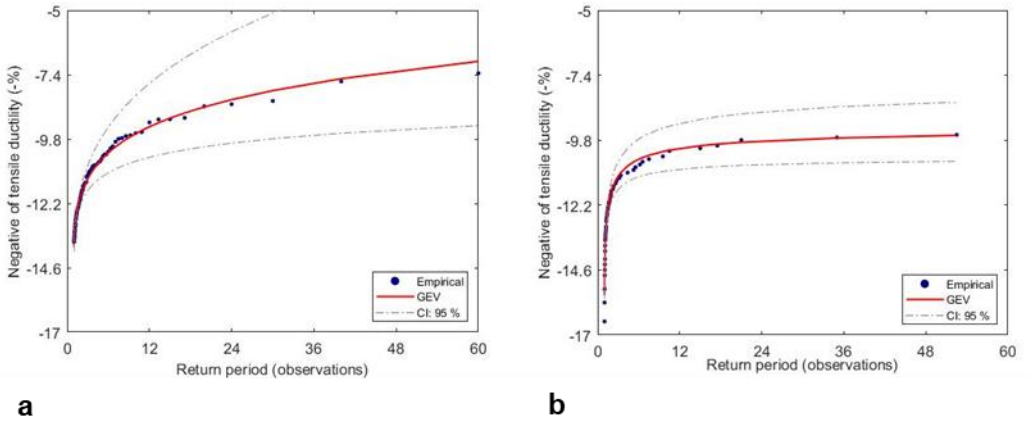

Fig. 6.6 Predicted values (GEV) of tensile ductility for the (a) Baseline, and (b) Optimized, specimens. The GEV curve was calculated from equation (6.2) for $x_i = -y_i$, where y_i denote our values of tensile ductility (hence units of - %). Its magnitude thus represents an upper limit to the minimum tensile ductility expected in a group of m specimens (abscissa). For comparison, experimental data points x_i are plotted in ascending order. Note that only unique values of x_i are considered (hence the upper limit of 60 observations). 95 % confidence intervals are shown as dashpot lines (CI: 95 %).

6.4.2 Source of Variability in Tensile Ductility

Fig. 6.7 plots the tensile ductility of a specimen against the size of the largest defect observed on its fracture surface; defects are classified as either porosity or non-metallic inclusions. A power-law relationship of the form, $y = ax^b$, was fitted to the overall data, as shown by the dashpot line in Fig. 6.7. The power-law accurately captures the behaviour of the empirical data (coefficient of determination: $R^2 = 0.856$) when the constants a and b take values of 7.77 and -0.302, respectively. From Fig. 6.7, it seems that inclusions ~0.75 mm in diameter have a similar effect on the tensile ductility as pores in the range of 0.96~1.60 mm. However, this is likely due to the location of these defects with respect to the specimen free surface, as opposed to the potency of the defects themselves—while pores typically congregate in the central core, non-metallic inclusions are often observed near to the specimen free surface. Strain localises more rapidly at surface defects and sub-surface defects compared to internal defects of an equivalent size [21]. Few oxides were observed on the fracture surfaces of the tensile specimens, and when they were observed they were relatively small in size; no other abnormalities were observed on the fracture surfaces. Based on these considerations, we infer that the observed variability in tensile ductility is related to variations in the size of pores and non-metallic inclusions, the origins of which we now discuss.

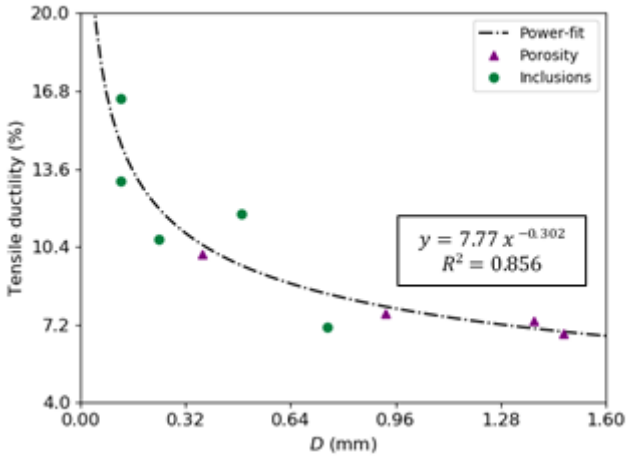

Fig. 6.7 Tensile ductility vs. maximum defect size (*D*). A power-law relationship is fitted to the overall data. R^2 denotes the coefficient of determination.

6.4.3 Origin of Non-Metallic Inclusions

Oil-based lubricants are often applied to the plunger tip to prevent wear and seizure. The tribological performance of such lubricants rely on the formation of a low-viscosity film between the contacting surfaces. When liquid metal enters the shot chamber, it reacts with organic compounds contained in the plunger lubricant to produce gaseous phases [22] and a carbonaceous residue [23]—this pyrolysis presents itself as a flame emerging from the pouring hole. This residue may be entrained into the liquid during solidification processing, materializing as non-metallic inclusions in the residual microstructure. Variations in inclusion size may then depend on the rate of build-up, and the viscous forces that lead to detachment and breakage.

EDX analysis—see insert of Fig. 6.4(b)—shows that these inclusions typically contain C, Na, S, Cl, K, and Ca. Due to its low atomic mass, the presence of C does not substantiate the pyrolysis hypothesis; C is also a common contaminant in electron microscopes. Let us, therefore, turn our attention to the heavier elements: Na, S, Cl, K and Ca. Petrochemical or synthetic based additives are often added to base stocks to impart additional properties to a lubricant. Extreme pressure additives enhance lubricity in high-pressure environments, and often contain compounds of S or Cl [24]. Other additives, such as surfactants and thickeners, are also used in commercial lubricants, and often contain compounds of Na, K and Ca [25]. To test the pyrolysis hypothesis, filling tests were performed by allowing the melt to solidify in the shot chamber with the plunger at rest. Large films, which closely resemble the non-metallic inclusions shown in Fig. 6.4(b), were identified on the surface of the solidified billets (Fig. 6.8). Hence, we propose that these non-metallic inclusions form during the pyrolysis of commercial plunger lubricants in the shot chamber. One might argue that the

aforementioned elements are also found in commercial foundry fluxes; however, no flux was used in the experiments.

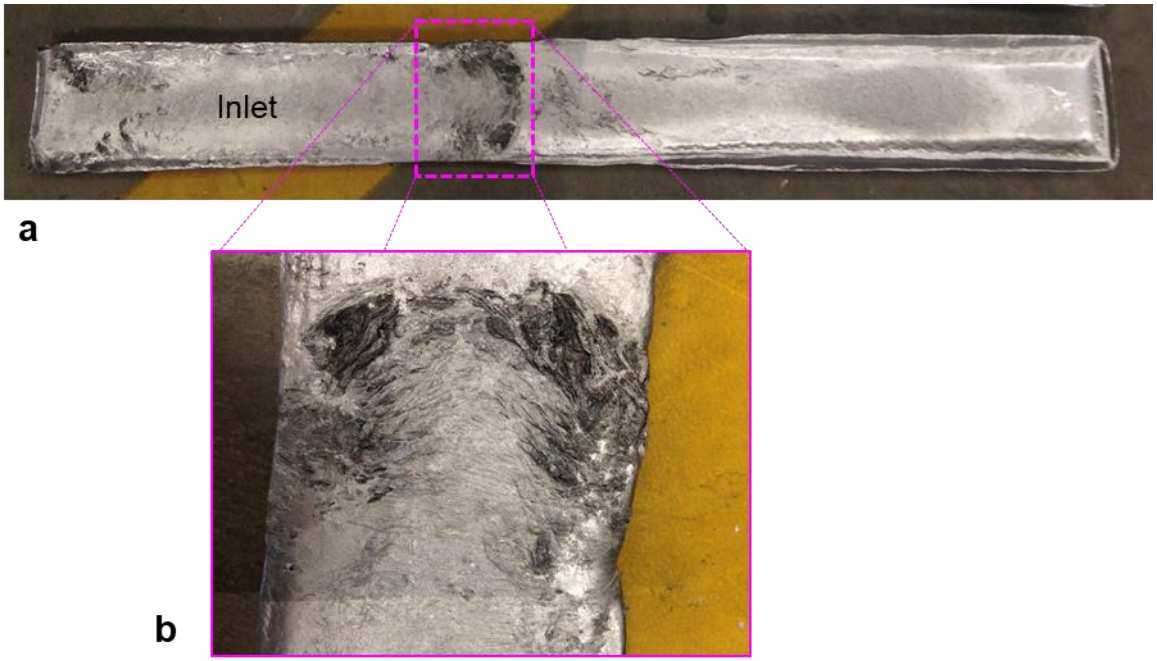

Fig. 6.8 Shot chamber filling tests performed to substantiate the pyrolysis hypothesis. Shown in (a) is a photograph of one such filling test sample, with a close up of the dashed region provided in (b). Large non-metallic inclusions, similar to that shown in Fig. 6.4 were observed on the surface of the solidified billets.

6.4.4 Origin of Porosity

Previously we found that a change in plunger kinematics may lead to a significant reduction in the maximum pore size; however, the average pore size remained relatively unchanged. We also attributed the observed variability in tensile ductility to variations in the size of these large pores. Fewer oxides are expected to accumulate in the casting under Optimized conditions (Fig. 6.9). However, no relationship was observed between the tensile ductility of a specimen and its position in the die. Furthermore, the average gas content is lower in the Optimized condition compared to the Baseline condition (Fig. 6.10). Although an increase in gas content would certainly expedite pore growth, it is unlikely that a small difference would have a significant effect. Moreover, one would expect the average pore size to also increase following an increase in the average gas content.

An alternative explanation lies in the response of the semi-solid alloy to shear deformation. Once die filling is complete, a pressure of ~32 MPa is applied to the solidifying alloy to compress gaseous phases and to assist in the feeding of shrinkage strains. Previous studies [26–29] have shown that

metallic alloys at 64∼93 % solid deform as near-cohesionless granular materials. The grains in a compacted granular assembly respond to compressive and shear loads by rearranging to form regions of contraction and dilation. Under compression, a pore will either contract or dilate depending on the solid fraction at which deformation occurs [26,27]. At low solid fractions, grains move towards one another, applying an external pressure on the pore, driving closure. At high solid fractions, grains are so densely packed that grain rearrangement leads to shear-induced dilation and pore growth. Kareh et al. [26] report a volumetric increase of ∼622 % for a pore in an Al-Cu alloy deformed at 93 % solid. The maximum volumetric strain encountered during deformation increases with the initial solid fraction [26,27]. Furthermore, the melt temperature at the end of die filling is 30 ^{o}C higher in the Optimized condition compared to the Baseline condition (Fig. 6.11). Thus, the change in plunger kinematics from Baseline to Optimized will lead to a decrease in the maximum volumetric strain encountered during semi-solid deformation. Dilatational strains are highly localised and time variant, and may lead to the formation of a new pore, or the sudden expansion of an existing pore. This dependency on the local microstructure may explain the seemingly random nature of pore formation in the HPDC process. This position is further supported by the grain size distributions in Fig. 6.5(c,d): a more uniform grain structure is expected to generate a more homogeneous strain field, thus reducing the scatter in pore size.

[This space intentionally left blank]

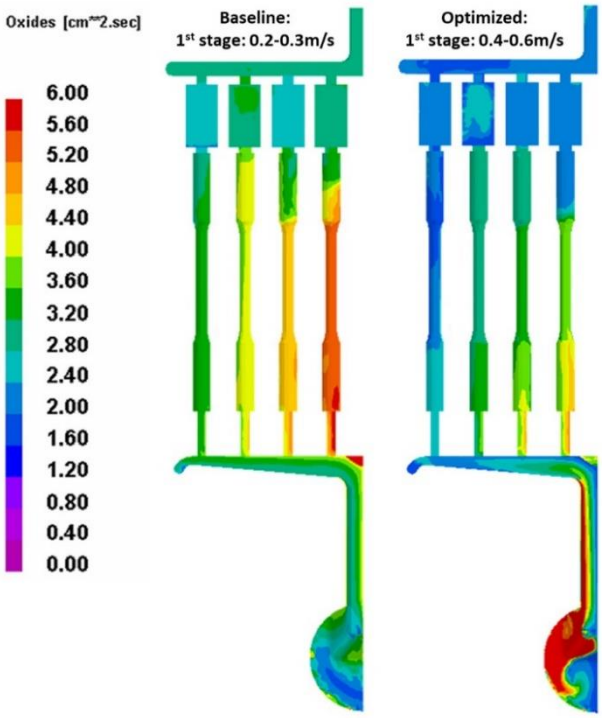

Fig. 6.9 Distribution of oxides in castings produced under Baseline (left) and Optimized (right) conditions. Oxides were predicted using the oxides indicator in ProCAST [15]. Simulation courtesy of Dr. Kun Dou.

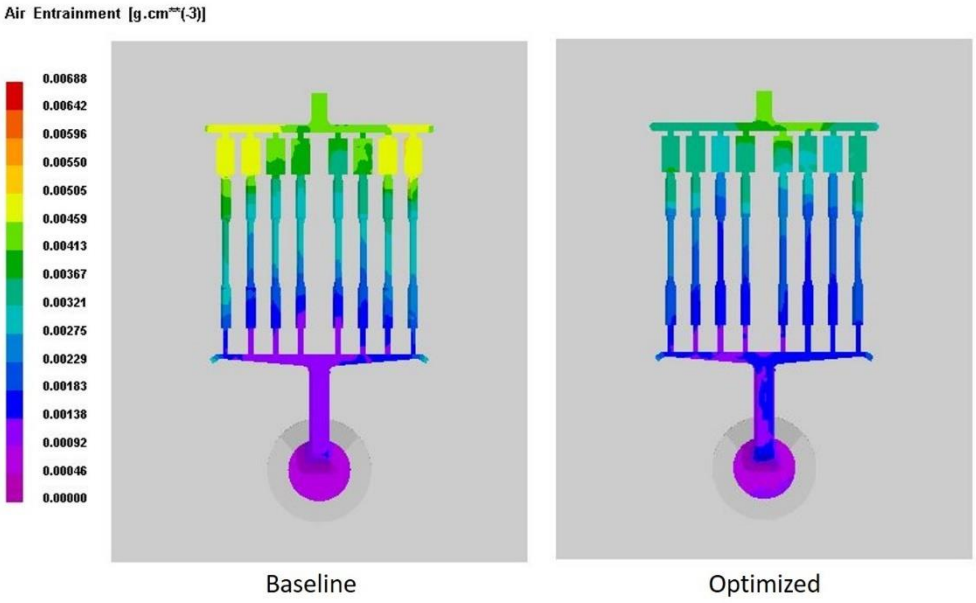

Fig. 6.10 Air entrainment in castings produced under Baseline (left) and Optimized (right) conditions. Air entrainment was predicted using the GAS model in ProCAST [15]. Simulation courtesy of Dr. Kun Dou.

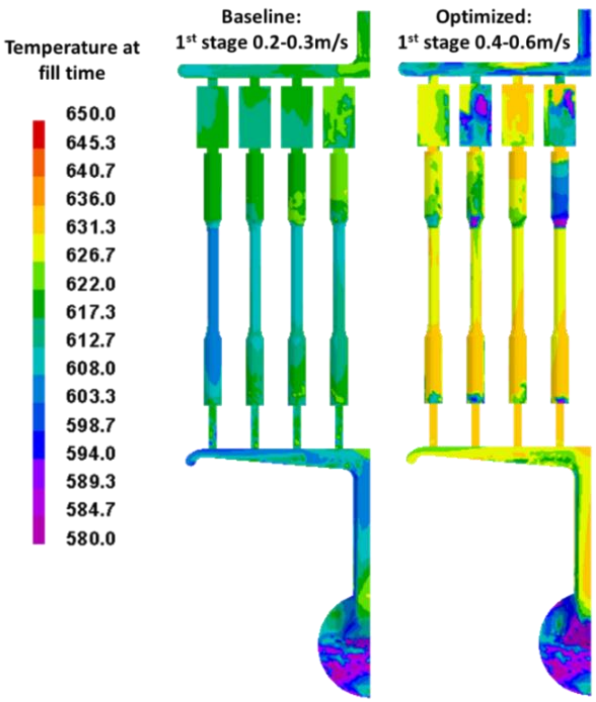

Fig. 6.11 ProCAST simulations depicting melt temperature at the end of die filling for castings produced under Baseline and Optimized Conditions [15]. Simulation courtesy of Dr. Kun Dou.

6.4.5 Representativity of the Baseline Process

To ensure our findings are indeed representative of industry, fatigue specimens were machined from automotive components produced by HPDC. Various alloys were studied for samples produced by different suppliers. Crack initiating defects were identified via SEM fractography. Critical casting defects were identified as porosity, oxide films, and non-metallic inclusions—a representative BSE micrograph is shown in Fig. 6.12. Although, the Baseline process appears to be representative of industrial practice, oxides are more prominent in the automotive castings compared to Baseline samples. This is attributed to the increased geometric complexity of automotive components, and the use of sub-optimal melt handling procedures in commercial foundries (it is more difficult to control melt cleanliness in a commercial foundry than it is in a laboratory environment). As the suppliers cannot disclose their practices, we are unable to dismiss the use of foundry flux during casting.

[This space intentionally left blank]

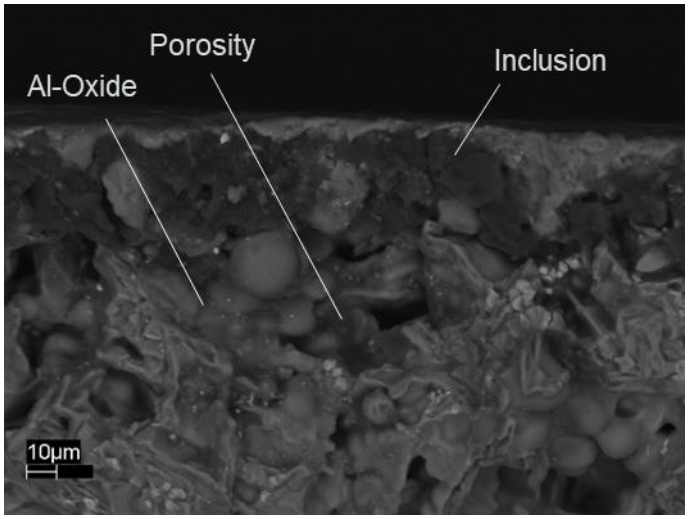

Fig. 6.12 Casting defects identified on the fracture surface of fatigue specimens machined from automotive components. Critical casting defects were identified as porosity, oxides, and non-metallic inclusions.

6.5 Summary

In a prior work [15], the authors simulated the HPDC process using a finite element model developed under the ProCAST software platform; an optimum shot curve was derived based on predictions from the model. Here, a *Baseline* HPDC process is established that is representative of commercial foundry practice. The variability in tensile ductility, of specimens produced under these conditions, is attributed to variations in the size of large pores and non-metallic inclusions. It is proposed that these non-metallic inclusions form during the pyrolysis of commercial plunger lubricants in the shot chamber.

The variability in tensile ductility is greatly reduced under *Optimized* conditions which is attributed to a significant reduction of the maximum pore size from 1.32 mm to 0.37 mm. We propose that these large pores derive from dilatational strains introduced during semi-solid deformation. The seemingly probabilistic nature of pore formation is thus attributed to variations in the local grain structure surrounding a liquid channel.

6.6 References

[1] C. Tian, J. Law, J. van der Touw, M. Murray, J.-Y. Yao, D. Graham, D. St. John, Effect of Melt Cleanliness on the Formation of Porosity Defects in Automotive Aluminium High Pressure Die Castings, J. Mater. Process. Technol. 122 (2002) 82–93. https://doi.org/10.1016/S0924-0136(01)01229-8.

[2] G. Timelli, A. Fabrizi, The Effects of Microstructure Heterogeneities and Casting Defects on the Mechanical Properties of High-Pressure Die-Cast AlSi9Cu3(Fe) Alloys, Metall. Mater. Trans. A 45 (2014) 5486–5498. https://doi.org/10.1007/s11661-014-2515-7.

[3] S. Ferraro, G. Timelli, Influence of Sludge Particles on the Tensile Properties of Die-Cast Secondary Aluminum Alloys, Metall. Mater. Trans. B 46 (2015) 1022–1034. https://doi.org/10.1007/s11663-014-0260-3.

[4] H. Gjestland, S. Sannes, J. Svalestuen, H. Westengen, Optimizing the Magnesium Die Casting Process to Achieve Reliability in Automotive Applications, SAE Transactions. 114 (2005) 67–73.

[5] S. Ji, W. Yang, F. Gao, D. Watson, Z. Fan, Effect of Iron on the Microstructure and Mechanical Property of Al–Mg–Si–Mn and Al–Mg–Si Diecast Alloys, Mater. Sci. Eng.: A 564 (2013) 130–139. https://doi.org/10.1016/j.msea.2012.11.095.

[6] H. Yang, S. Ji, D. Watson, Z. Fan, Repeatability of Tensile Properties in High Pressure Die-Castings of an Al-Mg-Si-Mn Alloy, Met. Mater. Int. 21 (2015) 936–943. https://doi.org/10.1007/s12540-015-5108-0.

[7] X. Li, S.M. Xiong, Z. Guo, On the Porosity Induced by Externally Solidified Crystals in High-Pressure Die-Cast of AM60B Alloy and its Effect on Crack Initiation and Propagation, Mater. Sci. Eng.: A 633 (2015) 35–41. https://doi.org/10.1016/j.msea.2015.02.078.

[8] X. Li, S.M. Xiong, Z. Guo, Improved Mechanical Properties in Vacuum-Assist High-Pressure Die Casting of AZ91D Alloy, J. Mater. Process. Technol. 231 (2016) 1–7. https://doi.org/10.1016/j.jmatprotec.2015.12.005.

[9] K. Dou, E. Lordan, Y.J. Zhang, A. Jacot, Z.Y. Fan, Numerical Simulation of Fluid Flow, Solidification and Defects in High Pressure Die Casting (HPDC) Process, IOP Conf. Ser.: Mater. Sci. Eng. 529 (2019) 012058. https://doi.org/10.1088/1757-899X/529/1/012058.

[10] M. Saeedipour, S. Schneiderbauer, S. Pirker, S. Bozorgi, A Numerical and Experimental Study of Flow Behavior in High Pressure Die Casting, in: M. Alderman, M.V. Manuel, N. Hort, N.R. Neelameggham, Magnesium Technol. (2014) 185–190. https://doi.org/10.1007/978-3-319-48231-6_37.

[11] D.R. Gunasegaram, M. Givord, R.G. O'Donnell, B.R. Finnin, Improvements Engineered in UTS and Elongation of Aluminum Alloy High Pressure Die Castings Through the Alteration of

Runner Geometry and Plunger Velocity, Mater. Sci. Eng.: A 559 (2013) 276–286. https://doi.org/10.1016/j.msea.2012.08.098.

[12] X. Li, W. Yu, J. Wang, S. Xiong, Influence of Melt Flow in the Gating System on Microstructure and Mechanical Properties of High Pressure Die Casting AZ91D Magnesium Alloy, Mater. Sci. Eng.: A 736 (2018) 219–227. https://doi.org/10.1016/j.msea.2018.08.090.

[13] X. Dong, X. Zhu, S. Ji, Effect of Super Vacuum Assisted High Pressure Die Casting on the Repeatability of Mechanical Properties of Al-Si-Mg-Mn Die-Cast Alloys, J. Mater. Process. Technol. 266 (2019) 105–113. https://doi.org/10.1016/j.jmatprotec.2018.10.030.

[14] K. Dou, E. Lordan, Y.J. Zhang, A. Jacot, Z.Y. Fan, A Complete Computer Aided Engineering (CAE) Modelling and Optimization of High Pressure Die Casting (HPDC) Process, J. Manuf. Process. 60 (2020) 435-446. https://doi.org/10.1016/j.jmapro.2020.10.062.

[15] K. Dou, E. Lordan, Y. Zhang, A. Jacot, Z. Fan, Improvement of Mechanical Properties for Aluminium Alloy in High Pressure Die Casting (HPDC) Process Combining Experimental and Modelling Approach, manuscript submitted for publication (2020).

[16] J. Campbell, Castings - 2nd Edition, Butterworth-Heinemann, 2002.

[17] R.B. Bergmann, A. Bill, On the Origin of Logarithmic-Normal Distributions: an Analytical Derivation, and its Application to Nucleation and Growth Processes, J. Crystal Growth 310 (2008) 3135–3138. https://doi.org/10.1016/j.jcrysgro.2008.03.034.

[18] S. Otarawanna, C.M. Gourlay, H.I. Laukli, A.K. Dahle, Microstructure Formation in AlSi4MgMn and AlMg5Si2Mn High-Pressure Die Castings, Metall. Mat. Trans. A 40 (2009) 1645–1659. https://doi.org/10.1007/s11661-009-9841-1.

[19] S. Otarawanna, C.M. Gourlay, H.I. Laukli, A.K. Dahle, Agglomeration and Bending of Equiaxed Crystals During Solidification of Hypoeutectic Al and Mg Alloys, Acta Mater. 58 (2010) 261–271. https://doi.org/10.1016/j.actamat.2009.09.002.

[20] S. Coles, An Introduction to Statistical Modeling of Extreme Values, Springer-Verlag, London, 2001. https://doi.org/10.1007/978-1-4471-3675-0.

[21] A. Borbély, H. Mughrabi, G. Eisenmeier, H.W. Höppel, A Finite Element Modelling Study of Strain Localization in the Vicinity of Near-Surface Cavities as a Cause of Subsurface Fatigue Crack Initiation, Int. J. Fract. 115 (2002) 227–232. https://doi.org/10.1023/A:1016350528652.

[22] L. Wang, P. Turnley, G. Savage, Gas Content in High Pressure Die Castings, J. Mater. Process. Technol. 211 (2011) 1510–1515. https://doi.org/10.1016/j.jmatprotec.2011.03.024.

[23] Tribo-chemie GmbH, The Thermal Reaction of Different Plunger Lubricants and its Influence on Casting Quality, https://tribo-chemie.de/images/media/downloads/EN/plungerlubricant.pdf (accessed August 20, 2020).

[24] T. Mang, W. Dresel, Lubricants and Lubrication, John Wiley & Sons Inc., Weinheim, 2007.

[25] ATC Europe, Lubricant Additives: Use and Benefits, 2016. https://www.atc-europe.org/public/Document%20118%20-%20Lubricant%20Additives%20Use%20and%20Benefits.pdf (accessed August 20, 2020).

[26] K.M. Kareh, P.D. Lee, R.C. Atwood, T. Connolley, C.M. Gourlay, Revealing the Micromechanisms Behind Semi-Solid Metal Deformation with Time-Resolved X-Ray Tomography, Nat. Commun. 5 (2014) 4464. https://doi.org/10.1038/ncomms5464.

[27] K.M. Kareh, P.D. Lee, R.C. Atwood, T. Connolley, C.M. Gourlay, Pore Behaviour During Semi-Solid Alloy Compression: Insights into Defect Creation Under Pressure, Scripta Mater. 89 (2014) 73–76. https://doi.org/10.1016/j.scriptamat.2014.06.033.

[28] C.M. Gourlay, A.K. Dahle, Dilatant Shear Bands in Solidifying Metals, Nat. 445 (2007) 70–73. https://doi.org/10.1038/nature05426.

[29] T.C. Su, C. O'Sullivan, T. Nagira, H. Yasuda, C.M. Gourlay, Semi-Solid Deformation of Al-Cu Alloys: A Quantitative Comparison Between Real-Time Imaging and Coupled LBM-DEM Simulations, Acta Mater. 163 (2019) 208–225. https://doi.org/10.1016/j.actamat.2018.10.006.

Chapter 7: Turbulent Breakup of Non-Metallic Inclusions and Equiaxed Crystals During Solidification of a Hypoeutectic Al-Si Alloy.

7.1 Introduction

The breakup of bodies and aggregates suspended in a turbulent flow are important phenomena that influence many aspects of commercial casting processes. For example, in melt-conditioned direct-chill casting the de-agglomeration and forced wetting of oxide inclusions (e.g. native MgO particles in Mg alloys [1]) creates copious nuclei for heterogeneous nucleation of solidification, which leads to grain refinement [2]. Breakup also plays a prominent role in die casting processes where defect-forming suspensions, such as gas bubbles [3,4] and oxide films [5], are readily transported by the bulk-liquid flow. Such defects adversely affect the fracture properties of die-cast structures by introducing considerable scatter in the material response [6].

The principal approach to controlling melt quality is to perform treatments on the liquid prior to solidification processing. These treatments typically involve the use of an external field to impart a force on the liquid, either directly by agitation [7,8] or indirectly through ultrasonic cavitation [9]. De-agglomeration, in both cases, takes place by a process of erosion, in which particulate matter detaches from the agglomerate surface in response to an external stress [9,10]. Extrinsic melt treatments may not always be appropriate for the solidification process, e.g. in HPDC the benefits of melt treatment are somewhat vitiated once the liquid is transferred into the shot chamber. Inside the shot chamber, some uncontrolled solidification takes place producing a multi-phase mixture consisting of up to 30 vol.% solid [11]. This multiphase flow—which carries an array of defect-forming suspensions—is transported at high speeds through a narrow orifice system where it is subject to shear rates in the order of 10^4∼10^5 s^{-1} [12]. Once die filling is complete, an intensification pressure of 30∼100 MPa [12] is applied to the casting to assist in the feeding of shrinkage strains. The shear rates during die filling are of a similar magnitude to those found in melt-conditioning (10^5∼10^6 s^{-1} [8]), where breakage has previously been evidenced [3,7,8]. This invites an obvious question: can we manipulate fluid flow in such a way as to encourage breakage during the transportation of liquid metals?

An aggregate suspended in a turbulent flow is subject to a hydrodynamic stress that fluctuates intermittently [13]. Viscous forces act on external particles of the aggregate and propagate inwards through a series of inter-particle collisions, causing stress to accumulate in vulnerable branches of the aggregate [14]. When an aggregate is small, with respect to the Kolmogorov length scale, it rotates in the flow like a rigid body and no structural change is observed [15]. Breakup occurs when a turbulent oscillation is violent enough to generate an internal stress that exceeds the cohesive strength of the inter-particle bonds, releasing a small fragment of the aggregate into the liquid

[13,14,16–18]. For large aggregates, the breakage rate function is believed to follow a power-law relationship [13,17,19]:

$$d \propto \dot{\gamma}_{\mathrm{eff}}{}^{-m},$$

$$\dot{\gamma}_{\mathrm{eff}} = \sqrt{\langle \varepsilon \rangle / \nu},$$

(7.1)

where d is the size of the aggregate and m is the breakage exponent; $\dot{\gamma}_{\mathrm{eff}}$ is the effective mean shear rate for the turbulent flow which is determined by the kinematic viscosity ν and mean kinetic energy dissipation rate $\langle \varepsilon \rangle$. Previous studies on aggregate breakage in solid-liquid [15,17,18] and liquid-liquid [20] systems have demonstrated that particle disruption depends on the flow field intensity, the strength of the particle, and the particle residence time. In HPDC, several researchers posit that the shear rates during die filling are large enough to incite aggregate breakage [21], dendrite fragmentation [22] and bubble disintegration [4,21]—however, many of the ideas in these papers are incomplete.

At present, an *in-situ* study of turbulent breakup in metallic alloy systems is not feasible. Liquid metals are opaque, preventing the use of optical techniques such as particle-tracking velocimetry. Moreover, synchrotron X-ray imaging does not meet the spatial and temporal requirements of such a study. The present contribution, therefore, infers the existence of breakage from the as-cast microstructure. HPDC samples are produced using two die geometries, which differ in the attainable levels of turbulent energy dissipation. X-ray tomography, machine learning, and electron backscatter diffraction (EBSD) mapping are used to quantify the size, shape and spatial distribution of inclusions, pores, and equiaxed grains in the residual microstructures. Numerical simulations of the HPDC process are performed in ProCAST (ESI Group) to quantify the three-dimensional flow field and to relate the derived quantities to breakage. We demonstrate that fluid flow can be manipulated in such a way as to encourage breakup, leading to significant improvements in both tensile strength and tensile ductility.

7.2 Method

LM24 alloy (8.09 % Si, 3.11 % Cu, 1.78 % Zn, 0.86 % Fe, 0.22 % Mn, 0.16 % Mg, and 0.04 % Ti) supplied by Norton UK was used as a base material. HPDC experiments were performed using the methodology outlined in Chapter 5. Fig. 7.1 presents the two die geometries used to produce ASTM standard [23] tensile specimens (gauge length and gauge diameter are 50 mm and 6.35 mm, respectively). The two dies differ in their choice of runner system: one adopts a traditional runner

system (TRS); the other employs a lean runner system (LRS), which aims to accelerate the liquid through a contractile flow.

HPDC is a multiphysical process characterised by a range of complex, interrelated phenomena: solidification, turbulence and free surface behaviour to name a few. Analytical studies must therefore address all aspects of the HPDC process, from the initial pouring of liquid into the shot chamber to final solidification in the die cavity. Numerical simulations were performed in ProCAST using the methodology outlined in reference [24]. Fluid turbulence was described using a standard k-ε turbulence model described in references [25–27].

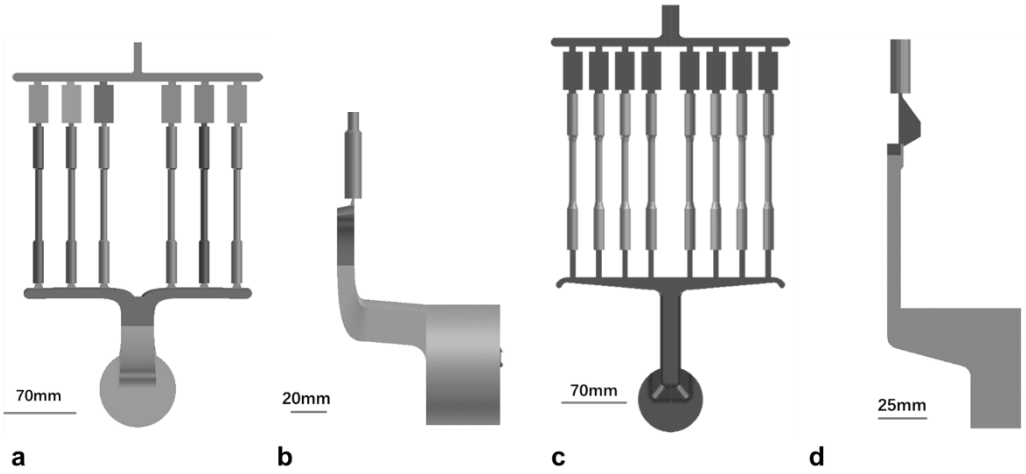

Fig. 7.1 Die geometries used to produce ASTM standard tensile specimens: (a,b) the TRS geometry, which employs a conventional runner; and (c,d) the LRS geometry, which aims to accelerate the liquid through a flow constriction. Shown in (b) and (d) are side views of the TRS and LRS, respectively.

7.3 Results

7.3.1 Tensile Properties

Fig. 7.2 presents the tensile properties of samples produced using the TRS and LRS casting geometries; 95 % confidence ellipses are shown for two-dimensional normally distributed data. Clearly, the flow constriction in the LRS leads to significant improvements in tensile strength (mean: +16 %) and tensile ductility (mean: +65 %); the increase in 0.2 % proof strength (mean: +10 %) is more modest in comparison. Similar observations have been reported by Gunasegaram et al. [21] for a wide range of melt velocities.

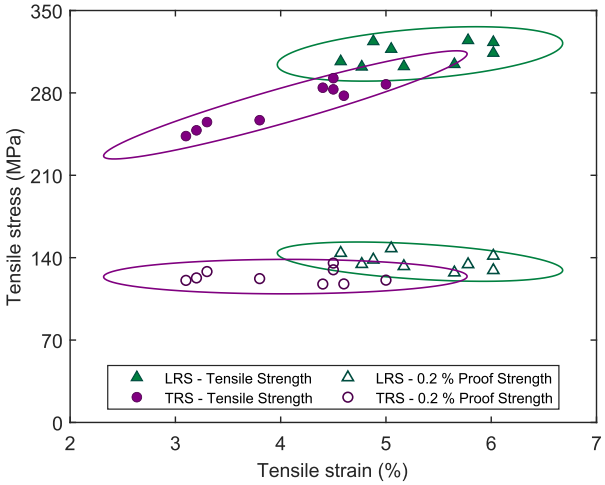

Fig. 7.2 Tensile properties and associated 95 % confidence ellipses for two-dimensional normally distributed data. Tensile tests were performed in the F temper.

7.3.2 Inclusions

Fig. 7.3 presents a three-dimensional visualisation of inclusions in the TRS and LRS samples, produced via X-ray tomography. Inclusion size was determined using the maximum Feret diameter method. Note: unless otherwise stated, future reference to particle size also implies use of the maximum Feret diameter method. Inclusions detected in the LRS sample are, on average, smaller than their TRS counterparts, with average diameters of 0.09 ± 0.03 mm (max. 0.37 mm) and 0.15 ± 0.08 mm (max. 0.73 mm), respectively. While still significant, the difference in the means is modest compared to that of the maximum values. Fig. 7.3(c) presents the probability distributions of inclusion size for the two materials. Clearly, there is a marked difference in the tails of the two distributions. Inclusions in the LRS sample also possess a more compact morphology than those in the TRS sample, with an average compactness of 0.28 ± 0.12 and 0.20 ± 0.11 reported for each sample, respectively. Here, compactness refers to the ratio V_i/V_s, where V_i is the volume of the inclusion and V_s the volume of its enclosing sphere. Values of compactness lie between zero and unity, with low values indicative of irregular morphology. Regarding the spatial distribution of inclusions, inclusions are more uniformly distributed in the LRS sample compared to the TRS sample.

[This space is intentionally left blank]

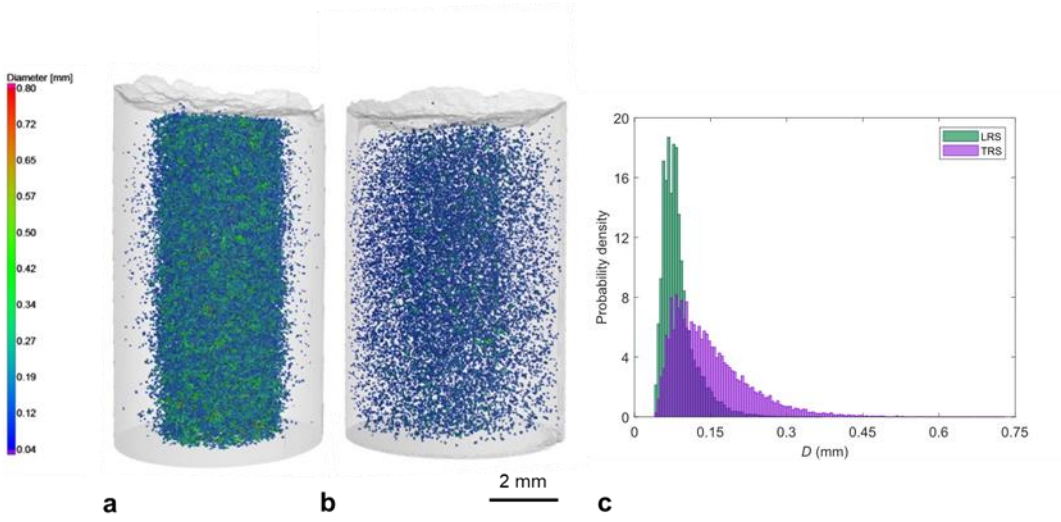

Fig. 7.3 Three-dimensional visualisation of inclusions within each sample, produced via X-ray tomography: (a) TRS sample, (b) LRS sample, and (c) corresponding size distributions.

7.3.3 Porosity

Fig. 7.4 displays a three-dimensional visualisation of porosity in the TRS and LRS samples; corresponding size distributions are shown in Fig. 7.4(c). Although the mean pore sizes are relatively similar, there is a notable difference in the tails of the two distributions. For example, the average pore size is 0.08 ± 0.02 mm (max. 0.28 mm) for the TRS sample and 0.07 ± 0.04 mm (max. 0.40 mm) for the LRS sample. Pores in both samples are highly spherical, with average sphericities of 0.61 ± 0.05 and 0.61 ± 0.07 reported for the TRS and LRS samples, respectively. This implies that most of these pores originate from gaseous sources as opposed to solidification shrinkage or dilatational strains [6]. Concerning the spatial distribution of pores, microporosity appears to concentrate towards the centreline flow, mimicking the shape of a conical screw. Moreover, the largest of these pores are randomly distributed in space, again implying gaseous origins: one would expect shrinkage porosity to congregate in the central core.

[This space is intentionally left blank]

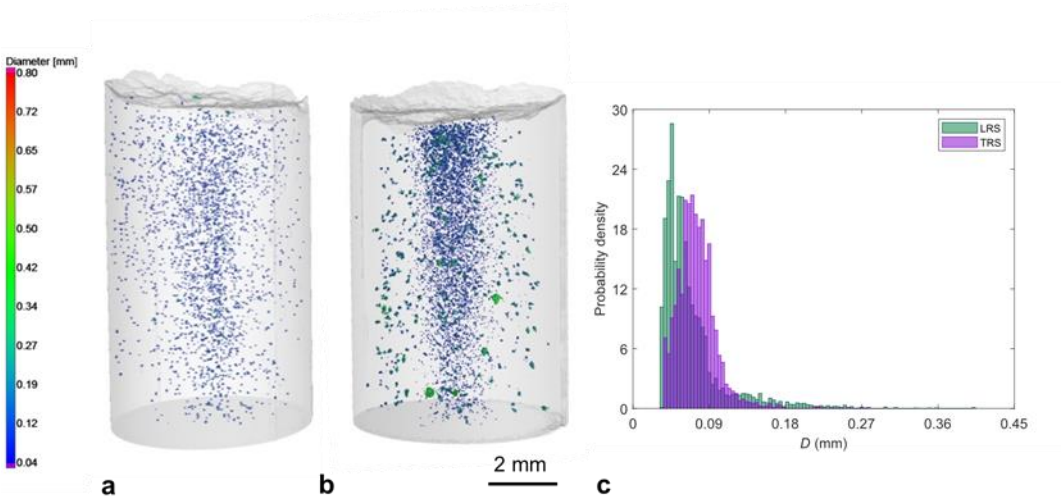

Fig. 7.4 Three-dimensional visualisation of porosity within each sample, produced via X-ray tomography: (a) TRS sample, (b) LRS sample, and (c) corresponding size distributions.

7.3.4 Grain Structure

Fig. 7.5 show inverse pole figure (IPF) maps superimposed on band contrast images obtained for the TRS and LRS samples, produced via EBSD mapping. The grain structure is shown to comprise both large dendritic primary α-Al_1 grains solidified in the shot chamber and smaller globular-rosette primary α-Al_2 grains formed in the die cavity. Although the primary α-Al_1 grains are relatively similar in size, it appears that the flow constriction in the LRS leads to a significant refinement of the smaller primary α-Al_2 grains.

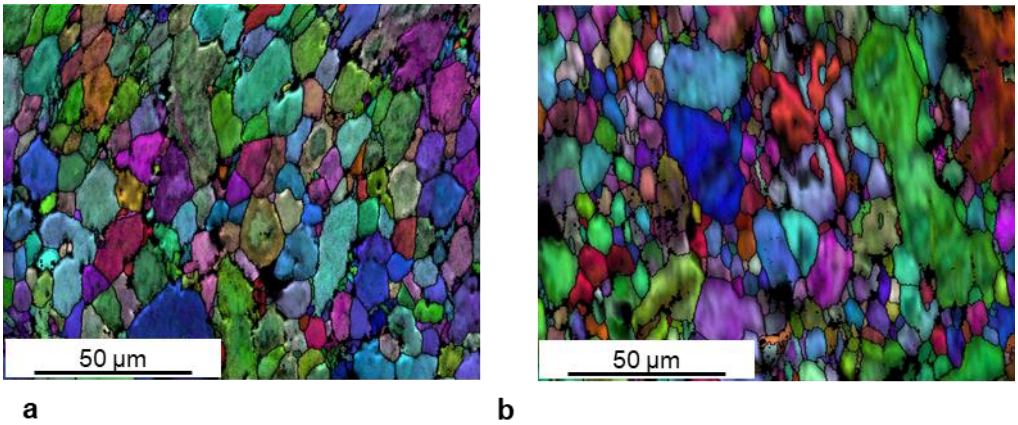

Fig. 7.5 Visualisation of grain morphology acquired via EBSD mapping. Shown are IPF maps superimposed on band contrast images obtained for the (a) TRS sample, and (b) LRS sample.

7.3.5 Numerical Modelling

Numerical simulations were performed in ProCAST to quantify the three-dimensional flow field and to relate the derived quantities to breakage. Fig. 7.6 compares the dissipation rate of turbulent energy ε along the flow path of the two die geometries. The flow constriction in the LRS leads to levels of ε that are an order of magnitude higher than in the TRS. Moreover, the melt is exposed to

this high-energy flow for a prolonged period in the LRS due to its increased pipe length. In both dies, the melt experiences high ε just upstream of the orifice system, the intensity of which varies with position—the initial jets quickly traverse the length of the die, reaching the far wall before filling back towards the orifice system, impeding the flow of newly arriving fluid [28]. In the TRS geometry, high levels of ε are also observed downstream of certain orifices, a phenomenon which is not observed in the LRS casting. This is attributed to the abrupt orifice design employed in the TRS geometry (Fig. 7.1(b)). In contrast, the LRS geometry employs a flow buffer (Fig. 7.1(d)) which aims to reduce turbulence prior to die filling.

Fig. 7.7 shows the temperature of the liquid at the end of die filling. Note that the temperature of the melt in the LRS casting is below the liquidus temperature (614 ^{o}C) of the alloy, which was calculated using a database supported by the ESI Group [27]. The same is not true for the TRS casting: the lean geometry employed in the LRS is shown to promote heat extraction leading to increased cooling rates.

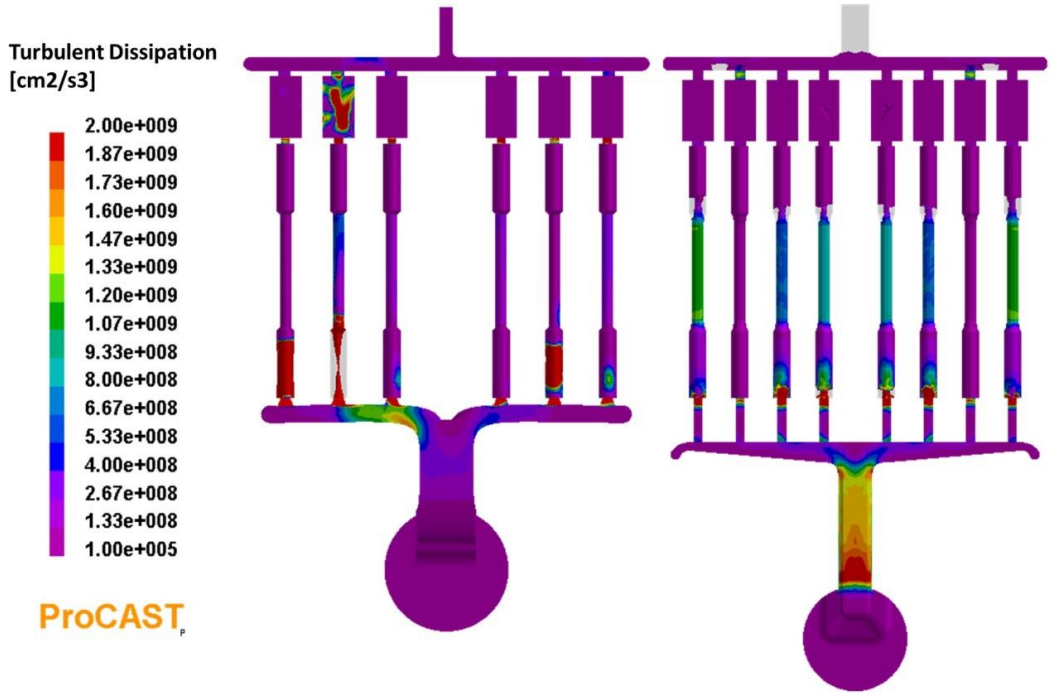

Fig. 7.6 Turbulent energy dissipation rate along the flow path of the TRS (left) and LRS (right) die geometries; numerical simulations were performed using ProCAST code. Courtesy of Dr. Kun Dou.

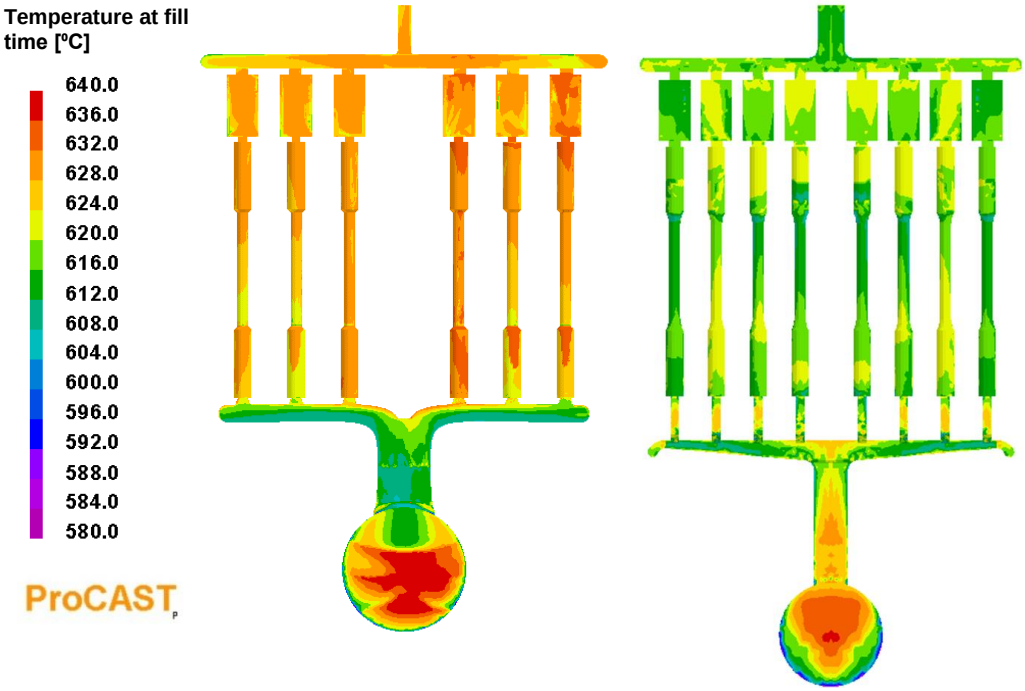

Fig. 7.7 ProCAST simulations depicting the melt temperature at the end of die filling, for the TRS (left) and LRS (right) die geometries. Courtesy of Dr. Kun Dou.

7.4 Discussion

7.4.1 Statistical Modelling of Extreme Values

Although the average inclusion/pore sizes presented in Fig. 7.3 and Fig. 7.4 are relatively similar, there is a marked difference in the tails of the distributions. Accordingly, the generalized Pareto (GP) distribution was used to model tail data; a detailed description of the GP distribution is provided in Chapter 4. A suitable threshold u was determined for each data set using the threshold stability property of the GP distribution. Parameter estimates were obtained by maximum likelihood estimation using the Statistics and Machine Learning Toolbox™ in MATLAB (Mathworks).

7.4.2 Inclusions

The GP distribution was used to model the upper tail of the inclusion size distributions shown in Fig. 7.3(c). Parameter estimates for the fitted distributions are shown in Table 7.1. The threshold value u of the TRS distribution is significantly larger than that of the LRS distribution. There is also a notable difference in the tail behaviour of the two distributions. For example, the negative shape parameter $\xi = -0.132$ implies that the LRS distribution possesses a finite upper bound of ~0.49 mm. In contrast, $\xi \to 0$ indicates that the TRS distribution is boundless. The return level plots in Fig. 7.8 exemplify this disparity. It is interesting to note that the 10th-observation return level X_{10} for the TRS distribution exceeds the upper bound of the LRS distribution. In fact, ~22 % of inclusions in the TRS

material are expected to be larger than the largest inclusion in the LRS material (the return period m associated with X_m =0.49 mm is ~4.5 for the TRS distribution).

Table 7.1 GP parameters used to model the upper tail of the inclusion size distributions shown in Fig.7.3(c). ξ, $\tilde{\sigma}$, u, and X_{10} denote the shape parameter, scale parameter, threshold value, and 10th-observation return level, respectively.

	ξ–mean	ξ– 95 % Confidence Intervals	$\tilde{\sigma}$	u	X_{10} *(mm)*
TRS	-0.032	[-0.169; 0.106]	0.064	0.406	0.548
LRS	-0.132	[-0.276; 0.012]	0.031	0.214	0.290

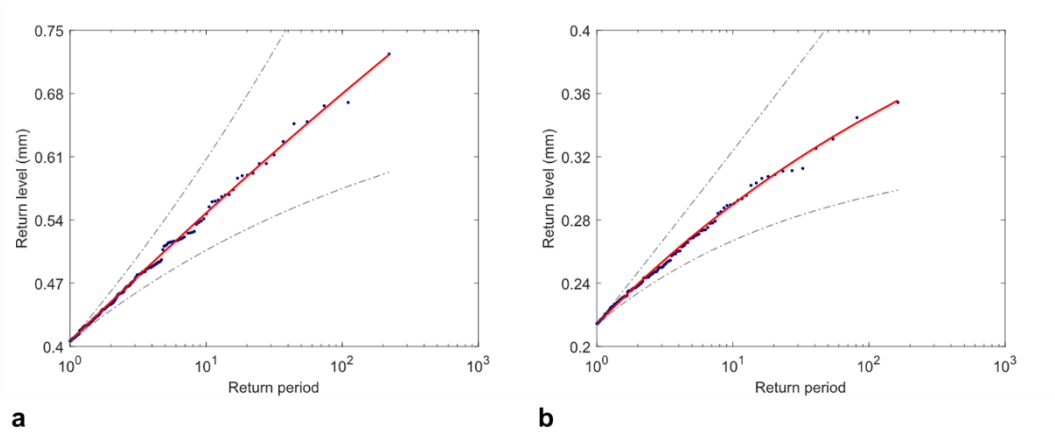

Fig. 7.8 GP distributions (solid line) fitted to the (a) TRS and (b) LRS inclusion size distributions shown in Fig. 7.3(c). Shown are the m^{th}-observation return levels X_m associated with a return period m. The dashed lines represent 95 % confidence intervals. For comparison, the experimental data points are plotted in ascending order. Note: the scale of the ordinate differs in (a) and (b).

7.4.3 Porosity

GP distributions were fitted to the pore size distributions shown in Fig. 7.4(c). Parameter estimates for the fitted distributions are provided in Table 7.2; return level plots are shown in Fig. 7.9. Although the threshold values u are relatively similar, differences between the two distributions become more apparent as m increases (as illustrated by the values of X_{10}). Suppose these pores originate from gaseous sources, as per Section 7.3.3. It follows that the flow constriction in the LRS leads to an increase in pore size. Several researchers [4,21] assert the contrary, i.e. increased melt velocities lead to a decrease in pore size via the breakup of gaseous phases; however, these assertions assume that most of the gas bubbles are introduced prior to die filling. When a bubble is placed in a turbulent flow, it oscillates and deforms due to fluctuations of the local pressure

gradient. Breakage will occur when the kinetic energy transmitted by a turbulent oscillation is greater than the surface energy of the bubble [29]. Although the flow buffer employed in the LRS casting (Fig. 7.1(d)) aims to reduce turbulence just downstream of the orifice, an appreciable increase in ε is observed in the gauge length of the tensile specimens (Fig. 7.6). It is possible that either this ε is less than the critical value ε_{crit} required for breakage, or that the filling times involved in HPDC (10~100 ms [30]) are too small to facilitate breakage inside the cavity. When $\varepsilon < \varepsilon_{crit}$, or when the particle residence time is too short, turbulence is expected to promote air entrapment and bubble coalescence, leading to an increase in pore size.

Table 7.2 GP parameter estimates used to model the tails of the pore size distributions shown in Fig. 7.4(c). ξ, $\tilde{\sigma}$, u, and X_{10} denote the shape parameter, scale parameter, threshold value and the 10th-observation return level, respectively.

	ξ–mean	ξ– 95 % Confidence Intervals	$\tilde{\sigma}$	u	X_{10} *(mm)*
TRS	0.103	[-0.074; 0.279]	0.017	0.109	0.166
LRS	-0.063	[-0.149; 0.024]	0.050	0.125	0.233

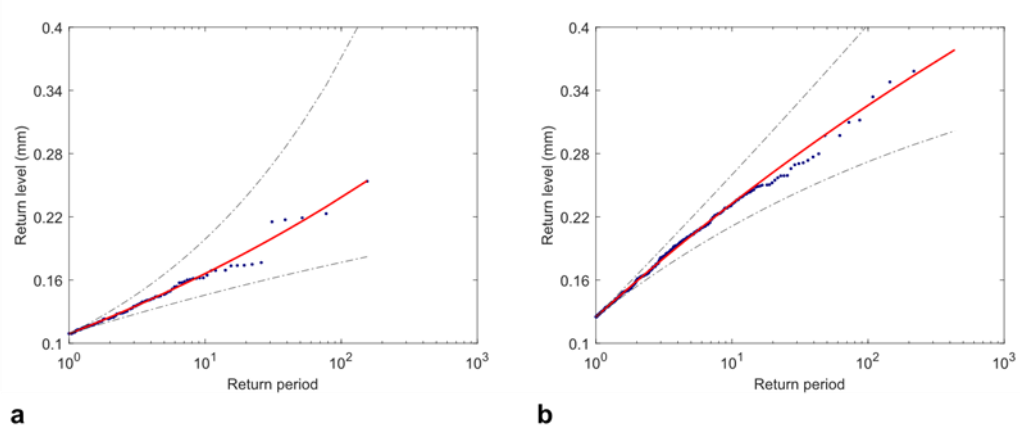

Fig. 7.9 GP distributions (solid line) fitted to the (a) TRS and (b) LRS pore size distributions shown in Fig. 7.4(c). Shown are the m^{th}-observation return levels X_m associated with a return period m. The dashed lines represent 95 % confidence intervals. For comparison, experimental data points are plotted in ascending order.

7.4.4 Improvement in Mechanical Properties

Significant improvements in tensile strength and ductility were obtained by promoting turbulence in the runner system—but what causes this improvement? Few oxides were observed on the fracture surface of the tensile specimens, and when they were observed they were relatively small in size.

Considering the return levels X_{10} obtained from the extreme value analysis, an increase in ε is accompanied by a significant decrease in inclusion size and a moderate increase in pore size. Additionally, in both materials the value of X_{10} obtained for the inclusion size distribution exceeds that obtained for the pore size distribution. This suggests that the observed improvement in tensile strength and tensile ductility is attributed to a refinement of large inclusions in the LRS.

7.4.5 Gaussian Mixture Models

Next, we discuss the mechanism by which inclusions are refined in the LRS. We begin by deducing the species of inclusions contained in the X-ray tomography data sets. The size and morphology of an inclusion will vary depending on the local thermal and hydrodynamic conditions. In an unstirred melt, these features will fluctuate about some mean value unique to that species of inclusion. As ε increases, it is suspected that breakage will induce both refinement and morphological change, i.e. inclusions will become smaller in size and more compact in morphology.

Clustering is a canonical problem in machine learning, in which query data is partitioned into groups, or clusters, based on similitude. In a Gaussian mixture model (GMM), clusters are modelled as a mixture of normal density components. The mixture density function is given by a weighted linear combination of the k-component densities [31]:

$$F(x) = \sum_{i=1}^{k} \alpha_i f(x\,|\mu_i, \Sigma_i),$$
$$f(x\,|\mu_i, \Sigma_i) = \frac{1}{\sqrt{(2\pi)^n |\Sigma_i|}} \exp\left(-\frac{1}{2}(x-\mu_i)^T {\Sigma_i}^{-1}(x-\mu_i)\right),$$
$$\sum_{i=1}^{k} \alpha_i = 1 \qquad \textbf{(7.2)}$$

where x is our n-dimensional feature vector and $\{\alpha_i, \mu_i, \Sigma_i\}$ denote the mixture weight, mean vector and covariance matrix associated with each component density $f(x\,|\mu_i, \Sigma_i)$, respectively.

Multivariate GMMs were fitted to the inclusion populations discussed in Section 7.3.2. A three-dimensional feature vector x was defined, with each row containing values for the diameter (*D*), compactness and mean grey value of a given inclusion; the mean grey value represents the attenuation of the X-ray beam averaged over all voxels of the inclusion. Parameter estimates for the GMM were obtained by expectation-maximization using the Statistics and Machine Learning Toolbox™ in MATLAB. Values of k were determined empirically using the Akaike information criterion (AIC) and the Bayesian information criterion (BIC). Estimated AIC and BIC for the two inclusion populations are shown in Fig. 7.10 and support the case of $k = 3$. In Fig. 7.11 each

inclusion is assigned to one of three clusters according to its posterior probabilities, i.e. the probability that the data point belongs to a given cluster. Each mixture component is equivalent to a three-dimensional normal distribution with mean vector μ_i and covariance matrix Σ_i, which may be visualised as an ellipsoid.

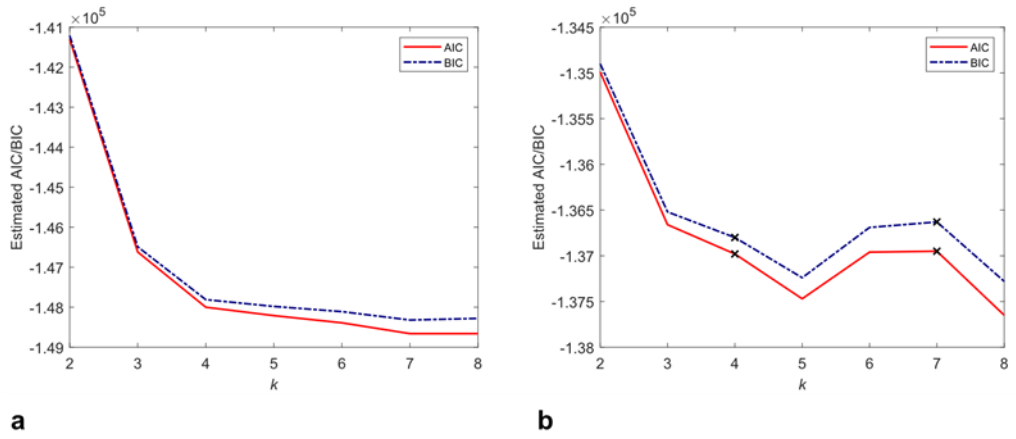

Fig. 7.10 Estimated AIC and BIC for multivariate GMMs (*k* = 2,3,…8) fitted to X-ray tomography data obtained for (a) the TRS sample and (b) the LRS sample. A cross indicates that the expectation-maximization algorithm failed to converge within 1000 iterations. A value of *k* = 3 was selected to prevent overfitting.

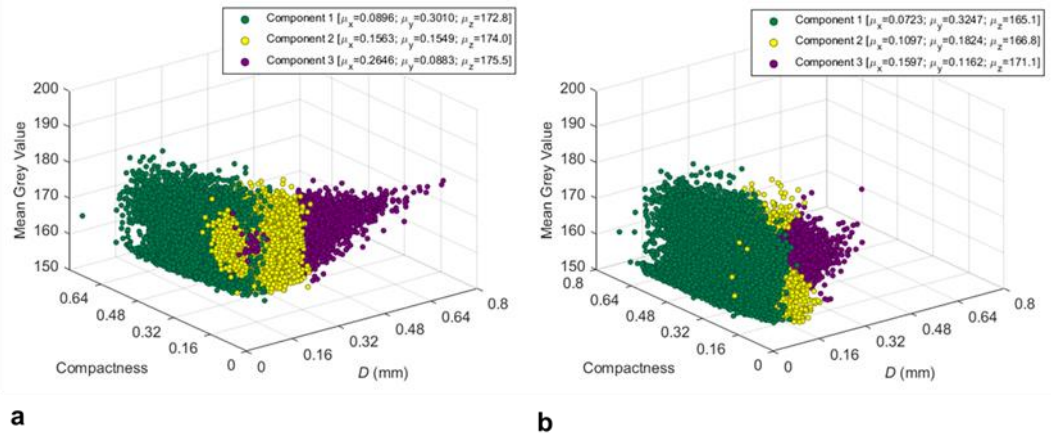

Fig. 7.11 Multivariate GMMs (*k*=3) fitted to X-ray tomography data obtained for (a) the TRS sample, and (b) the LRS sample. The *x*, *y*, and *z* axes represent the diameter (*D)*, compactness, and mean grey value of each inclusion identified by the VGDEFX algorithm.

7.4.6 Species of Inclusions

So far, we have partitioned inclusions into three clusters based on their size, shape and attenuating behaviour. The question we wish to address is: what species of inclusions do these clusters represent? Consider the mean vector of each component in the TRS mixture model: $\mu_1 = [0.0896\ \text{mm}, 0.3010, 172.8]$, $\mu_2 = [0.1563\ \text{mm}, 0.1549, 174.0]$, and $\mu_3 = [0.2646\ \text{mm}, 0.0883, 175.5]$. Candidate inclusions must be of a comparable size to the mean diameter μ_x of the cluster; the morphology of these inclusions must also relate to the mean compactness μ_y of the cluster. Additionally, there must be enough atomic contrast between the inclusion and Al-matrix to produce a detectable increase in X-ray attenuation. The phase diagram (Fig. 7.12) presents two intermetallic phases as candidates: α-$Al_{15}(FeMn)_3Si_2$ and β-AlFeSi. In HPDC, two-types of α-$Al_{15}(FeMn)_3Si_2$ phase precipitate during solidification: primary α-$Al_{15}(FeMn)_3Si_2$ phase forms in the shot chamber, exhibiting a polyhedral/Chinese script morphology ($20{\sim}100\ \mu\text{m}$ [32]); proeutectic α-$Al_{15}(FeMn)_3Si_2$ phase forms in the die cavity, exhibiting a compact polyhedral morphology ($3{\sim}20\ \mu\text{m}$ [32]). The appreciable difference in size is due to the high cooling rates in the die cavity ($500{\sim}1000\ \text{Ks}^{-1}$ [33]) compared to that in the shot chamber ($\sim 10\ \text{Ks}^{-1}$ [34]). Clearly, the proeutectic α-$Al_{15}(FeMn)_3Si_2$ phase is outside the spatial resolution of the X-ray tomography scan. Furthermore, β-AlFeSi phases are rarely observed in the two materials (Fig. 7.13): this is attributed to the addition of Mn which acts to suppress the formation of β-AlFeSi [35].

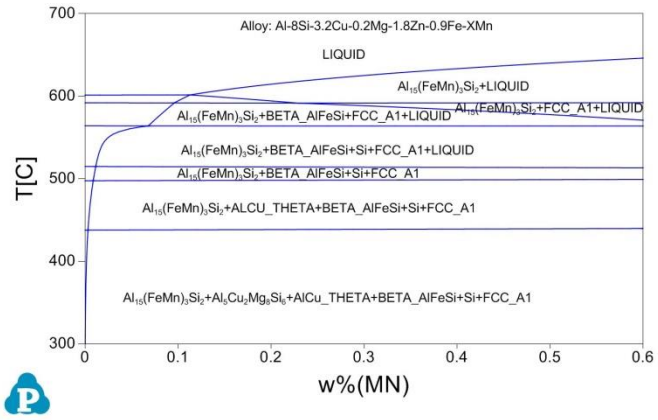

Fig. 7.12 Phase diagram for HPDC LM24 alloy produced in PANDAT (CompuTherm LLC) using the PanAl2020 database (CompuTherm LLC) under equilibrium solidification conditions. Phase diagram courtesy of Dr. Feng Gao.

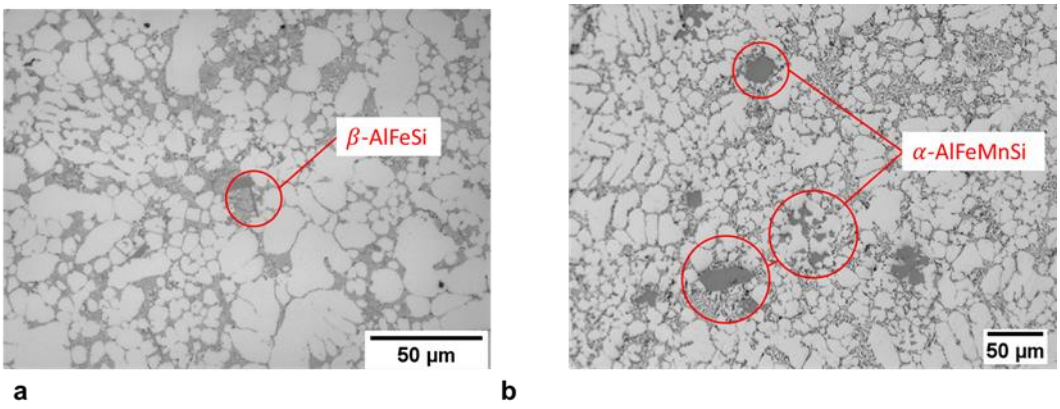

Fig. 7.13 Optical micrographs highlighting (a) β-AlFeSi phase, and (b) α-AlFeMnSi phases. Note that the distinction between β-AlFeSi and α-AlFeMnSi phases are based solely on the morphology of the intermetallic compounds and prior knowledge of the alloy system.

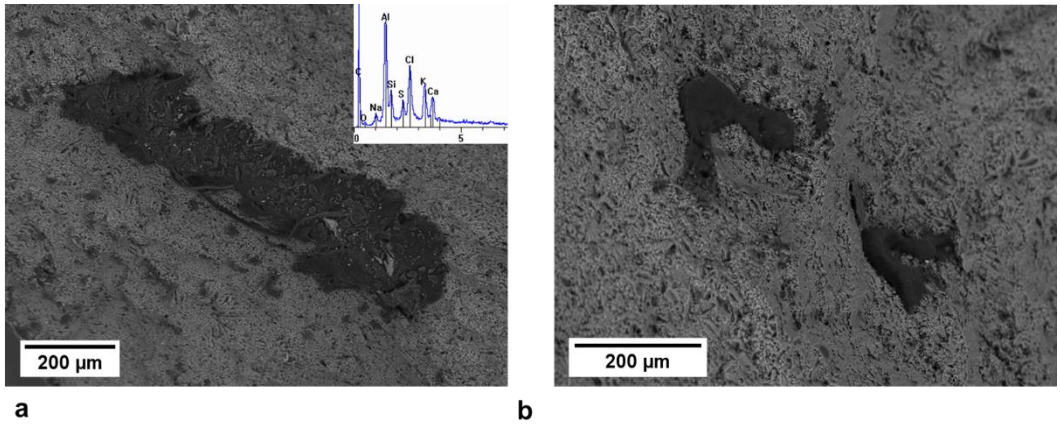

Fig. 7.14 BSE micrographs of non-metallic inclusions observed on the fracture surface of tensile specimens from the TRS group. (a) large inclusion with irregular morphology. (b) fine, compact inclusions. The insert in (a) shows a representative EDX spectrum for these non-metallic inclusions.

Large non-metallic inclusions are also present in both materials; representative micrographs of these inclusions are shown in Fig. 7.14. We discuss the origin of these non-metallic inclusions in Chapter 6. EDX analysis revealed that these inclusions typically contain C, S, Cl, K, and Ca—the latter two elements are of interest, as they fulfil the atomic contrast requirement for X-ray tomography. The fact that these inclusions contain K and Ca does not necessarily mean that they will be more attenuating than the aforementioned Fe-rich phases, particularly if these elements are diffusively distributed throughout the inclusion, or if the inclusions possess a film-like morphology. Comparing the mean grey values of each cluster, inclusions in Component-2 (174.0) and Component-3 (175.5) are, on average, more attenuating than those in Component-1 (172.8). However, a more notable difference lies in the spread of the mean grey values within each cluster. For example, Component-1 and Component-2 both exhibit a wide range of mean grey values $(150\sim180)$ within a relatively

small size interval ($100{\sim}300\ \mu m$). Conversely, inclusions in Component-3 appear to attenuate in a more consistent manner, with the mean grey value observed to increase with an increase in inclusion size. This suggests that Component-3 represents a single species of inclusion, while Component-1 and Component-2 comprise a mixture of non-metallic inclusions and intermetallic phases.

7.4.7 Influence of ε on Breakage

Previously, we narrowed our candidate inclusions down to primary α-$Al_{15}(FeMn)_3Si_2$ phase, β-AlFeSi phase, and non-metallic inclusions. Fig. 7.14 shows that these non-metallic inclusions vary significantly in both size ($10{\sim}800\ \mu m$) and morphology (compact to highly irregular). Since high levels of ε are attained in both dies, breakage should be evidenced in both materials. From Section 7.4.6, we deduce that Component-3 is composed entirely of large non-metallic inclusions. Additionally, we infer that Component-1 consists of primary α-$Al_{15}(FeMn)_3Si_2$ phase solidified in the shot chamber and fine non-metallic inclusions. Component-2 is expected to comprise a mixture of fragmented non-metallic inclusions and β-AlFeSi phases. Comparing the mean vectors of the two mixture models (Fig. 7.11), the LRS is shown to produce a significant decrease in the mean diameter μ_x and an increase in the mean compactness μ_y of all three clusters—an effect which is most notable in Component-3. Additionally, the probability density contours in Fig. 7.15 show that the peaks of the LRS mixture model also move towards a region of higher compactness and lower diameter compared to the TRS model. In fact, the number fraction of inclusions in Component-1 of the LRS mixture model (0.65) is approximately double that of the TRS mixture model (0.32).

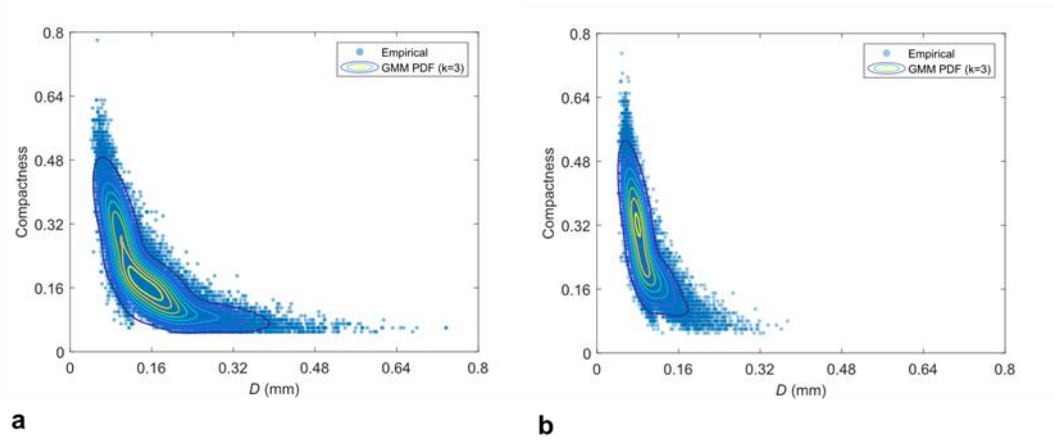

Fig. 7.15 Multivariate GMMs (*k*=3) fitted to X-ray tomography data obtained for (a) the TRS sample, and (b) the LRS sample. Shown is a projection of the three-dimensional model shown in Fig. 7.11 with superimposed probability density contours.

Thus, increasing ε and/or the particle residence time leads to a significant refinement of non-metallic inclusions and the production of small, compact particles. Since solidification conditions in the shot chamber were closely monitored, it is proposed that the production of fines is attributed to the breakup of non-metallic inclusions. This supposition is supported by the mean grey values observed in Component-1 (Fig. 7.11): while the number of inclusions with mean grey values in the range of $150{\sim}160$ remains relatively constant, an increase in ε is accompanied by a significant increase in the number of inclusions with mean grey values in the range of $160{\sim}180$. It is proposed that these non-metallic inclusions fragment in a manner that is analogous to the breakage of solid aggregates [15,17] and highly viscous droplets [20] suspended in a turbulent flow.

7.4.8 Crystal Fragmentation

There is a growing consensus that grain size distributions in HPDC microstructures are bimodal, i.e. they comprise a mixture of large dendritic α-Al_1 grains (30∼300 μm [36,37]) solidified in the shot chamber, and small globular-rosette α-Al_2 grains (∼10 μm [36,37]) solidified in the die cavity. Conversely, it is generally accepted that agitation of the liquid during solidification causes dendrite fragmentation, which leads to grain refinement and morphological change [38–42]. It has been suggested [22] that intensive shearing of the liquid during die filling expedites the fragmentation of primary α-Al_1 crystals, leading to a high density of solid fragments in the liquid. If this is indeed the case, then surely grain size distributions in HPDC microstructures should be trimodal, rather than bimodal—they should comprise a mixture of primary α-Al_1 grains, primary α-Al_2 grains, and the fragmented dendrite arms of primary α-Al_1 crystals. This postulate forms the basis of the following discussion.

Fig. 7.16 presents grain size distributions corresponding to the IPF maps shown in Fig. 7.5. Grain size distributions are often observed to approximate a lognormal shape—a phenomenon which has previously been attributed to the time-dependent kinetics of random nucleation and growth processes [43]. Accordingly, the grain size distributions in Fig. 7.16 are presented on a logarithmic scale (i.e. $x = \ln D$, where D is the maximum Feret diameter). Clearly, the grain size distributions are multimodal—an observation which is more pronounced in the TRS distribution than in the LRS distribution. Univariate GMMs were fitted to the two grain size distributions to identify subpopulations within each data set. Estimated AIC and BIC are shown Fig. 7.17, and support the case of $k = 3$, indicating that both grain size distributions are trimodal. Although the flow field intensity appears to have a negligible influence on μ_1, an increase in ε is shown to produce a significant decrease in μ_3 (from 33.2 μm to 17.1 μm) and a modest decrease in μ_2 (from 12.5 μm to 8.8 μm). Additionally, the number fraction of grains in Component-2 increases from 0.45 (TRS) to 0.70 (LRS). This may be interpreted as the fragmentation of large primary α-Al_1 grains (μ_3) into more,

smaller crystals (μ_2); in this framework μ_1 represents primary α-Al_2 grains solidified in the die cavity. The observed refinement of μ_1 and μ_2 may be explained by considering the liquid temperature at the end of die filling (Fig. 7.7): higher cooling rates are attained in the LRS geometry than in the TRS geometry, which may further inhibit the growth of both primary α-Al_2 grains and fragmented α-Al_1 crystals.

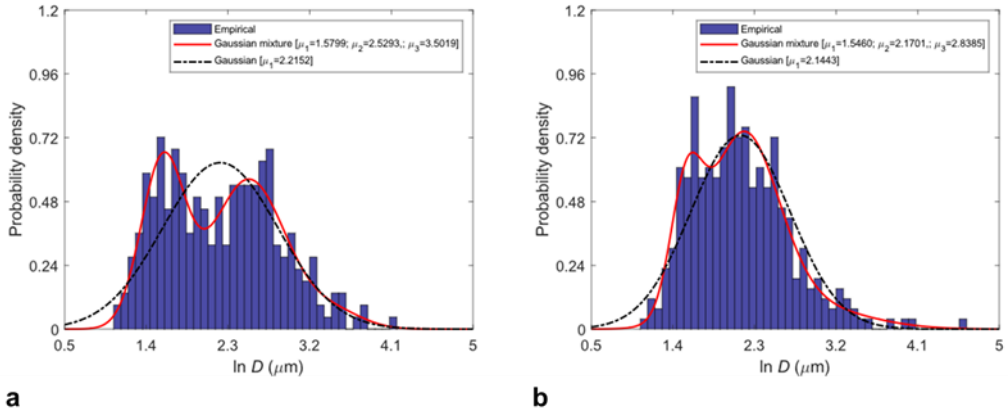

Fig. 7.16 Univariate Gaussian mixture models (*k*=3) fitted to grain size distributions corresponding to (a) the TRS sample, and (b) the LRS sample; for comparison, a unimodal Gaussian is also shown. Grain size is presented as the natural logarithm of the maximum Feret diameter (i.e. ln *D*).

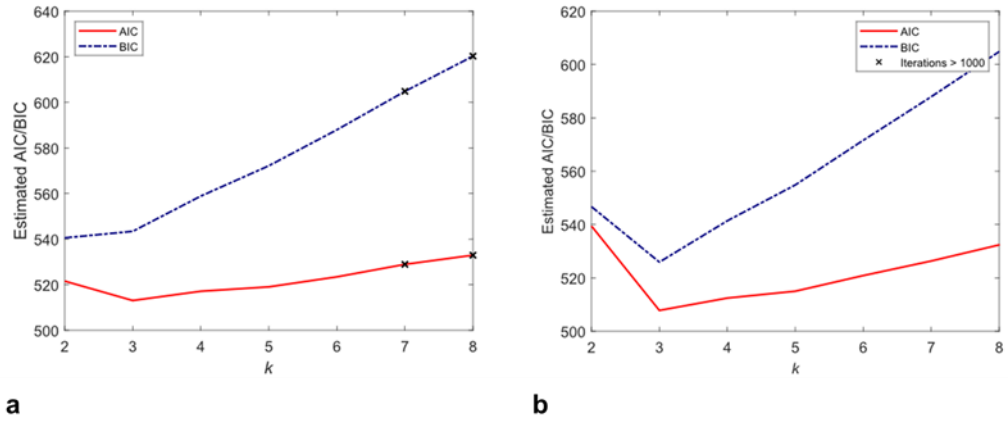

Fig. 7.17 Estimated AIC/BIC for unimodal GMMs (*k* = 2,3,…,8) fitted to grain size distributions obtained for the (a) TRS and (b) LRS samples. A cross indicates that the expectation-maximization algorithm failed to converge within 1000 iterations. A value of *k* = 3 was selected corresponding to distinct minimums in AIC and BIC.

We may divide dendrite fragmentation mechanisms into two broad classes, depending on the driving force for breakage: those that rely on direct mechanical action of the hydrodynamic field to induce plastic bending and subsequent fragmentation [38,39]; and those that depend on the induced movement of solute-rich liquid to destabilise the solid relative to the liquid [41,44]. Although there is compelling experimental evidence that primary α-Al_1 crystals bend plastically during HPDC [36], this is not necessarily evidence for a mechanical mode of breakage—how can we ascertain that crystal bending occurs prior to breakage, as opposed to during the intensification stage, when the solidifying alloy undergoes shear deformation with large compressive stresses? Previous studies based on synchrotron X-ray imaging [44] have demonstrated that the flow of inter-dendritic liquid may destabilise the local temperature-concentration-curvature equilibrium, leading to dendrite root remelting. Adopting this framework, turbulent oscillations of the surrounding liquid would cause the local thermal and constitutional conditions to fluctuate intermittently, which may expedite the remelting process—the time scale of turbulence is likely to be smaller than that required for both thermal and constitutional equilibration.

7.5 Summary

1. Adopting a lean runner system can lead to significant improvements in both tensile strength (mean: +17 %) and tensile ductility (mean: +35 %). This improvement is attributed to a refinement of large non-metallic inclusions that originate from the pyrolysis of commercial plunger lubricants.
2. X-ray tomography and machine learning are used to identify species of inclusions contained in HPDC samples produced with different flow field intensities. At high levels of ε, large non-metallic inclusions are broken down into more, smaller particles with a compact morphology. It is proposed that breakage occurs in a manner analogous to the rupture of colloidal aggregates and highly viscous droplets suspended in a turbulent flow.
3. Under the observed experimental conditions, grain size distributions in HPDC microstructures are shown to be trimodal: they comprise a mixture of primary α-Al_1 grains formed in the shot chamber, primary α-Al_2 grains formed in the die cavity, and the fragmented dendrite arms of primary α-Al_1 grains. Several fragmentation mechanisms are discussed, with a particular emphasis on the role of fluid turbulence.

7.6 References

[1] S. Wang, Y. Wang, Q. Ramasse, Z. Fan, The Nature of Native MGO in Mg and its Alloys, Metall. Mater. Trans. A. 51 (2020) 2957–2974. https://doi.org/10.1007/s11661-020-05740-1.

[2] G.S.B. Lebon, H.-T. Li, J.B. Patel, H. Assadi, Z. Fan, Numerical Modelling of Melt-Conditioned Direct-Chill Casting, Appl. Math. Model. 77 (2020) 1310–1330. https://doi.org/10.1016/j.apm.2019.08.032.

[3] E. Lordan, J. Lazaro-Nebreda, Y. Zhang, Z. Fan, Effective Degassing for Reduced Variability in High-Pressure Die Casting Performance, JOM. 71 (2019) 824–830. https://doi.org/10.1007/s11837-018-3186-4.

[4] E. Koya, M. Nakagawa, S. Kitagawa, J. Ishimoto, Y. Nakano, N. Ochiai, Research of Atomization Phenomena in HPDC-Step 1 Feature of Gas Porosity Dispersion and Photography of Atomized Flow, in: 2018: pp. 2018-01–1392. https://doi.org/10.4271/2018-01-1392.

[5] C. Tian, J. Law, J. van der Touw, M. Murray, J.-Y. Yao, D. Graham, D. St. John, Effect of Melt Cleanliness on the Formation of Porosity Defects in Automotive Aluminium High Pressure Die Castings, J. Mater. Process. Technol. 122 (2002) 82–93. https://doi.org/10.1016/S0924-0136(01)01229-8.

[6] E. Lordan, J. Lazaro-Nebreda, Y. Zhang, K. Dou, P. Blake, Z. Fan, On the Relationship Between Internal Porosity and the Tensile Ductility of Aluminium Alloy Die-Castings, Mater. Sci. Eng.: A 778 (2020) 139107. https://doi.org/10.1016/j.msea.2020.139107.

[7] S. Ji, W. Yang, B. Jiang, J.B. Patel, Z. Fan, Weibull Statistical Analysis of the Effect of Melt Conditioning on the Mechanical Properties of AM60 Alloy, Mater. Sci. Eng.: A 566 (2013) 119–125. https://doi.org/10.1016/j.msea.2012.12.079.

[8] Y. Zhang, J.B. Patel, J. Lazaro-Nebreda, Z. Fan, Improved Defect Control and Mechanical Property Variation in High-Pressure Die Casting of A380 Alloy by High Shear Melt Conditioning, JOM. 70 (2018) 2726–2730. https://doi.org/10.1007/s11837-018-3005-y.

[9] D.G. Eskin, I. Tzanakis, F. Wang, G.S.B. Lebon, T. Subroto, K. Pericleous, J. Mi, Fundamental Studies of Ultrasonic Melt Processing, Ultrason. Sonochem. 52 (2019) 455–467. https://doi.org/10.1016/j.ultsonch.2018.12.028.

[10] N. Gül Özcan-Taşkın, G.A. Padron, D. Kubicki, Comparative Performance of In-Line Rotor-Stators for Deagglomeration Processes, Chem. Eng. Sci. 156 (2016) 186–196. https://doi.org/10.1016/j.ces.2016.09.023.

[11] C.M. Gourlay, H.I. Laukli, A.K. Dahle, Defect Band Characteristics in Mg-Al and Al-Si High-Pressure Die Castings, Metall. Mater. Trans. A 38 (2007) 1833–1844. https://doi.org/10.1007/s11661-007-9243-1.

[12] X.P. Niu, K.K. Tong, B.H. Hu, I. Pinwill, Cavity Pressure Sensor Study of the Gate Freezing Behaviour in Aluminium High Pressure Die Casting, Int. J. Cast Met. Res. 11 (1998) 105–112. https://doi.org/10.1080/13640461.1998.11819264.

[13] M.U. Bäbler, M. Morbidelli, J. Bałdyga, Modelling the Breakup of Solid Aggregates in Turbulent Flows, J. Fluid Mech. 612 (2008) 261–289. https://doi.org/10.1017/S002211200800298X.

[14] J. De Bona, A.S. Lanotte, M. Vanni, Internal Stresses and Breakup of Rigid Isostatic Aggregates in Homogeneous and Isotropic Turbulence, J. Fluid Mech. 755 (2014) 365–396. https://doi.org/10.1017/jfm.2014.421.

[15] V. Becker, E. Schlauch, M. Behr, H. Briesen, Restructuring of Colloidal Aggregates in Shear Flows and Limitations of the Free-Draining Approximation, J. Colloid Interface Sci. 339 (2009) 362–372. https://doi.org/10.1016/j.jcis.2009.07.022.

[16] S. Blaser, Break-Up of Flocs in Contraction and Swirling Flows, Colloids Surf. Physicochem. Eng. Asp. 166 (2000) 215–223. https://doi.org/10.1016/S0927-7757(99)00450-1.

[17] K. Higashitani, K. Iimura, H. Sanda, Simulation of Deformation and Breakup of Large Aggregates in Flows of Viscous Fluids, Chem. Eng. Sci. 56 (2001) 2927–2938. https://doi.org/10.1016/S0009-2509(00)00477-2.

[18] N. Zumaeta, E.P. Byrne, J.J. Fitzpatrick, Breakage of Protein Precipitates Flowing Through Orifices, Chem. Eng. Res. Des. 86 (2008) 107–117. https://doi.org/10.1016/j.cherd.2007.10.017.

[19] N. Zumaeta, G.M. Cartland-Glover, S.P. Heffernan, E.P. Byrne, J.J. Fitzpatrick, Breakage Model Development and Application with CFD for Predicting Breakage of Whey Protein Precipitate Particles, Chem. Eng. Sci. 60 (2005) 3443–3452. https://doi.org/10.1016/j.ces.2005.02.016.

[20] R. Sanjuan-Galindo, E. Soto, R. Zenit, G. Ascanio, Viscous Filament Fragmentation in a Turbulent Flow Inside a Stirred Tank, Chem. Eng. Commun. 202 (2015) 1251–1260. https://doi.org/10.1080/00986445.2014.923994.

[21] D.R. Gunasegaram, M. Givord, R.G. O'Donnell, B.R. Finnin, Improvements Engineered in UTS and Elongation of Aluminum Alloy High Pressure Die Castings Through the Alteration of Runner Geometry and Plunger Velocity, Mater. Sci. Eng.: A 559 (2013) 276–286. https://doi.org/10.1016/j.msea.2012.08.098.

[22] M. Wu, X. Li, Z. Guo, S. Xiong, Effects of Process Parameters on Morphology and Distribution of Externally Solidified Crystals in Microstructure of Magnesium Alloy Die Castings, China Foundry. 15 (2018) 139–144. https://doi.org/10.1007/s41230-018-7242-z.

[23] ASTM Committee, Standard Test Methods for Tension Testing of Metallic Materials, 2003.

[24] K. Dou, E. Lordan, Y.J. Zhang, A. Jacot, Z.Y. Fan, Numerical Simulation of Fluid Flow, Solidification and Defects in High Pressure Die Casting (HPDC) process, IOP Conf. Ser. Mater. Sci. Eng. 529 (2019) 012058. https://doi.org/10.1088/1757-899X/529/1/012058.

[25] S.E. Elghobashi, T.W. Abou-Arab, A Two-Equation Turbulence Model for Two-Phase Flows, Phys. Fluids. 26 (1983) 931–938. https://doi.org/10.1063/1.864243.

[26] A. Vakhrushev, A. Ludwig, Menghuai Wu, Y. Tnag, G. Nitzl, G. Hackl, Modelling of Turbulent Melt Flow and Solidification Processes in Steel Continuous Caster with the Open Source Software Package OpenFOAM, (2010). https://doi.org/10.13140/RG.2.1.1452.9123.

[27] O. Koser, J. Ruckert, P. Ubl, Modelling and Optimization of Part Ejection in Magnesium High Pressure Die Casting, Euro. Metall. Conf., 2015, 371-382, Düsseldorf, Germany.

[28] M. Saeedipour, S. Schneiderbauer, S. Pirker, S. Bozorg, A Numerical and Experimental Study of Flow Behavior in High Pressure Die Casting, Magnesium Tech. 2014, 185–190. https://doi.org/10.1007/978-3-319-48231-6_37.

[29] Y. Liao, D. Lucas, A Literature Review of Theoretical Models for Drop and Bubble Breakup in Turbulent Dispersions, Chem. Eng. Sci. 64 (2009) 3389–3406. https://doi.org/10.1016/j.ces.2009.04.026.

[30] P.K. Mallick, Materials, Design and Manufacturing for Lightweight Vehicles, Woodhead Publishing, 2010. https://www.sciencedirect.com/book/9781845694630/materials-design-and-manufacturing-for-lightweight-vehicles.

[31] J. McGonagle, G. Pilling, A. Dobre, V. Tembo, A. Kurmukov, E.R. Chumbley, Gaussian Mixture Model, https://brilliant.org/wiki/gaussian-mixture-model/ (accessed June 17, 2020).

[32] Y. Zhang, S. Wang, E. Lordan, Y. Wang, Z. Fan, Improve Mechanical Properties of High Pressure Die Cast Al9Si3Cu Alloy via Dislocation Enhanced Precipitation, J. Alloys Compd. 785 (2019) 1015–1022. https://doi.org/10.1016/j.jallcom.2019.01.278.

[33] H. Gjestland, S. Sannes, J. Svalestuen, H. Westengen, Optimizing the Magnesium Die Casting Process to Achieve Reliability in Automotive Applications, SAE Trans. 114 (2005) 67–73.

[34] ASTM Committee, Magnesium and Magnesium Alloys, ASM International, 1999.

[35] S. Ji, W. Yang, F. Gao, D. Watson, Z. Fan, Effect of Iron on the Microstructure and Mechanical Property of Al–Mg–Si–Mn And Al–Mg–Si Diecast Alloys, Mater. Sci. Eng.: A 564 (2013) 130–139. https://doi.org/10.1016/j.msea.2012.11.095.

[36] S. Otarawanna, C.M. Gourlay, H.I. Laukli, A.K. Dahle, Agglomeration and Bending of Equiaxed Crystals During Solidification of Hypoeutectic Al and Mg Alloys, Acta Mater. 58 (2010) 261–271. https://doi.org/10.1016/j.actamat.2009.09.002.

[37] S. Otarawanna, C.M. Gourlay, H.I. Laukli, A.K. Dahle, Microstructure Formation in AlSi4MgMn and AlMg5Si2Mn High-Pressure Die Castings, Metall. Mater. Trans. A 40 (2009) 1645–1659. https://doi.org/10.1007/s11661-009-9841-1.

[38] R.D. Doherty, H.-I. Lee, E.A. Feest, Microstructure of Stir-Cast Metals, Mater. Sci. Eng. 65 (1984) 181–189. https://doi.org/10.1016/0025-5416(84)90211-8.

[39] A. Vogel, Turbulent Flow and Solidification: Stir-Cast Microstructure, Met. Sci. 12 (1978) 576–578. https://doi.org/10.1179/msc.1978.12.12.576.

[40] R.H. Mathiesen, L. Arnberg, P. Bleuet, A. Somogyi, Crystal Fragmentation and Columnar-to-Equiaxed Transitions in Al-Cu Studied by Synchrotron X-ray Video Microscopy, Metall. Mater. Trans. A. 37 (2006) 2515–2524. https://doi.org/10.1007/BF02586224.

[41] D. Ruvalcaba, R.H. Mathiesen, D.G. Eskin, L. Arnberg, L. Katgerman, In Situ Observations of Dendritic Fragmentation due to Local Solute-Enrichment During Directional Solidification of an Aluminum Alloy, Acta Mater. 55 (2007) 4287–4292. https://doi.org/10.1016/j.actamat.2007.03.030.

[42] D. Shu, B. Sun, J. Mi, P.S. Grant, A High-Speed Imaging and Modeling Study of Dendrite Fragmentation Caused by Ultrasonic Cavitation, Metall. Mater. Trans. A. 43 (2012) 3755–3766. https://doi.org/10.1007/s11661-012-1188-3.

[43] R.B. Bergmann, A. Bill, On the Origin of Logarithmic-Normal Distributions: an Analytical Derivation, and its Application to Nucleation and Growth Processes, J. Cryst. Growth. 310 (2008) 3135–3138. https://doi.org/10.1016/j.jcrysgro.2008.03.034.

[44] E. Liotti, A. Lui, R. Vincent, S. Kumar, Z. Guo, T. Connolley, I.P. Dolbnya, M. Hart, L. Arnberg, R.H. Mathiesen, P.S. Grant, A Synchrotron X-Ray Radiography Study of Dendrite Fragmentation Induced by a Pulsed Electromagnetic Field in an Al–15Cu Alloy, Acta Mater. 70 (2014) 228–239. https://doi.org/10.1016/j.actamat.2014.02.024.

Chapter 8: On the Relationship Between Internal Porosity and the Tensile Ductility of Aluminium Alloy Die-Castings

8.1 Introduction

Previously, we identified porosity as one of the dominant sources of variability in tensile ductility, for die-castings produced under Baseline conditions (Chapter 6). Although we can reduce porosity by adjusting the kinematics of the plunger (Chapter 6), we cannot eliminate it completely. For the purpose of cost reduction and part consolidation, die-castings typically exhibit a high degree of geometric complexity, which results in a certain amount of porosity that is practically unavoidable in normal industrial castings [1–3]. As the dominant ductility limiting factor in hypoeutectic Al-Si-Mg alloys, porosity presents a major obstacle to the more widespread use of aluminium castings within the automotive industry, often responsible for the conservative safety coefficients used in component design [4]. To address this issue, further understanding is required before a quantitative relationship may be established between the casting integrity and the materials performance in tensile and fatigue.

By performing three-dimensional in-situ tensile and fatigue tests using X-ray tomography and digital volume correlation, several studies have revealed the damage mechanisms of hypoeutectic Al-Si alloys [4–13]. It is widely accepted, that damage originates at various microstructural heterogeneities including eutectic Si particles and intermetallic phases. The nucleation of voids from these hard inclusions occurs by decohesion of the particle-matrix interface or by particle fracture, with the subsequent growth and coalescence of voids forming large cracks in the Al matrix [14]. By reducing the load-bearing area and localising strain, pores provide preferential crack initiation sites and accelerate the production of damage [1,2,10]. While there exists little to no correlation between the bulk porosity content and the reduction in tensile properties, the ductility and tensile strength are reported to decrease monotonically with an increase in the areal fraction of porosity observed on the fracture surface [1,2,15–18]. Accordingly, several researchers have attempted to relate the failure of die-cast metals to some measure of the areal fraction of porosity; whether determined by non-destructive evaluation or by coupling quantitative fractography with extreme value statistics [1,2,18–22].

A tensile failure model, first presented by Ghosh and later developed by Cáceres and Selling, approximates the effects of multiple voids (A_i) as a single geometric imperfection of equivalent area ($A_v = \sum A_i$), located at the centre of an otherwise perfect specimen [1,2,23]. The geometry assumed in this model is illustrated in Fig. 8.1(i). Under uniaxial tension, the defective region yields first as a consequence of the reduced load-bearing area. The subsequent localisation of plastic flow results in the formation of an incipient neck around the local inhomogeneity. Following Ghosh's model for the loss of mechanical stability in a deforming body, the rate of strain concentration can be described

considering the strain hardening ability of the material [23]. For a sample of initial cross-sectional area A_o containing an imperfection of areal fraction $f = A_v/A_o$, axial load equilibrium requires:

$$\sigma_v(1-f)A_o \exp(-\varepsilon_v) = \sigma_h A_o \exp(-\varepsilon_h) \tag{8.1}$$

where σ_v, ε_v and σ_h, ε_h are the true stresses and true strains in the void containing region and in the homogeneous material respectively. By coupling (8.1) with the following constitutive equation, we may solve for ε_h when ε_v reaches some critical fracture strain ε_v^*:

$$\sigma = K\varepsilon^\eta \tag{8.2}$$

where K is a material constant, σ is the true stress, ε is the true strain, and η is the strain-hardening exponent of the material. Substituting (8.2) into (8.1), we may relate the strain in the defective region to the homogeneous strain:

$$\varepsilon_v^\eta(1-f)\exp(-\varepsilon_v) = \varepsilon_h^\eta \exp(-\varepsilon_h) \tag{8.3}$$

Solving (8.3) allows the ductility of the sample to be determined by plotting ε_v against ε_h and noting the homogeneous fracture strain ε_h^* attained when the ordinate reaches some critical fracture strain ε_v^*, as illustrated in Fig. 8.1(ii). The tensile strength of the material σ_f may then be determined using (8.4), where σ^* is the true fracture strength of the 'defect-free' material obtained from $\sigma^* = K\eta^\eta$, corresponding to Considéres criterion $\varepsilon = \eta$.

$$\sigma_f = \sigma^* \left[\frac{\varepsilon_h^*}{\eta}\right]^\eta \tag{8.4}$$

Clearly, the predicted fracture strain depends on the estimated values of *f*, η and ε_v^*. Intuitively speaking, the predicted fracture strain depends on: the method used to characterise defects in the material; and the method used to describe the response of the material to plastic deformation. With regards to the former, an accurate measure of *f* can easily be obtained from the fracture surface of post-mortem specimens. However, when the location of fracture is unknown (i.e. prior to deformation) the estimation of *f* is not so trivial. The problem now becomes that of predicting which defects will be involved during tensile failure, and estimating the resultant value of *f*. By acquiring a non-destructive measure of *f* using X-ray tomography, and using this as input for the critical local strain model, Weiler et al. [24] were able to predict the location of fracture, the tensile fracture strain and the tensile fracture stress to within 8%, 22%, and 11% error, respectively. It is possible that this relatively high error stems from the axiom that fracture will occur on the tomographic plane

containing the maximum dimension of the largest defect. By considering the 3D volume as a sequence of independent 2D images, the authors effectively constrain the fracture path to a single elevation. Whilst this assumption might be accurate for defects which are highly spherical and/or small in comparison to the casting dimension, this is not the usually the case.

The purpose of this contribution is to present a new characterisation technique that identifies which defects will be involved during tensile failure and captures their true 3D form. By alleviating the spatial constraints of its predecessors, the proposed technique is capable of estimating *f* with utmost precision. The practical implications of this improvement are demonstrated by coupling the proposed estimator with the critical local strain model to predict the tensile properties of Al-Si alloy die-castings containing natural casting defects. We opt to use gravity die-castings instead of pressure die-castings for two reasons:

- Pores in gravity die-castings are much larger in size, and possess a more irregular morphology, than pores in pressure die-castings—this presents a limiting case that tests the capabilities of the proposed estimator.
- Pores in gravity die-castings are large enough to be identified via macrotomography—this allows a relatively large number of tensile specimens to be examined within a reasonable time frame.

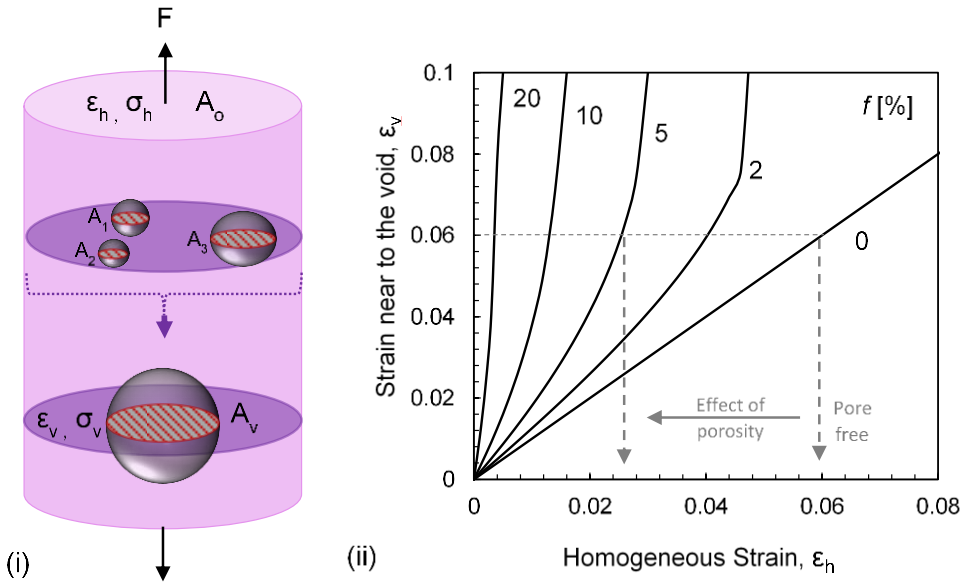

Fig. 8.1 (i) Geometry assumed by the critical local strain model, in which the effects of multiple voids of area $A_1, A_2, \ldots A_n$ are approximated by a single spherical void of area $A_v = \sum A_i$ located at the centre of an otherwise perfect specimen. (ii) Curves derived from Eq.(8.3) showing the relation between strain in the void containing region and the homogeneous strain for different areal fractions of porosity *(f)*.

8.2 Experimental Method

8.2.1 Specimen Preparation

A typical AlSiMnMg die-casting aluminium alloy (8 % Si, 0.4 % Mn, 0.3 % Mg) was used as a base material. The melt was prepared in a clay-graphite crucible (30 Kg charge) in an electric resistance furnace at 750 °C. The melt was degassed using a conventional rotary degassing unit (4 L/min at 350 rpm for 10 min) and then manually poured at 680 °C into an ASTM B108 standard permanent steel mould [25], pre-heated to 460 °C. In total, 16 tensile specimens were produced, with dimensions shown in Fig. 8.2(i). The geometry of the casting mould in addition to the nominal flow of liquid metal is shown in Fig. 8.2(ii). To acquire the strain-hardening exponent η and strength coefficient K required in (8.2), a 'pore-free' sample of dimensions equivalent to Fig. 8.2(i) was machined from the bottom region of a bespoke gravity die-casting shown in Fig. 8.2(iii); Fig. 8.2(iii) shows a prediction of shrinkage porosity in the 'pore-free' casting calculated using the POROS 1 module [26,27] in ProCAST (ESI Group).

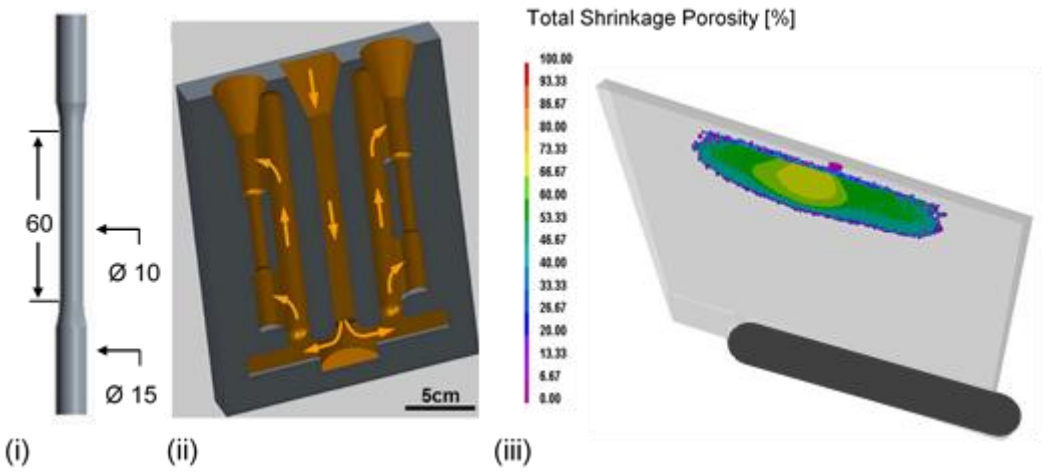

Fig. 8.2 (i) Specimen geometry (ASTM B108 [25]). (ii) Geometry of the mould used to produce tensile specimens (arrows indicate the nominal flow of liquid metal). (iii) Prediction of shrinkage porosity within the casting used to produce the 'pore free' specimen. Simulations were performed using the POROS1 module based on ProCAST code. Simulation courtesy of Dr. Kun Dou.

8.2.2 X-ray Tomography and 3D Analysis

X-ray inspection was carried out using a Y.CT Compact XL Mag computed tomography system (YXLON International; 450KV, 1mA), for which data acquisition and tomographic reconstructions are performed in parallel. An anisotropic voxel was defined, corresponding to a 2D pixel size of 133 µm and an interstitial spacing of 200 µm. The VGSTUDIO MAX software suite (Volume Graphics GmBH) was used to visualise and analyse the 3D volumes. An iterative local surface determination was

performed to define outer boundaries of the material volume whilst compensating for local fluctuations in grey value. Pore descriptors (relating to size, shape and location) were obtained using the VGDEFX void and inclusion analysis module by Volume Graphics Inc.

To identify a suitable size descriptor, two methods were used to predict the location of tensile fracture (defined here as the longitudinal distance from the bottom of the gauge section) and then compared to the actual location of fracture. In the first method, the location of fracture was predicted to occur on the tomographic plane corresponding to the centroid of the pore with the largest Feret diameter (*Diameter*). The second method utilizes a similar approach to that of Weiler et al. [24], in which fracture was assumed to occur on the tomographic plane containing the maximum projected area of porosity in the tensile direction (*Proj. Area*). A visualisation of these two methods is shown in Fig. 8.3(i).

The *Diameter* and *Proj. Area* methods may also be used to estimate the areal fraction of porosity $f_{Diameter}$ and $f_{Proj.Area}$ involved during failure: by evaluating *f* on the transverse plane coincident with the corresponding fracture locations. However, considering the inherently complex morphology of an interconnected shrinkage pore, it seems unreasonable to assume that its maximum projected area will lie exactly on one of the tomographic planes. Hence, acquiring a measure of *f* using the 2D images alone will likely result in an underestimate of the true value.

To overcome these spatial constraints, a new estimator (*Z-Project*) is presented, in which the series of images within a specified range are superimposed to estimate the maximum value of *f* within the three-dimensional sub-volume (Fig. 8.3(ii)). To achieve this, each tomographic dataset is imported as an image sequence into the Fiji image post-processing software based on ImageJ [28]. The tomographic plane containing the maximum projected area of porosity is then defined as a starting position for the image superposition (i.e. *Proj. Area*). From this plane, the sequence of images within a search distance of $\pm\sqrt{area}/2$ are examined to identify extensions of the projection in the transverse plane of the main defect along the principle stress axis; where $\sqrt{area}$ (square root of the area of the defect projected in the direction of principle stress) is selected as a representative dimension of length due to its relation with the maximum stress intensity factor along a 3D crack (i.e. $K_{I_{max}} \propto (\sqrt{area})^{1/2}$) [29,30]. The minimum intensity of each pixel within this sub-sequence is

then superimposed onto a single plane and the areal fraction of porosity measured from the generated image ($f_{Z\text{-}Project}$).

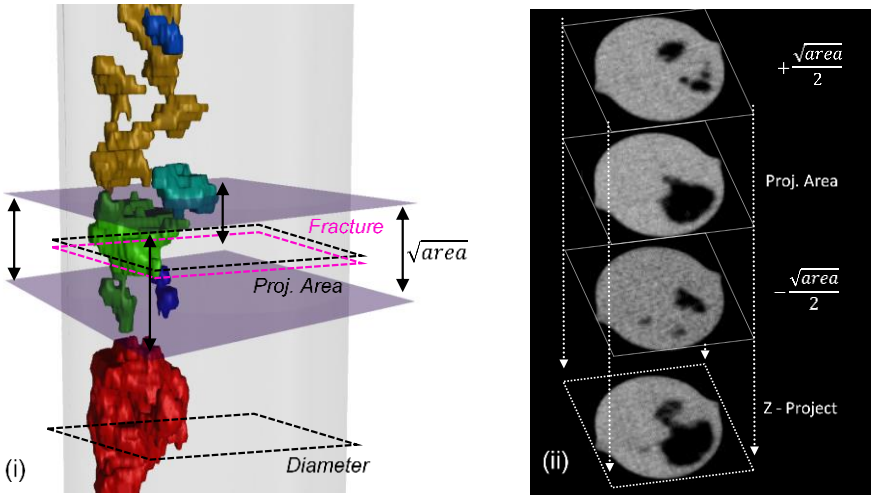

Fig. 8.3 (i) 3D visualisation of internal porosity within the tensile specimen, showing the location of fracture predicted using the Diameter and Proj. Area methods respectively. (ii) Overview of Z-Project methodology, highlighting the starting position (Proj. Area) in addition to the upper and lower limits of the image superposition.

8.2.3 Mechanical Properties and Fracture Characterization

Following X-ray inspection, tensile tests were performed at room temperature using an Instron 5500 universal electromechanical testing system equipped with a 50 kN load cell, in accordance with ASTM standard E8/E8M [31]. Post-mortem tensile specimens were examined to identify the true location of fracture, with the areal fraction of porosity on the fracture surface obtained via quantitative fractography. The location of fracture was determined by the average distance from the bottom of the gauge section to the plane defined by several symmetric points along the lateral fracture surface, in a similar manner to that described in references [32,33].

8.2.4 Critical Local Strain Model

To describe the strain-hardening behaviour of the material, values of K and η were acquired from the true stress-strain curve of the 'pore-free' sample. Equation (8.3) was then solved numerically in MATLAB (Mathworks Inc.) and the homogenous strain ε_h plotted against the strain in the void containing region ε_v. A critical fracture strain ε_v^* was defined to denote failure in the void containing region, as determined by the ductility of the 'pore-free' sample (i.e. when $f = 0$, $\varepsilon_v^* = \varepsilon_h^*$). For $f \neq 0$, strain concentrates in the void containing region and $\varepsilon_v^* > \varepsilon_h^*$. In this case, the ductility of the sample

is determined by the value of ε_h attained when $\varepsilon_v = \varepsilon_v^*$. This concept is illustrated by the dashed lines in Fig. 8.1(ii) for the hypothetical case $\varepsilon_v^* = 0.06$ and f = 0.05.

8.3 Results

8.3.1 Characterisation of Internal Porosity

Fig. 8.4 depicts a three-dimensional visualisation of porosity within the gauge length of the tensile specimens, obtained via X-ray tomography. In agreement with the underlying assumption of the critical local strain model, fracture is likely to be dominated by the presence of a single macropore or a condensed cluster of pores covering, in both cases, a sizeable fraction of the cross-sectional area. Pore morphology has also been found to play an important role in the distribution of strain. Stress concentrations induced by shrinkage cavities of an interconnected and tortuous nature have proven to be more severe than those of near-spherical gas pores of an equivalent size [9,11,34]. Sphericity, which relates the surface area of a particle or void to the surface area of a perfect sphere of equivalent volume, is commonly used to characterise the morphology of a particle or void [7,35]. In Fig. 8.5, the sphericity of each pore is plotted against its maximum Feret diameter. Pores of sphericity greater than 0.4 were assumed to originate from gaseous sources, whilst those of sphericity below 0.4 were attributed to solidification shrinkage or oxide films. From the 648 pores analysed by the VGDEFX algorithm, a quasi-logarithmic relationship was obtained between the sphericity and maximum Feret diameter.

Fig. 8.4 3D visualisation of porosity within the gauge length of tensile specimens obtained via X-ray tomography. Each connected pore is designated a colour based on its sphericity. Pores of sphericity greater than 0.4 were believed to originate from gaseous sources, whilst those of sphericity below 0.4 were attributed to solidification shrinkage or oxide films.

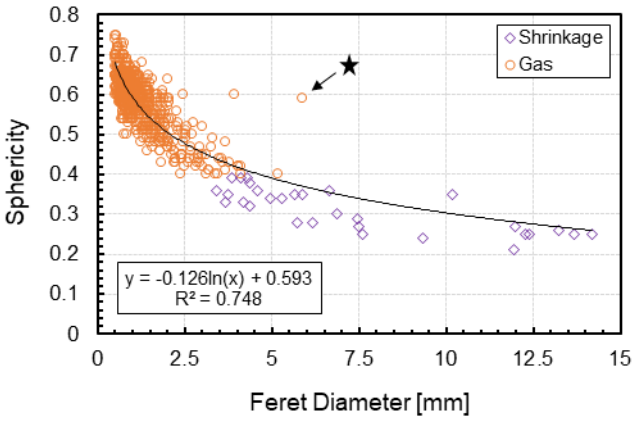

Fig. 8.5 Relationship between sphericity and maximum Feret diameter. Pores of sphericity less than 0.4 are attributed to solidification shrinkage or oxide films, whilst those of sphericity greater than or equal to 0.4 are believed to originate from gaseous sources.

8.3.2 Fracture Location

In Fig. 8.6 the fracture locations predicted using the *Diameter* and *Proj. Area* approaches are plotted against the actual location of fracture measured after tensile testing. Least squares linear regression fittings are also included in the graph, with the corresponding coefficient of determination (R^2) provided for each method. Predictions based on the *Proj. Area* method clearly surpass their *Diameter* method counterparts, with average errors of 5 % (max. 18 %) and 15 % (max. 75 %) reported for each method respectively. It follows then, that the maximum projected area of a pore in the tensile direction is a superior size descriptor than the maximum Feret diameter. An example of this difference is also shown in Fig. 8.3(i), for which failure was observed to occur not at the pore with the largest Feret diameter but instead at a smaller pore with a larger projected area in the transverse plane. These findings are in strong agreement with previous reports describing a quasi-linear relationship between the tensile fracture strain and the projected area of the largest defect observed on the fracture surface [16,17].

[This space intentionally left blank]

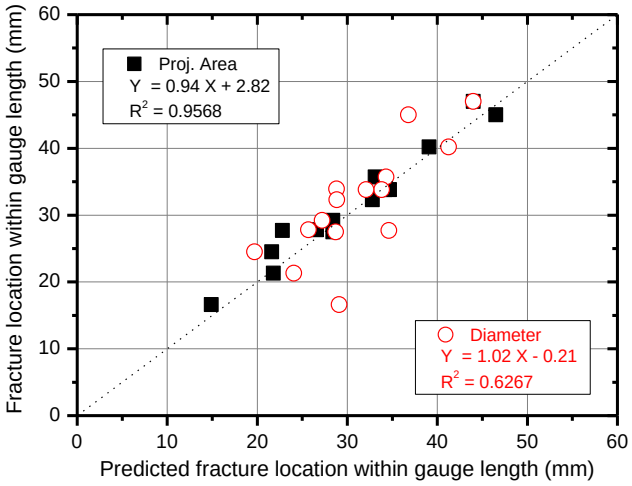

Fig. 8.6 Comparison between the true fracture location and those predicted using the *Diameter* and *Proj. Area* methods respectively. Linear fittings and corresponding R^2 coefficients are also included to compare the predictability of both methods.

8.3.3 Areal Fraction of Porosity

Fig. 8.7(i-iii) presents a visual representation of the areal fraction of porosity estimated using the *Diameter*, *Proj. Area*, and *Z-Project* methods respectively, with the actual fracture surface shown in Fig. 8.7(iv). One might expect predictions based on the *Diameter* approach to highly depend on pore morphology, as the maximum Feret diameter considers only the largest dimension of the defect without regards to the principle stress axis. Accordingly, the image produced using the *Diameter* approach is shown to drastically underestimate the true areal fraction of porosity. While there are distinct similarities between the image produced using the *Proj. Area* method and the actual fracture surface, it is evident that the true fracture path transcends the tomographic plane, and traverses multiple elevations. In contrast to this, the *Z-Project* method provides an excellent measure of the areal fraction of porosity, with the superimposed image closely resembling the actual fracture surface. Fig. 8.8 presents a quantitative comparison between the values of *f* estimated using the three prediction methods and the true areal fraction of porosity measured from fracture surface. For the majority of samples, the *Diameter* and *Proj. Area* methods produce an underestimate of *f*. The only exception to this was the value of *f* estimated for Sample-4 (marked with a star symbol in Fig. 8.4, Fig. 8.5 and Fig. 8.8) using the *Proj. Area* method, for which failure was observed to occur at a highly spherical gas pore.

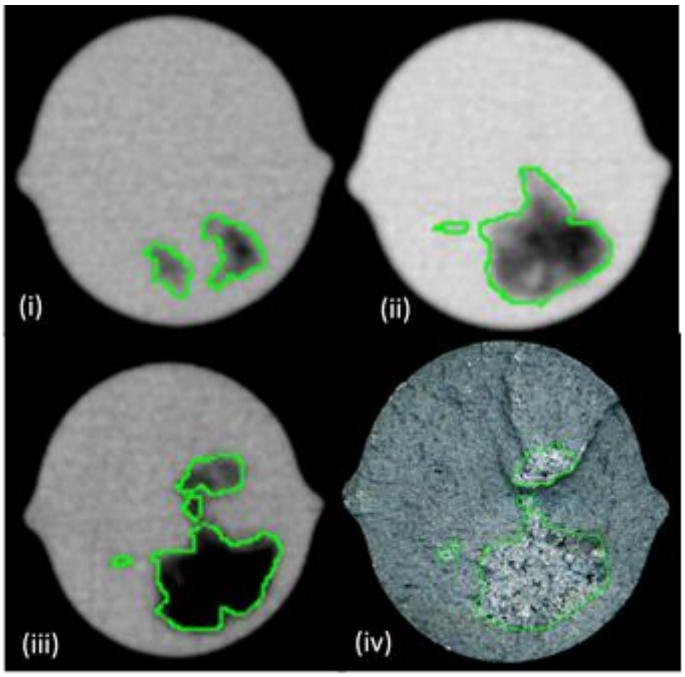

Fig. 8.7 Areal fraction of porosity estimated for a representative sample using the (i) *Diameter*, (ii) *Proj. Area*, and (iii) *Z-Project* methods respectively. For comparison, the actual fracture surface is provided in (iv). Here, green lines denote the outer boundaries of each defect.

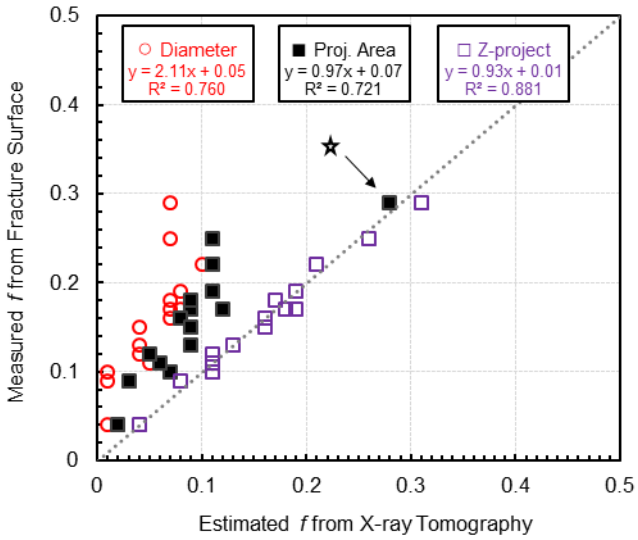

Fig. 8.8 Comparison between the true areal fraction of porosity, *f*, and those estimated using the *Diameter*, *Proj. Area*, and *Z-Project* methods respectively.

8.3.4 Mechanical Properties

The measured tensile properties of the die-cast Al8SiMnMg alloy samples are shown in Fig. 8.9(i). Note that all tensile tests were performed in the F temper. The 0.2% proof strength appears to be relatively unaffected by changes in porosity, with an average value of 101.1 ± 4.8 MPa. In contrast to this, a high degree of variability is observed for the tensile strength and the tensile ductility, with average values of 175.1 ± 20.2 MPa and 2.3 ± 1.1 % respectively. This relatively high variability in mechanical properties results from variations in the size and spatial distribution of casting defects within each sample, as will be discussed later. A power-law relation was observed between the ductility and tensile strength, as would be expected from a material that exhibits strain-hardening behaviour.

Conventionally, the parameters K, η and ε_i^* are derived from the maximum fracture strain recorded in a large series of tensile tests. The assumption is that for a sufficiently large sample size (e.g. 1000 samples [24]), the maximum strain is likely to approach that of a defect-free material. However, this induces significant cost and should be avoided when possible. In this study, we opt to obtain values of K, η and ε_v^* from a single 'pore-free' specimen machined from the custom-made gravity die-casting shown in Fig. 8.2(iii). X-ray tomography confirmed that no pores could be detected inside the machined specimen. Shown in Fig. 8.9(ii) is the true stress-strain curve used to obtain the strength coefficient K and strain-hardening exponent η of the 'pore-free' material (f = 0). Using this approach, values of $K = 341$ and η = 0.164 were obtained by fitting data in the plastic region to equation (8.2). For comparison, the true fracture strain and true fracture stress of the ASTM specimens (f > 0) are also plotted in Fig. 8.9(ii). Clearly, the points for f > 0 fall along the curve for f = 0, suggesting that the strain-hardening behaviour of the material is adequately described by the 'pore-free' specimen.

[This space intentionally left blank]

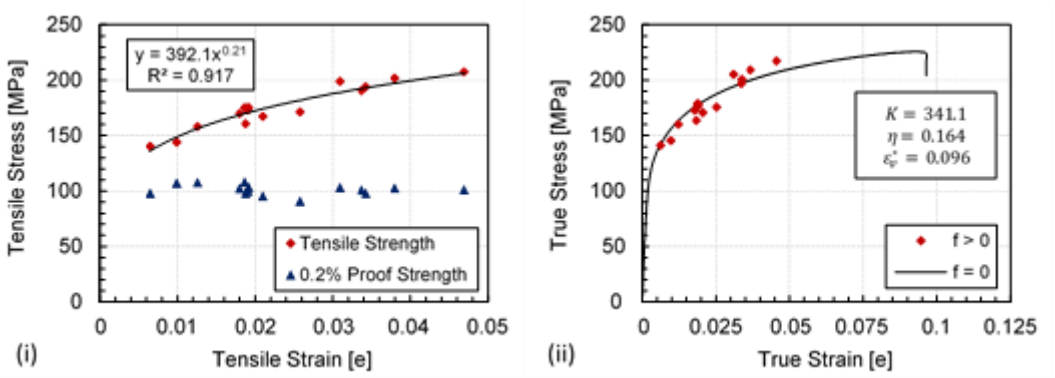

Fig. 8.9 (i) Tensile properties of the Al8SiMnMg alloy die-castings acquired from the engineering stress-strain curves of each sample. (ii) True stress strain curve of the 'pore-free' sample (f = 0) *used* to acquire the values of K, η and ε_v^* required of the critical local strain model. Also shown are the true fracture strain and true fracture stress for each of the tensile specimens (f > 0). Tensile tests were performed in the F temper.

8.3.5 Critical Local Strain Model

Using the methodology outlined in Section 8.2.4, a critical fracture strain $\varepsilon_v^* = 0.096$ was defined to denote failure in the void containing region. The homogeneous fracture strain ε_h^* was then determined by the value of ε_h attained when $\varepsilon_v = 0.096$ for a given value of f: this concept is illustrated in Fig. 8.1(ii) for the hypothetical case of $\varepsilon_v^* = 0.06$ and f = 0.05. The tensile fracture stress was then calculated for each value of ε_h^* using equation (8.4). Equations (8.3) and (8.4) were solved numerically in MATLAB for a range of f, with the predicted fracture strain and fracture stress plotted as a function of f, as shown in Fig. 8.10(i) and Fig. 8.10(ii) respectively. For comparison, the experimental data points obtained from the tensile tests are also included. Clearly, the critical local strain model can predict the tensile fracture strain and tensile fracture stress to a reasonable degree of accuracy, with average errors of 4.5 % (max. 8.9 %) and 3.9 % (max. 8.3 %), respectively.

[This space intentionally left blank]

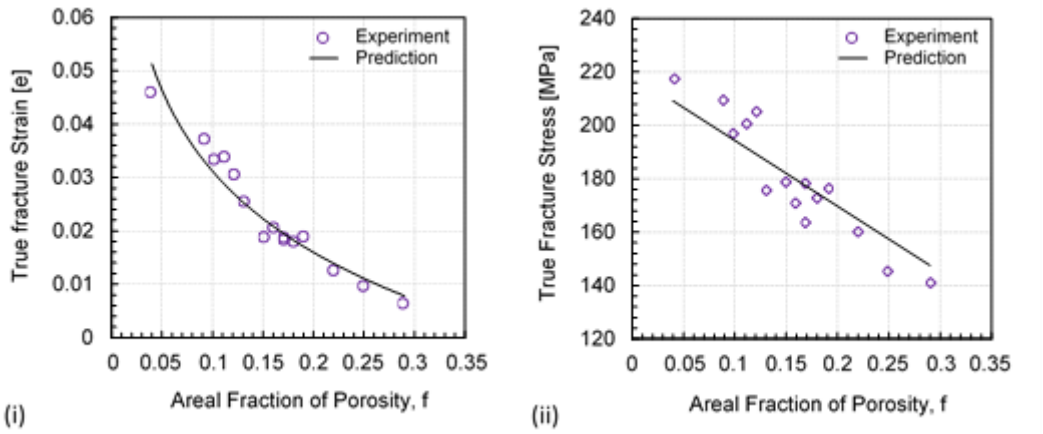

Fig. 8.10 Comparison between the predicted and measured tensile fracture strain (i) and tensile fracture stress (ii). For the experimental data points the fracture properties obtained via tensile testing are plotted against the corresponding value of *f* measured on the fracture surface.

8.4 Discussion

8.4.1 Statistical Analysis of Defect Size

The extremal types theorem allows one to make inference on the probability of low-frequency, high-severity events based on limited data. Methods based on the statistics of extremes are used within the material science and engineering community to study variability in mechanical properties, particularly in modern durability (fatigue) analysis where statistical relationships are often established between the defect size distribution and the variability in fatigue life [36]. In contrast to this, such techniques are rarely used to relate the probability distribution of defect size to the variability in tensile ductility [16].

The GEV distribution is used to approximate the limiting distribution of the maxima of defect size; a detailed description of the GEV distribution is provided in Chapter 4. We use the block maxima approach to sample our data. In block maxima, the observation period is divided into a series of sub-domains with only the maximum observation within each sub-domain considered in the analysis (i.e. $z_n = \max\{X_1, \dots X_n\}$). Accordingly, the largest defect within each specimen was identified and its value of $\sqrt{area}$ used in the subsequent analyses. Within MATLAB, GEV parameters were obtained by maximum likelihood estimation. The empirical CDF was then computed using the Kaplan-Meier estimator; 95 % confidence intervals were evaluated using Greenwood's formula. Parameter estimates and 95 % confidence intervals are provided in Table 8.1. Fig. 8.11(i) presents a visual comparison between the empirical CDF and the GEV CDF computed using the parameter estimates in Table 8.1. Since the entire 95 % confidence interval of ξ lies in the negative range, we may conclude

that the limiting distribution of maxima follows a Weibull distribution. In a similar study, Teng et al. [16] found $\xi = 0$ to lie within the 95 % confidence range, suggesting that the pore size distribution in an Al-Si alloy low pressure die-casting may be mathematically described by all three families. The authors reasoned that subject to physical considerations, the Weibull distribution was most appropriate due to its finite upper bound μ'. While defects in this study were characterised using X-ray tomography, the pore size distribution studied by Teng et al. [16] was acquired from 2D images of the fracture surface. It is possible that the observed differences in ξ arise from this difference in measurement technique—in the present contribution, pore size measurements were acquired prior to deformation.

Table 8.1 Limiting distribution of the maxima of defect size. Shown are the GEV parameter estimates and corresponding 95 % confidence intervals.

ξ- Mean	ξ– 95 % Confidence Intervals	σ	$\boldsymbol{\mu}$	σ'	$\boldsymbol{\mu}'$
-0.473	[-0.843, -0.102]	0.847	3.150	1.791	4.941

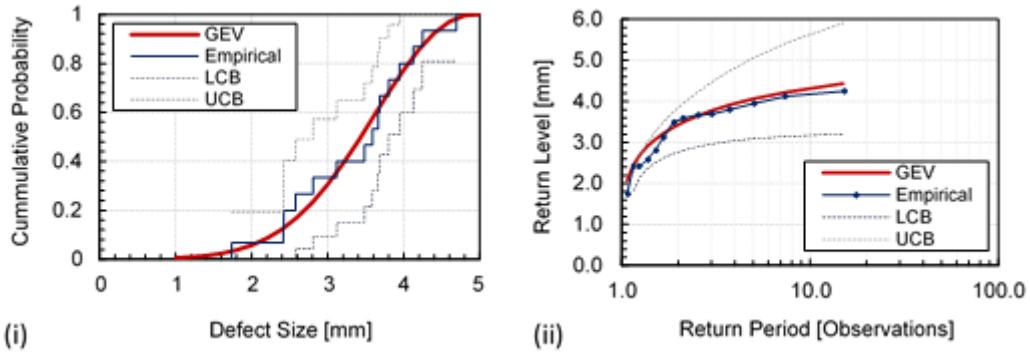

Fig. 8.11 Limiting distribution of the maxima of defect size. (i) Comparison between the empirical CDF and the GEV CDF computed using the parameter estimates in Table 8.1. Here LCB and UCB refer to the lower and upper 95 % confidence bounds of the empirical distribution respectively. (ii) Return level plot for the block maxima data. Here, the m^{th}-observation return level represents a lower bound to the maximum defect size expected in a group of *m* specimens.

Fig. 8.11(ii) presents a return level plot for the fitted model; a detailed description of return levels and return periods is provided in Chapter 4. Regarding the quality-of-fit, the fitted model provides a reasonable approximation of the empirical quantiles. For simplicity, the lower and upper bounds of the fitted curve were computed using the 95 % confidence intervals for the parameter estimates (ξ, σ, μ). Here, we simply wish to illustrate the relation between ξ and z_p as the return period tends to

infinity. The negative shape parameter ξ results in a return level curve which exhibits concavity and approaches some upper limit μ' at large return periods. Physically, this implies that the maximum defect size observed in an infinite number of tensile specimens is expected to converge towards some finite value μ'.

8.4.2 Statistical Analysis of Tensile Properties

This section discusses the application of the GEV function to estimate the limiting distribution of the minima of fracture stress and fracture strain. Here, we shall focus on the probability distribution of true stress and true strain, as these are the quantities predicted by the critical local strain model. With regards to sampling, we opt to use the block minima approach. In this case, the minimum observation within each sub-domain is stored instead of the maximum value (i.e. $\tilde{z}_n = \min\{X_1, \dots X_n\}$). A duality exists between the limiting distributions of minima and maxima such that the former may be determined by modelling the latter for $\tilde{z}_n = -z_n$ (i.e. small values of X_i correspond to large values of $-X_i$) [37]. For the sake of computational efficiency, the GEV parameters and 95 % confidence intervals were determined using the methodology outlined in Chapter 4 for $\tilde{z}_n = -z_n$, with the sign correction $\tilde{\mu} = -\mu$ (Table 8.2). Fig. 8.12(i,ii) compares the empirical CDF and the GEV CDF obtained for the probability distribution of true strain and true stress respectively. Regarding the distribution of true strain, the entire 95 % confidence interval of ξ lies in the negative range, thus we conclude that the limiting distribution of minima follows Weibull. Interestingly, $\xi = 0$ lies within the 95 % confidence range for the distribution of true stress, suggesting that the probability distribution may be mathematically described by all three families. Following the rational of Teng et al. [16], we will discuss the physical implications of the three distributions with regards to their respective tail behaviours. If we consider the upper bounds of the 95 % confidence range (i.e. $\xi > 0$), the Fréchet distribution predicts a negative lower bound of $\tilde{\mu}$ = -175.1 MPa. Here, a negative threshold has no physical meaning and usually indicates a mixture of probability distributions [36]. According to equation (8.4), the diminution of tensile strength results from the reduction in tensile strain. As there is no indication of a mixed distribution for the case of tensile strain, we have opted to disregard this possibility. Furthermore, although the upper bound of ξ lies in the positive range, one could equally say that the positive value ξ= 0.092 in fact suggests a Gumbel distribution (i.e. $\xi \to 0$). Considering the return level plot in Fig. 8.12(iv), the curve clearly exhibits some degree of concavity, again suggesting that the distribution follows Weibull. Since it is of practical interest to identify a statistical lower bound to tensile strength, the Weibull distribution is preferred to the Gumbel distribution, as the return level curve converges to a finite value $\tilde{\mu}'$. It follows then, that the presence of defects following a Weibull distribution (maxima) results in tensile fracture properties that also follow a Weibull distribution (minima): the causal relationship between

the two factors is demonstrated in Fig. 8.10, with the maximum defect size assumed to contribute to the region of maximum f.

Table 8.2 Limiting distributions of the minima of true stress and true strain. Shown are the GEV parameter estimates and corresponding 95 % confidence intervals.

	ξ-mean	ξ– 95 % Confidence Intervals	σ	$\tilde{\mu}$	σ'	$\tilde{\mu}'$
True Strain	-0.538	[-0.937, -0.138]	0.012	0.026	0.022	0.047
True Stress	-0.356	[-0.804, 0.092]	22.29	186.4	62.59	249.0

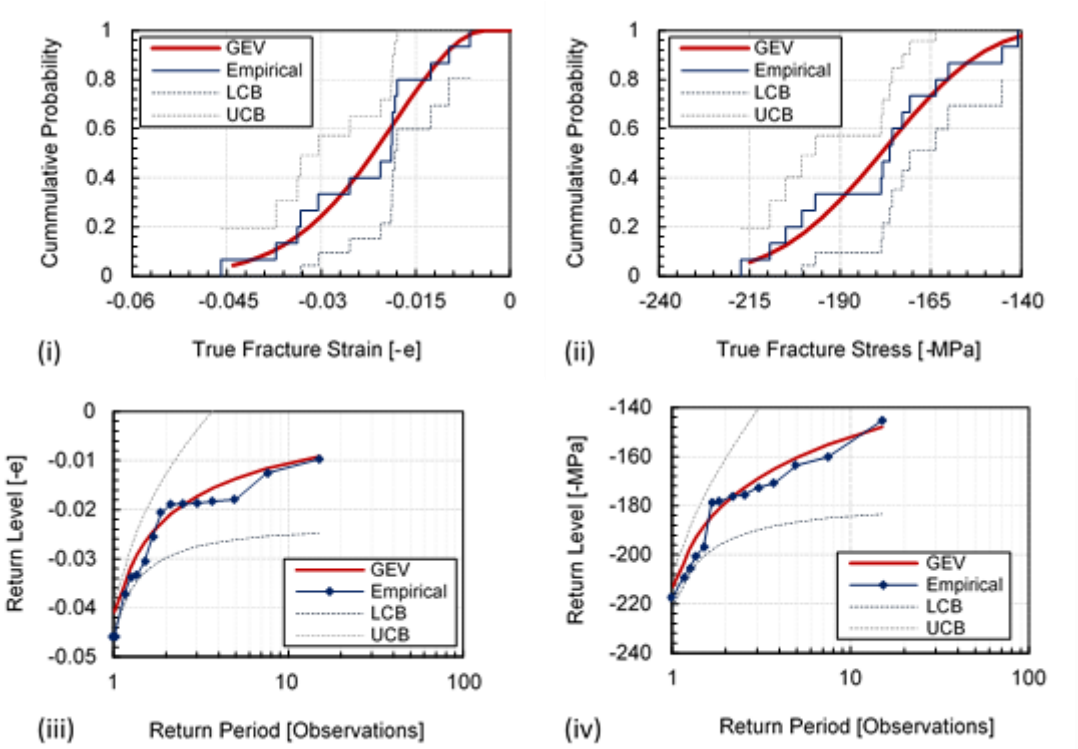

Fig. 8.12 Limiting distribution of the minima of true strain (i,iii) and true stress (ii,iv). Shown is a visual comparison between the empirical CDF and the GEV CDF (i,ii) and the corresponding return level plots for the block minima data (iii,iv).

8.4.3 Improved Prediction of Mechanical Properties

This section concerns the predictive capability of the critical local strain model when coupled with the values of f estimated via X-ray tomography. Fig. 8.13 presents a comparison between the predicted and experimental tensile fracture properties. Predictions based on the *Z-Project* method clearly exhibit superior accuracy with respect to the *Diameter* and *Proj. Area* methods. In Table 8.3, the average and maximum errors associated with the prediction of f, ε and σ are provided for each

of the three estimators. It is apparent that an improved measure of the areal fraction of porosity is accompanied by a reduction in predictive error. Accordingly, we will focus our discussion to the aptitude of the three methods in the estimation of *f*, as this controls the values predicted for the other two quantities. Here, it is useful to draw comparisons from the study of Weiler et al. [24], in which the pores analysed by the authors were much smaller and more regularly shaped ($f_{max} \approx 0.06$, $Sphericity_{min} \approx 0.48$) than those analysed in this study ($f_{max} = 0.29$, $Sphericity_{min} = 0.21$). It is interesting to note that, for the case of ε, the predictive error of the *Proj. Area* method observed in this study (95.2 %) is substantially larger than that reported by Weiler et al. (22 % [24]). We may infer, then, that for large values of *f*, the probability that the fracture plane will deviate from the transverse plane increases as the sphericity of the pore decreases. Consequently, the predictive error of conventional two-dimensional methods (i.e. *Diameter*, *Proj. Area*) also increases with decreasing sphericity. By alleviating the aforementioned spatial constraints, the *Z-Project* method is capable of estimating *f* to a superior degree of accuracy, regardless of how large or irregularly shaped these defects might be. This is confirmed by the similarity between the maximum error of the *Z-Project* method (fracture strain: 10.9 %, fracture stress: 8.9 %) and the maximum error obtained for the critical local strain model (fracture strain: 8.9 %, fracture stress: 8.3 %).

Despite the strong agreement between the *Z-Project* and baseline predictions, there is still room for improvement within the bounds of the existing model. The observed error is likely attributed to the upper and lower bounds considered for the image superposition ($\pm\sqrt{area}/2$). To further improve the characterization technique, a quantitative relationship may be established between the spatial clustering of defects and the interaction of their mechanical fields, thus enabling a more rational upper and lower bound to be determined for the image superposition. This will further improve the accuracy of the proposed estimator.

Table 8.3 Average and maximum (parenthesised) errors associated with the prediction of *f*, ε, and σ for the *Diameter*, *Proj. Area* and *Z-Project* methods respectively.

	Average Predictive error [%]		
	Diameter	*Proj. Area*	*Z-Project*
Areal fraction of porosity, *f*	63.3 (90.0)	43.3 (66.7)	5.00 (11.8)
True fracture strain, ε	180 (626)	95.2 (242)	6.22 (10.9)
True Fracture stress, σ	18.4 (45.4)	12.2 (33.5)	4.11 (8.9)

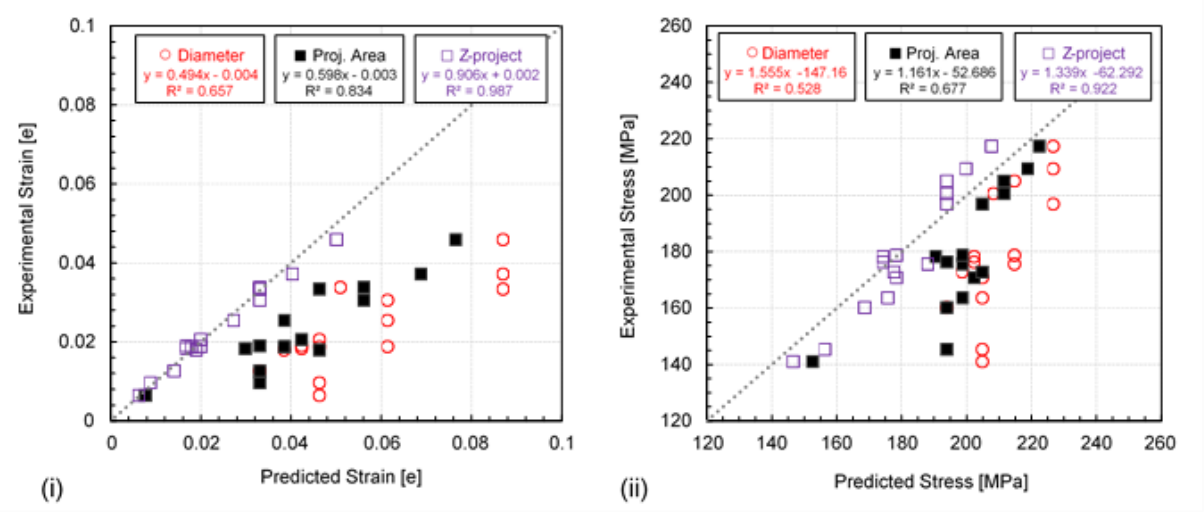

Fig. 8.13 Tensile fracture properties predicted using the critical local strain model using values of f obtained via the *Diameter*, *Proj. Area*, and *Z-Project* methods respectively. Here the predicted values of the (i) true fracture strain ε, and (ii) true fracture stress σ, are plotted against the experimental values obtained via tensile testing.

8.5 Conclusions

i. A new estimator (*Z-Project*) is presented that can predict the areal fraction of porosity involved during tensile failure to a high degree of accuracy, surpassing that of previous methods.

ii. By coupling the *Z-Project* method with an existing model for the development of plastic instabilities, the true fracture strain and true fracture stress were predicted to within 10.9 % and 8.9 % error, respectively. This fares extremely well against its predecessor, for which maximum errors of 242 % and 33.5 % were reported for the fracture strain and fracture stress, respectively. The substantial difference in error was attributed to the misalignment of the fracture plane with respect to the transverse plane, which is expected to become more severe with increasing pore size and decreasing pore sphericity. This misalignment is captured by the *Z-Project* estimator but is neglected in conventional approaches.

iii. The GEV function was used to model the upper tail of the defect size distribution. It was found that the limiting distribution of the maxima of defect size was best described by a Weibull distribution. It follows that the presence of defects following a Weibull distribution result in tensile fracture properties that also follow a Weibull distribution. This presents the opportunity to determine a finite upper bound for the maximum defect size, and thus a finite lower bound for the tensile fracture properties.

8.6 References

[1] C.H. Cáceres, On the Effect of Macroporosity on the Tensile Properties of the Al-7%Si-0.4%Mg Casting Alloy, Scripta Metall. Mater. 32 (1995) 1851–1856.

[2] C.H. Cáceres, B.I. Selling, A Casting Defects and the Tensile Properties of an Al-Si-Mg Alloy, Mater. Sci. Eng. A:. 220 (1996) 109–116.

[3] C. Dørum, O.S. Hopperstad, O.-G. Lademo, M. Langseth, Aluminium and Magnesium Castings - Experimental Work and Numerical Analyses, Int. J. Crashworthiness. 8 (2003) 455-470.

[4] L. Wang, N. Limodin, A. El Bartali, J.F. Witz, R. Seghir, J.Y. Buffiere, E. Charkaluk, Influence of Pores on Crack Initiation in Monotonic Tensile and Cyclic Loadings in Lost Foam Casting A319 Alloy by Using 3D In-Situ Analysis, Mater. Sci. Eng.: A 673 (2016) 362–372.

[5] D. Mohr, R. Treitler, Onset of Fracture in High Pressure Die Casting Aluminum Alloys, Eng. Fract. Mech. 75 (2008) 97–116.

[6] H. Zhang, H. Toda, H. Hara, M. Kobayashi, T. Kobayashi, D. Sugiyama, N. Kuroda, K. Uesugi, Three-Dimensional Visualization of the Interaction Between Fatigue Crack and Micropores in an Aluminum Alloy Using Synchrotron X-Ray Microtomography, Metall. Mater. Trans. A 38 (2007) 1774–1785.

[7] L. Zaidao, Influence of the Microstructure on Mechanical Properties and Damage Mechanisms in Al-Si-Cu Alloys by Using 2D and 3D In-Situ Analysis, Université de Lille, 2016.

[8] P. Li, P.D. Lee, D.M. Maijer, T.C. Lindley, Quantification of the Interaction Within Defect Populations on Fatigue Behavior in an Aluminum Alloy, Acta Mater. 57 (2009) 3539–3548.

[9] S. Dezecot, V. Maurel, J.Y. Buffiere, F. Szmytka, A. Koster, 3D Characterizaation and Modeling of Low Cycle Fatigue Damage Mechanisms at High Temperature in a Cast Aluminum Alloy, Acta Mater. 123 (2017) 24–34.

[10] M.F. Horstemeyer, J. Lathrop, A.M. Gokhale, M. Dighe, Modelling Stress State Dependent Damage Evolution in a Cast Al-Si-Mg Aluminum Alloy, Theor. Appl. Fract. Mech. 33 (2000) 31–47.

[11] S. Dezecot, J.Y. Buffiere, A. Koster, V. Maurel, F. Szmytka, E. Charkaluk, N. Dahdah, A. El Bartali, N. Limodin, J.F. Witz, In Situ 3D Characterization of High Temperature Fatigue Damage Mechanisms in a Cast Aluminum Alloy Using Synchrotron X-Ray Tomography, Scripta Mater. 113 (2016) 254–258.

[12] J. Song, S.M. Xiong, M. Li, J. Allison, In Situ Observation of Tensile Deformation of High-Pressure Die-Cast Specimens of AM50 Alloy, Mater. Sci. Eng.: A. 520 (2009) 197–201.

[13] I. Bacaicoa, M. Wicke, M. Luetje, F. Zeismann, A. Brueckner-Foit, A. Geisert, M. Fehlbier, Characterization of Casting Defects in a Fe-Rich Al-Si-Cu Alloy by Microtomography and Finite Element Analysis, Eng. Fract. Mech. 183 (2017) 159–169.

[14] A.M. Waters, Three-Dimensional Analysis of Voids in AMGOB Magnesium Tensile Bars Using Computed Tomography Imagery, United States, (2001), doi:10.2172/15006000.

[15] X. Sun, K.S. Choi, D.S. Li, Predicting the Influence of Pore Characteristics on Ductility of Thin-Walled High Pressure Die Casting Magnesium, Mater. Sci. Eng.: A. 572 (2013) 45–55.

[16] X. Teng, H. Mae, Y. Bai, T. Wierzbicki, Pore Size and Fracture Ductility of Aluminum Low Pressure Die Casting, Eng. Fract. Mech. 76 (2009) 983–996.

[17] X. Teng, H. Mae, Y. Bai, T. Wierzbicki, Statistical Analysis of Ductile Fracture Properties of an Aluminum Casting, Eng. Fract. Mech. 75 (2008) 4610–4625.

[18] S.G. Lee, G.R. Patel, A.M. Gokhale, A. Sreeranganathan, M.F. Horstemeyer, Quantitative Fractographic Analysis of Variability in the Tensile Ductility of High-Pressure Die-Cast AE44 Mg-Alloy, Mater. Sci. Eng.: A. 427 (2006) 255–262.

[19] J.P. Weiler, J.T. Wood, Modelling Fracture Properties in a Die-Cast AM60B Magnesium Alloy I-Analytical Failure Model, Mater. Sci. Eng.: A. 527 (2009) 25–31.

[20] J.P. Weiler, J.T. Wood, Modelling Fracture Properties in a Die-Cast AM60B Magnesium Alloy II-the Effects of the Size and Location of Porosity Determined Using Finite Element Simulations, Mater. Sci. Eng.: A. 527 (2009) 32–37.

[21] J.P. Weiler, J.T. Wood, Modelling the Tensile Failure of Cast Magnesium Alloys, J. Alloys Compd. 537 (2012) 133–140.

[22] G. Nicoletto, G. Anzelotti, R. Konečná, X-Ray Computed Tomography vs. Metallography for Pore Sizing and Fatigue of Cast Al-Alloys, Procedia Eng. 2 (2010) 547–554.

[23] A.K. Ghosh, Tensile Instability and Necking in Materials with Strain Hardening and Strain-Rate Hardening, Acta Metall. 25 (1977) 1413–1424.

[24] J.P. Weiler, J.T. Wood, R.J. Klassen, E. Maire, R. Berkmortel, G. Wang, Relationship Between Internal Porosity and Fracture Strength of Die-Cast Magnesium AM60B Alloy, Mater. Sci. Eng.: A. (2005) 315–322.

[25] ASTM Committee, ASTM Volume 02.02 Aluminium and Magnesium Alloys, 2006.

[26] A.J. Torroba, O. Koeser, L. Calba, L. Maestro, E. Carreño-Morelli, M. Rahimian, S. Milenkovic, I. Sabirov, J. LLorca, Investment Casting of Nozzle Guide Vanes from Nickel-Based Superalloys: Part I – Thermal Calibration and Porosity Prediction, Integr. Mater. Manuf. Innov. 3 (2014) 344–368.

[27] J. Guo, A. Makinde, B. Bewlay, Modelling of Shrinkage Porosity Formation and its Validation, Proc. from 12th Int. Conf. Model. Cast. Welding, Adv. Solidif. Process. (2009) 337–344.

[28] Fiji/ ImageJ. https://imagej.nih.gov/ij/ (accessed August 22, 2018).

[29] Y. Murakami, M. Endo, Effects of Defects Inclusions and Inhomogenieities on Fatigue Strength, Int. J. Fatigue, 16, (1993), 163-182.

[30] Y. Murakami, M. Endo, Quantitative Evaluation of Fatigue Strength of Metals Containing Various Small Defects or Cracks, Eng. Fract. Mech. 17 (1983) 1–15.

[31] ASTM committee, Standard Test Methods for Tension Testing of Metallic Materials, 2003.

[32] Q. Xue, Y. Wang, H. Zhai, X. Chang, Automatic Identification of Fractures Using a Density-Based Clustering Algorithm with Time-Spatial Constraints, Energies. 11 (2018) 1-15.

[33] Q. Xue, Y. Wang, X. Chang, Automatic 3D Fracture Plane Identification with Spatial Constraints, Society of Exploration Geophysicists, 2016: pp. 3443–3447.

[34] P. Mu, Y. Nadot, I. Serrano-Munoz, A. Chabod, Influence of Complex Defect on Cast AS7G06-T6 Under Multiaxial Fatigue Loading, Eng. Fract. Mech. 123 (2014) 148–162.

[35] V. Boulos, L. Salvo, D. Houzet, P. Lhuissier, Investigating Performance Variations of an Optimized GPU-Ported Granulometry Algorithm, Des. Archit. Signal Image Process., 2012: pp. 1–6.

[36] M. Tiryakioğlu, J. Campbell, Weibull Analysis of Mechanical Data for Castings: A Guide to the Interpretation of Probability Plots, Metall. Mater. Trans. A 41 (2010) 3121–3129.

[37] S. Coles, An Introduction to Statistical Modelling of Extreme Values, Springer, 2001.

Chapter 9: Concluding Remarks

9.1 Conclusions

To conclude, porosity and non-metallic inclusions are the primary sources of variability in tensile ductility (for die-cast specimens produced under *Baseline* conditions). We propose that these non-metallic inclusions form during the pyrolysis of commercial plunger lubricants, and that these large pores derive from dilatational strains introduced during semi-solid deformation. The seemingly probabilistic nature of pore formation is thus attributed to variations in the local grain structure surrounding a liquid channel. By changing the kinematics of the plunger, one can greatly reduce the variability in tensile ductility. This improvement is attributed to a significant reduction in the maximum pore size (from 1.32 mm to 0.37 mm), which in turn is related to the extent of heat loss in the shot chamber.

Next, we consider the breakup of defect-forming suspensions during the transportation of liquid metals. In a turbulent flow, large non-metallic inclusions are broken down into more, smaller particles with a compact morphology. This refinement leads to significant improvements in tensile strength (mean: +17 %) and tensile ductility (mean: +35 %). An increase in turbulent kinetic energy is also accompanied by a refinement of large dendritic crystals formed in the shot chamber. We attribute this refinement to the fragmentation of incipient grains due to turbulent oscillations of the surrounding liquid.

Finally, we present a novel technique—based on X-ray tomography and digital image processing—to predict the areal fraction of porosity involved during tensile failure. By coupling this estimator with an existing model for the development of plastic instability in a deforming body, we predict the tensile fracture strain and tensile fracture stress to within 10.9 % and 8.1 % error, respectively. This fares well against its predecessor, for which maximum errors of 242 % and 33.5 % were reported for the fracture strain and fracture stress, respectively.

Despite its shortcomings, this thesis provides a solid foundation for future work to build upon. It unmasks the underlying cause of variability in the HPDC process, and identifies useful phenomena for technological development. Furthermore, it establishes a quantitative relationship between the casting integrity and the materials performance in monotonic tension, enabling materials engineers to produce more informed safety factors for component design. This will assist in vehicle lightweighting and the reduction of green gas emissions.

9.2 Suggestions for Future Work

“It is a commonplace in academic circles to say that any good doctoral thesis throws up more questions than it solves”—Brian Cantor [1]. While I am unable to comment on the quality of this

thesis, it certainly presents a number of interesting questions. Here, we consider a few of these questions and discuss possible avenues for future work.

Porosity and non-metallic inclusions are identified as the main sources of variability in tensile ductility; however, we know little about these defects and the factors influencing their formation. Future studies could address this gap in knowledge. For example, one could study the influence of melt temperature and lubricant composition on the formation of non-metallic inclusions, which may lead to the development of novel plunger lubricants. One could also study the influence of solid fraction and intensification pressure on the maximum pore size. This may reveal the extent to which semi-solid deformation influences pore growth in HPDC.

In Chapter 7, we present a novel technique—based on X-ray tomography and unsupervised machine learning—that partitions inclusions into clusters based on their size, shape, and attenuating behaviour. From this, one can deduce the species of inclusions contained in the material. This could be a very powerful tool for microstructural characterization. Future studies could aim to develop a tool that automatically identifies different phases in a material and performs quantitative analyses on the individual phases.

Although we show that fluid turbulence can lead to de-agglomeration and dendrite fragmentation in HPDC, we have yet to explore the key variables influencing breakage. One could investigate the effects of turbulent energy dissipation rate, particle residence time, and cohesive bond strength on the extent of breakage. Such studies may be performed experimentally, or numerically using the discrete-element method, and may lead to the design of novel runner systems for HPDC. A similar approach could also be used to study the dispersion of reinforcement particles in the manufacture of metal matrix composites.

In Chapter 8, we establish a quantitative relationship between the casting integrity and the materials performance in monotonic tension; however, the problem is inherently more complex for the case of cyclic loading. For example, separate relationships are required for the case of low-cycle (strain-life) fatigue, and high-cycle (stress-life) fatigue. The finite-element method may be used to investigate the influence of factors, such as defect size and morphology, on the localisation of strain. One could also adopt a similar approach to establish a relationship between the spatial clustering of defects and the interaction of their mechanical fields.

9.3 References

[1] B. Cantor, The Equations of Materials, Oxford University Press, 2020.